PULSED FERRITE X-BAND GENERATOR

Final Report

for

Contract DA 28-043-AMC-00397(E)

M. L. Report No. 1467

U. S. Army Electronics Command

Fort Monmouth, New Jersey

March 1967

Prepared in accordance with
DA Project No. 1G6-22001-A-055-05
Electronics Command Technical Requirement
No. SCL-5506B, dated 18 February 1963

Approved by H. J. Shaw

Microwave Laboratory
W. W. Hansen Laboratories of Physics
Stanford University
Stanford, California

DISTRIBUTION OF THIS DOCUMENT IS UNLIMITED

ECOM

UNITED STATES ARMY ELECTRONICS COMMAND · FORT MONMOUTH, N.J.

PULSED FERRITE X-BAND GENERATOR

Final Report

for

Contract DA 28-043 AMC-00397(E)

M. L. Report No. 1467

U. S. Army Electronics Command

Fort Monmouth, New Jersey

March 1967

Approved by H. J. Shaw

Microwave Laboratory
W. W. Hansen Laboratories of Physics
Stanford University
Stanford, California

ABSTRACT

A magnetically saturated ferrite subjected to a pulsed magnetic
field forms a generator of coherent microwave energy. It is shown
that relatively high peak rf power in short pulses can be generated
in this way. A pulsed magnetic field having amplitude ~ 4 Kg and
rise time ~ 1 ns is developed by a strip-line pulser with spark-gap
switches. This pulsed field causes nonadiabatic excitation of a
coherent oscillation in a YIG sphere. The pulsed field also produces
adiabatic pumping of the frequency and energy of this oscillation, so
that the output frequency is not related to the pulsed-field rise
time. The entire process is completed inside the build-up time of
second-order spin waves, allowing precession angles in the YIG to
exceed the usual steady-state spin-wave threshold by an order of magni-
tude. A monolithic circuit element contains a pulsed-field loop and an
x-band resonator, which are mutually uncoupled but both tightly coupled
to the YIG. The resonator extracts x-band energy from the YIG by radia-
tion damping and transfers it to an output waveguide. The resonator is
tunable and determines the output frequency. Coherent, nearly mono-
chromatic rf output pulses having energy of several hundred watt-ns, and
pulse widths in the range of 1 - 3 ns, have been observed using YIG diam-
eters in the vicinity of 50 mils. These results are in good agreement
with theoretical predictions.

TABLE OF CONTENTS

I. INTRODUCTION

This project has been concerned with development of a coherent microwave oscillator using a small sample of yttrium iron garnet (YIG) subjected to a pulsed magnetic field. The first proposal for devices of this kind appears to have been made by R. V. Pound in 1959.[1] In the years following that time, however, it developed that several advancements in ferrite theory and technology were to be required before progress could be made with this kind of device. At the time, ferrite line widths were too large to allow the use of magnetic field pulses with reasonable rise times. Also, it turned out that refinements and advancements in spin wave theory were required, so that the limitations imposed on the operation of these devices by the build-up of spin waves could be understood and properly taken into account in the design. Also, at that time, no work had been reported on pulser circuits designed to produce the large field magnitudes required for microwave frequency generation together with the short rise times required for satisfactory operation of the device.

In the meantime some closely related devices were studied.[2,3,4] These devices accomplished pulsed frequency translation in ferrites. They used a pulsed magnetic field to translate upward the frequency and energy of an oscillation which was established in the ferrite sample before the application of the field pulse. An rf input signal, which was essentially a cw signal, was applied to the ferrite to establish this initial uniform precession. These devices were found to perform largely as predicted. They were limited to low power levels by the second-order spin-wave instability.

In contradistinction to these earlier devices, the present device uses the pulsed magnetic field to start the initial precession in addition to translating the frequency and energy. When this is done it is possible to avoid the serious limiting of the power output resulting from spin waves. It is now well-known that first-order and second-order

spin wave instabilities restrict the rf energy associated with the precession in devices using low-loss ferrites. With the exception of limiters, which use these processes to advantage, these devices are degraded in performance by the spin waves. The present device avoids this limitation by operating on a short-pulse basis. I is found that the excitation and translation processes referred to above can be carried out on a time scale which avoids serious degradation of performance due to spin waves.

In previous reports, the former type of device has been referred to as the Type I generator, while the device of concern here has been referred to as Type II.

The present device makes use of the fact that a small ferrite sample of single crystal YIG constitutes a high-Q microwave resonator whose frequency can be tuned throughout the entire microwave range by simply varying the magnitude of an applied dc magnetic field. Figure 1(a) is the usual illustration of the uniform precession mode in a spherical sample, which is the mode that is of concern in the present work. In this case, the precessional motion is circular with amplitude Θ . The frequency tuning of the oscillation is linear in the amplitude of the applied magnetic field H . Figure 1(b) consists of a simple RLC circuit representing a general singly-resonant system, which includes the case of the ferrite resonator. It is well known that if an initial free oscillation is present on such a circuit, and if we tune the resonant frequency of this circuit upward as a function of time, both the frequency and energy of the initial oscillation will increase. This increase in energy of the oscillation will be proportional to the increase in frequency. This will be ture if proper conditions on the rate of increase of the frequency tuning are met.

The device to be described utilizes this principle and makes use of the fact that a pulsed magnetic field whose magnitude increases with time can be used to accomplish the tuning function. Furthermore, it is found that if this pulsed magnetic field is properly applied, it can start the initial oscillation on the circuit as well as translating its frequency and energy in the manner referred to above.
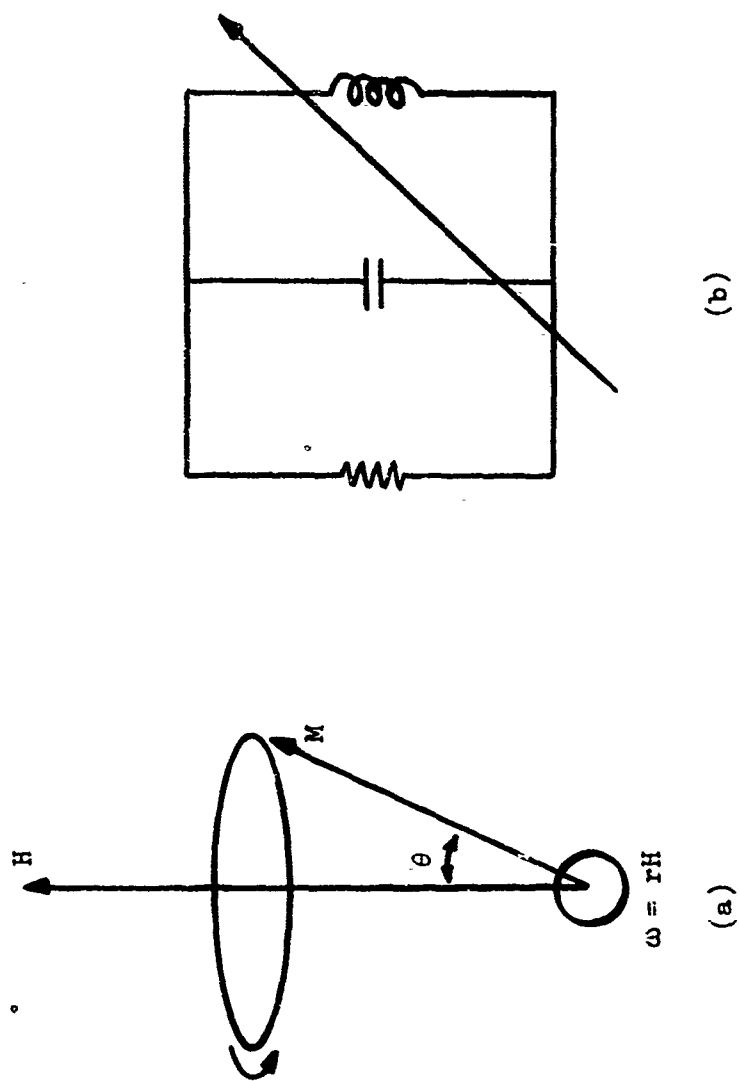
- 2 -

FIG. 1 -- Schematic representation of ferrite resonator.

$\omega = rH$

(a)

(b)

Figure 2 shows a block diagram of the principal components of the Type II generator. A permanent magnet supplies a small dc magnetic field which saturates the YIG sphere. A pulsed current generator feeds current to a coil which generates the pulsed magnetic field that performs the functions described above. In the presence of this pulsed field, the total field applied to the ferrite will be a rising function of time, of the nature of the curve shown at the bottom of Fig. 2. Since, for a YIG sphere, the frequency is proportional to the net applied field, the ordinate for this curve can be labeled in terms of frequency, which refers to the instantaneous frequency of the oscillation in the sphere. Also coupled to the YIG sphere, in addition to the permanent magnet and the pulsed field coil, is an electromagnetic circuit resonator. In the present instance, this circuit is resonant in the x-band frequency range. For any given adjustment of this circuit, its resonant frequency is a constant as indicated by the horizontal dashed line in Fig. 2. As the resonance of the ferrite oscillation cuts through the resonance line of the circuit, some of the energy associated with the oscillation in the ferrite will be transferred to the circuit. The circuit will then ring coherently at its resonant frequency. The circuit is coupled to an output waveguide and radiates an output signal into this waveguide.

We have stated that in the present device the pulsed magnetic field performs two separate functions, namely initiation and translation of the oscillation. It is not surprising to find, in a device which uses a pulsed field to excite coherent oscillation, that there is a requirement on the rate of rise of the field pulse. In a rough way, the field is required to reach a certain magnitude in a time which is short compared to the period of the rf oscillation which is to be excited. These requirements are defined more precisely in the body of the present report. However, it may be useful at this point to describe qualitatively their place in the design and operation of the present device. In the initial excitation process the scale of magnetic field values is set by the magnitude of the applied dc magnetic field, and the field level which must be reached in the prescribed time is of the order of magnitude of this dc field. The time scale in this initial excitation process is also controlled by the dc field magnitude
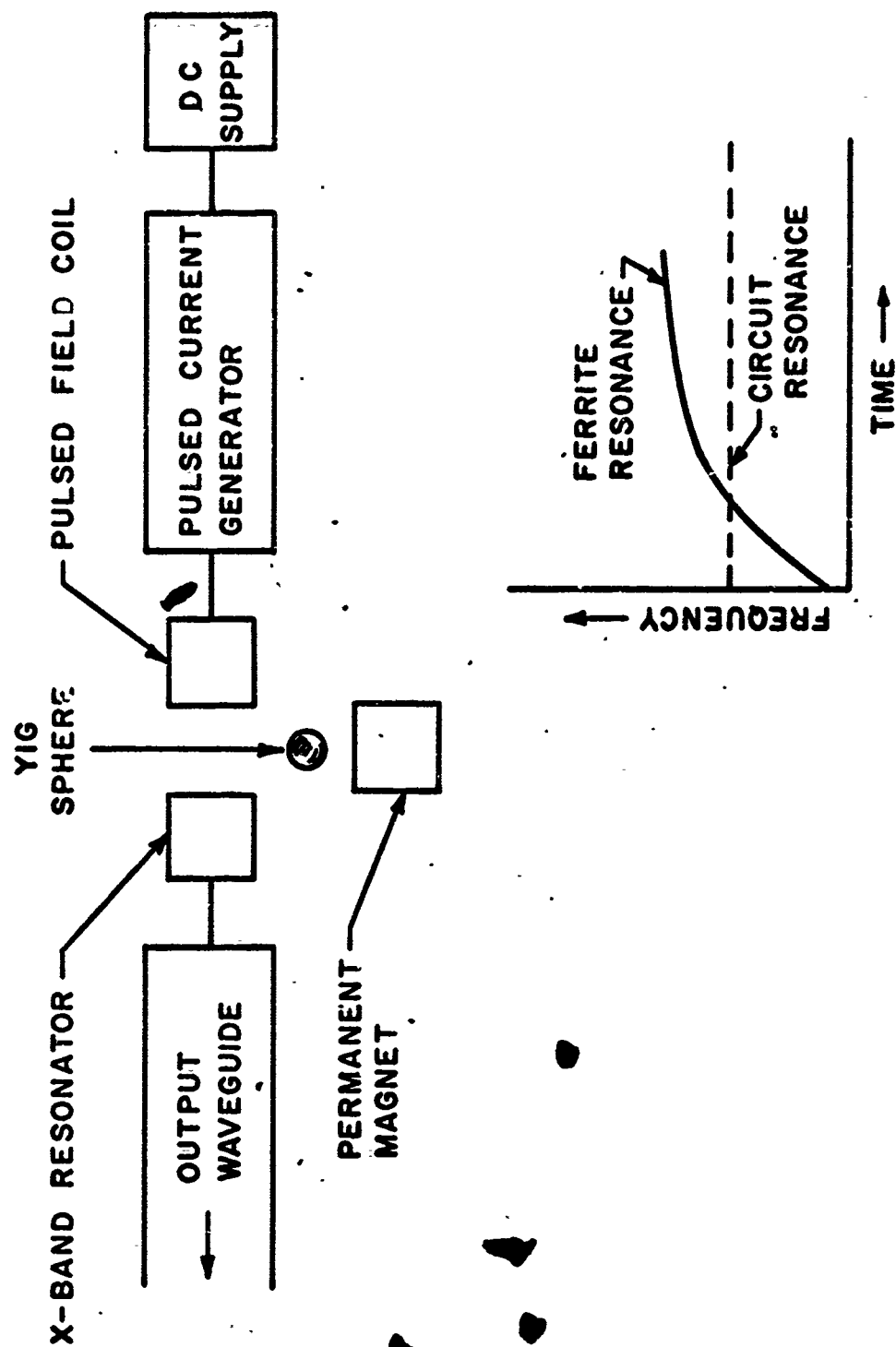
- 4 -

FIG. 2.—Block diagram of Type II ferrite generator.

because the oscillation period just mentioned refers to the period of
the resonant frequency of the ferrite in the dc magnetic field alone
which, as we have seen, is directly proportional to the magnitude of
the dc field. Thus, the requirement for efficient excitation of the
initial oscillation is a requirement on the time-rate-of-rise of the
first small portion of the pulsed magnetic field curve. Furthermore,
this initial time-rate-of-rise is set entirely by the initial oscil-
lation frequency and is totally unrelated to the frequency of the out-
put energy delivered by the device. Once the nonadiabatic requirement
on the initial portion of the pulsed field rise has been met, the pulsed
field can continue to rise beyond that point in an adiabatic fashion,
and in a time covering many rf oscillation periods, in reaching a final
value. During this larger, second regime of the pulsed field rise the
frequency and energy of the oscillation are translated upward by a sub-
stantial amount. Thus, the pulsed field rise is adiabatic with respect
to the output frequency and is not related in any direct way to the out-
put frequency. In the present designs, the magnitude of the dc field
is set at the lowest value which is consistent with saturation of the
YIG sphere. As we have just seen this lowers the rise rate require-
ment of the initial first portion of the field pulse by simultaneously
decreasing the field level associated with the initial portion of the
pulse and also increasing the time allowed to reach that level.

The second, or adiabatic portion of the field rise, which in
practice is actually much the larger portion, is limited in total time,
in principle, by two requirements, but in practice by only one. The
first requirement is that this field reach its final magnitude in a time
which is short compared to the relaxation time of the uniform precession
mode in the ferrite sample. In the case of single crystal YIG materials,
this relaxation time is sufficiently long as to constitute essentially
no problem. The second requirement is that the field reach its final
value before second-order spin wave pumping can decrease the amplitude
of the rf precession which has been established. In principle, during
this translational portion of the field rise, the amplitude of the rf
precession is constant, in the absence of parametric spin waves, but

- 6 -

decreases very rapidly with time after spin wave build-up gets underway. This turns out to be the controlling factor in setting the rise time condition during the second portion of the pulsed field profile. As will be seen, it is found that there is sufficient time under this consideration for the total pulsed magnetic field rise to be completely nonadiabatic with respect to the output frequency in a practical case.

Successful operation of this type of device has been demonstrated previously.[5,6] However, as a result of the investigations carried out under the present Contract DA 28-043-AMC-00397(E), the rf output power of devices of this kind has been increased by several orders of magnitude over any previously reported results.

The principal areas of investigation have been concerned with the theory of the build-up of the uniform precession mode in ferrites subjected to pulsed magnetic fields, theory of spin wave build-up under these same conditions, theory of transfer of energy from a pulsed ferrite to a microwave circuit, development of pulsed circuitry for the production of multi-kilogauss, nanosecond-rise field pulses, development of compatible dc pulse and rf pulse circuits for coupling directly to a ferrite sample, development of measurement techniques for the fast dc and rf pulses produced by the above apparatus, and design and testing of experimental models of Type II x-band generators. This report contains references to, and descriptions of, work carried out along these lines, leading to the successful demonstration of high peak power in a device of this kind.

The work leading to the demonstration of high peak power from Type II ferrite generators and the results obtained on the experimental Model II-B are summarized in a recent publication under the present contract.[7] In the present report we include the material contained in that publication, together with some additional material. This additional material includes: (1) further discussion and data on some of the subjects referred to in the paper and (2) a summary of some further investigations which were undertaken under the present contract subsequent to the work referred to in the paper. A few key items from earlier status reports under the contract are also included in the present report.

Further details on activities during the year may be obtained by reference to those reports.[8]

This present report is concerned only with the latest experimental model of the ferrite generator, which has been designated Model II-B. Work was done earlier in the contract year under the subject contract, on a Model II-A generator. This device was limited to very low power compared to the Model II-B device, but the results and experience gained with the former device led to some of the modifications resulting in high peak power output from the Model II-B generator. For a summary of results obtained with the II-A apparatus the reader is referred to the Quarterly Status Reports.[8]

II. THEORY OF OPERATION

A. Establishment of Uniform Precession

The establishment of a coherent uniform precession oscillation is accomplished by applying to the ferrite both a dc magnetic field H_0 and a pulsed magnetic field H_p , as indicated in Fig. 3, whose directions differ by an angle Ψ_0 which, in the figure, is shown as 90°. The purpose of H_0 is to saturate the ferrite and to establish the initial direction of the magnetization M . As the magnitude of H_p increases with time, the total field H_T rotates away from its initial direction along H_0 , establishing a growing geometrical angle Ψ between H_T and H_0 . As a result of this angle, M tends to precess about the axis of H_T , along some path which is indicated symbolically by the dashed line in the figure, such that the angle Θ between H_T and M tends to be less than Ψ , but increases monotonically as the rate of rise of H_p is increased. Taking the magnitude of H_p to be a linear function of time, then to obtain relatively large values of Ψ , it is necessary that dH_p/dt be sufficient for H_T to become of the order of H_0 in a time of the order of one radian at the initial precession frequency γH_0 . Also, Θ attains essentially its full growth Θ_ℓ (defined as Θ at $t = \infty$) during this time interval, remaining relatively constant as H_T continues to grow and Ψ approaches Ψ_0 .

Values of Θ_ℓ for arbitrary values of H_0 , Ψ_0 and dH_p/dt have been calculated using the digital computer. This work was initially carried out under contract DA 36(039)AMC-00041(E), the predecessor to the present contract, and was issued as a technical report under that contract. During the period of the present contract this report was revised for publication.[9] Because of its basic importance in the design of the Type II ferrite generator, this revised version of the report is included herewith as Appendix A.
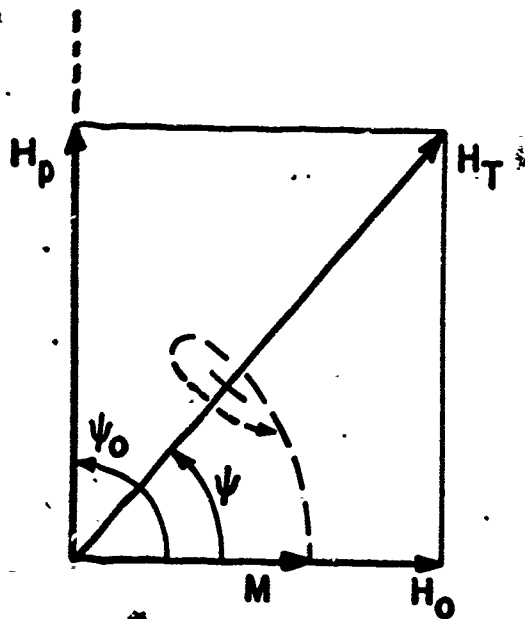
- 9 -

FIG. 3 --Geometry of magnetic fields applied to ferrite sample.

A very useful way of representing some of the results of these calculations on uniform precession amplitude is indicated in Fig. 4. This figure shows the theoretical value of the final precession angle as a function of a parameter R , using data taken from the results shown in Appendix A. In Fig. 4, the parameter R measures the field strength reached by the pulsed field in a time corresponding to one radian of precession of the magnetization at the initial precession frequency. For this purpose, field strength is measured in units of the applied dc field H_0 . This coordinate normalization is very convenient for application to the Type II generator. In Fig. 4 the final precession angle is shown for two particular values of pulsing angle Ψ_0 , namely 90^c and 20°. In the experiments described below, 90° pulsing was employed. In Fig. 4 the curve for 20° pulsing is included for reference, and curves corresponding to other pulsing angles are readily obtained from the data in Appendix A.

In the calculations referred to, internal damping of the uniform precession mode due to relaxation mechanisms in the ferrite are neglected, it being assumed that the time intervals involved in the experiment are shorter than the relaxation times for the material. In samples of single crystal YIG this condition is well satisfied in practice, for experiments of the type to be described below. The assumption that H_p is a linear function of time is also well satisfied in practice, with the exception of a quadratic component in H_T near the origin, the effect of which has also been evaluated using the computer.

The function of the pulsed magnetic field may be divided into two parts, the first being an excitation function resulting in establishment of a uniform precession oscillation of relatively high amplitude, and the second being a pumping function through which both the frequency and energy of this precession are increased as a function of time.

After the full growth of the uniform precession angle has been reached, the field H_p can, in principle, be increased indefinitely without appreciable change occurring in the angle Θ_ℓ . This portion of the pulsed field rise accomplishes the pumping function by means of which the frequency and energy associated with the uniform mode are
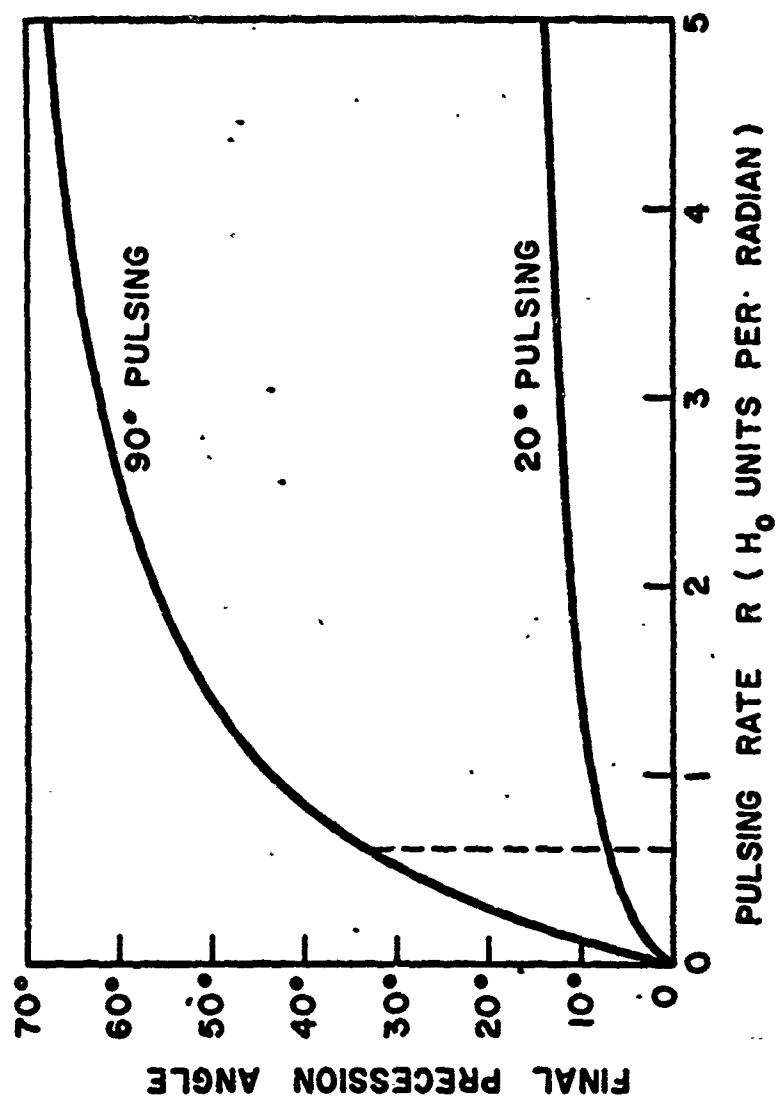
- 11 -

FIG. 4.—Final precession angle as a function of pulsing rate.

increased. As H_p increases in this range, H_T approaches H_p in magnitude, and the frequency and energy of the uniform mode become asymptotically proportional to the magnitude of H_T .

Figure 5 is an example taken from the computer results, using parameters $(dH_p/dt = 3$ kOe/nsec, $\psi_0 = 90^\circ$, $H_0 = 0.7$ kOe) which are sufficiently close to those used in the experiments described below that the curves give a good picture of the transient properties of the modes. The horizontal time scale applies accurately to the experiments. The curve labeled 1 illustrates the nature of the uniform-precession build-up. The peak value of Θ is reached at a time corresponding to 2.5 rad. calculated at the initial precession frequency of the uniform mode, namely $\gamma H_0/2\pi = 1.96$ Gc/sec. Thus the interval out to this point represents the region in which the essential function of the pulsed field is to establish the magnitude of the uniform precession, while the time interval beyond this point represents the pumping region in which the purpose of the pulsed field is to raise the energy and frequency of the precession at essentially constant precession angle. The curve labeled 1 represents the calculated energy of the uniform mode which is associated with the precession angle Θ . Note that this energy is normalized to the energy MVH_T , where M is the saturation magnetization of the ferrite and V is its volume. Since H_T is asymptotic to H_p , and H_p is assumed to be a linear function of time, the horizontal portion of the curve E_{UM} at large time actually represents energy increasing linearly with time.

The overshoot in Fig. 5, in which the uniform mode acquires an early amplitude which is noticeably larger than the asymptotic amplitude, is of interest. Although the experimental generators to be described below utilize the asymptotic value, the peak value which is reached earlier may be of some possible use. Under some parameter ranges the degree of overshoot can exceed that shown in Fig. 5. Figure 6 shows calculated values of the ratio of peak precession amplitude at the top of the overshoot to its asymptotic value, for various parameter adjustments. Figure 7 shows the normalized time at which the peak precession amplitude occurs.
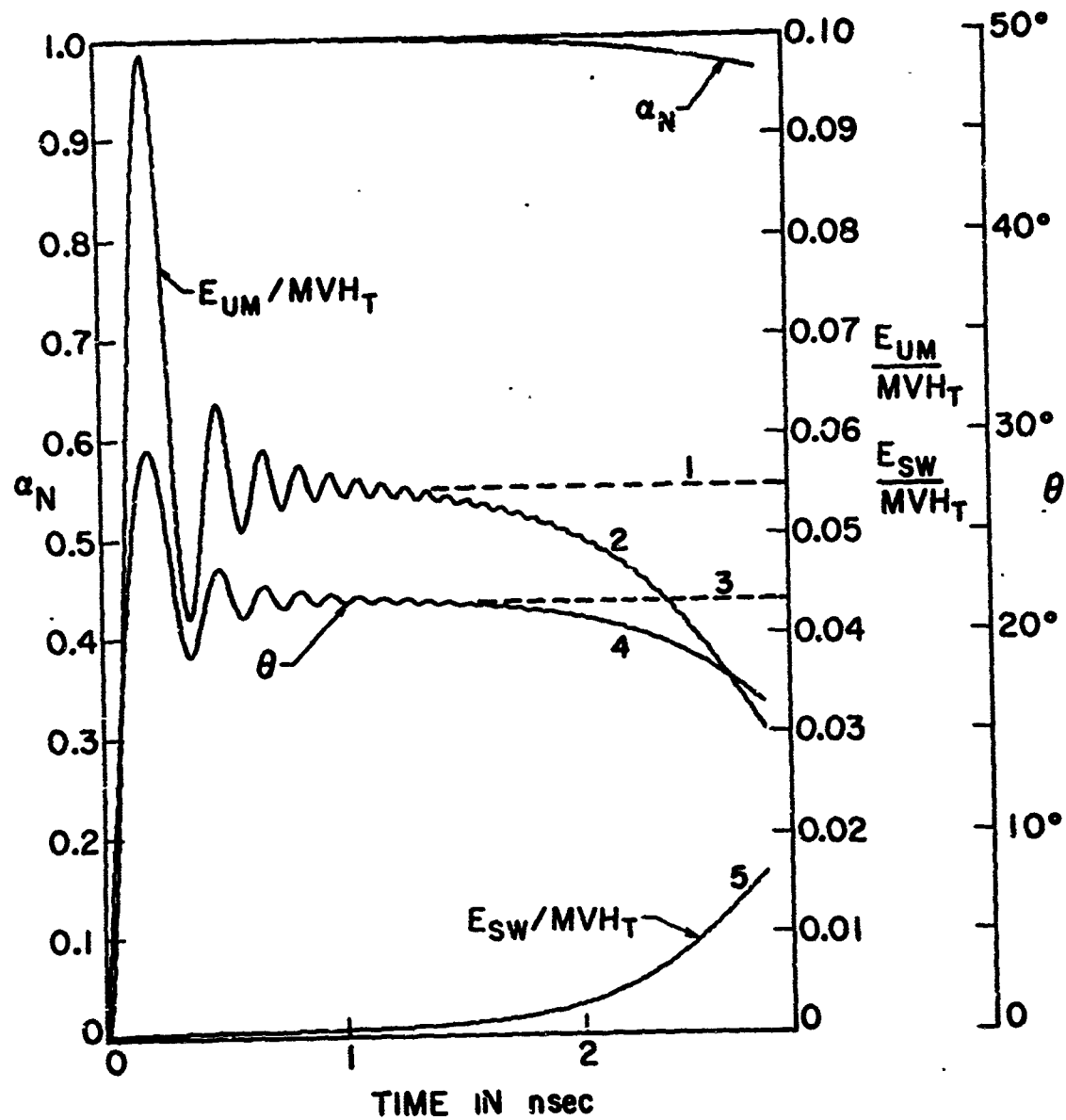
- 13 -

FIG. 5--Precession angle θ of the uniform mode, and normalized
energy of the uniform mode and spin waves, as a function
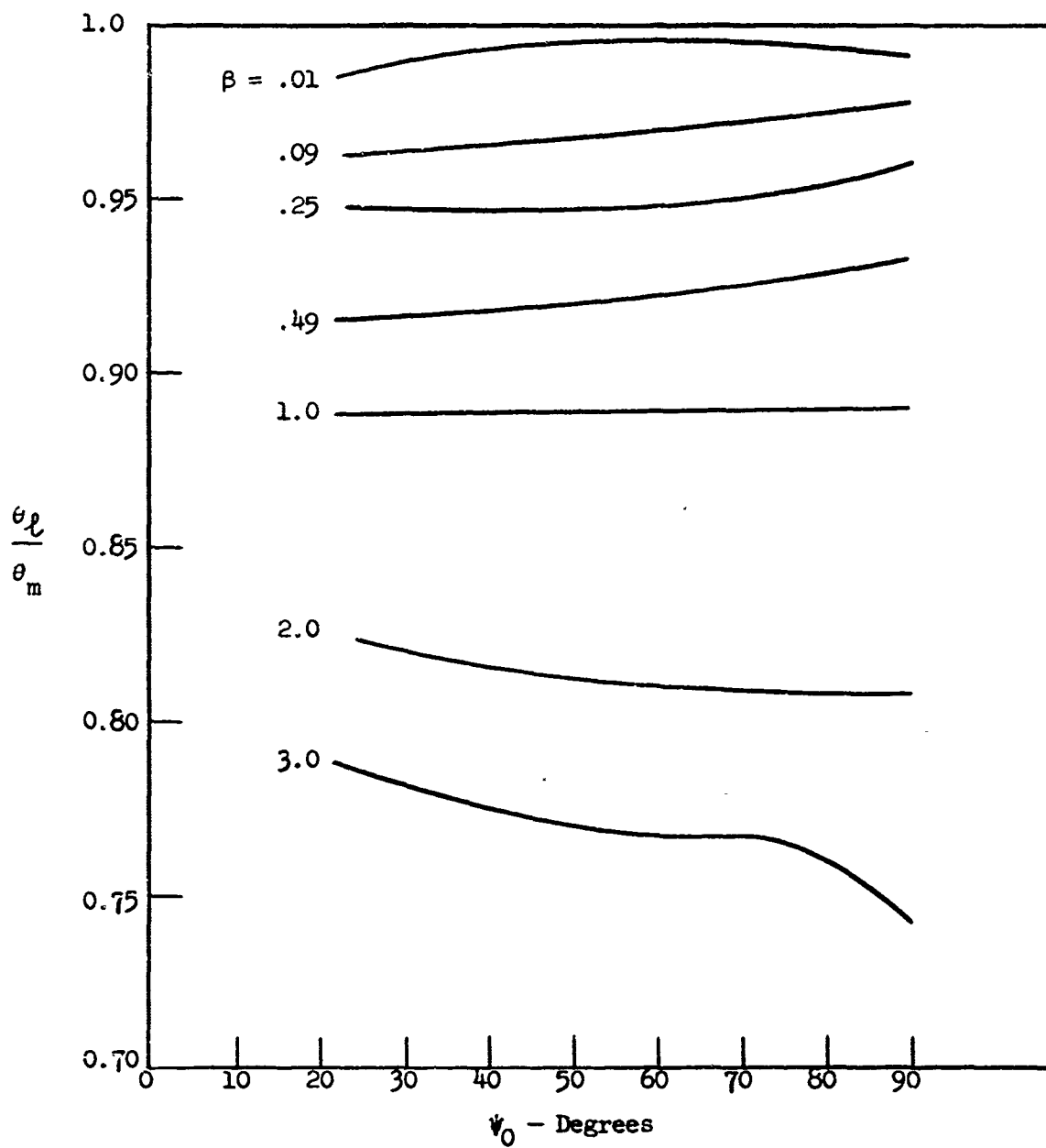of time.

FIG. 6--Ratio of final precession angle, θ_ℓ, to maximum precession angle θ_m vs pulsing angle, Ψ_0.
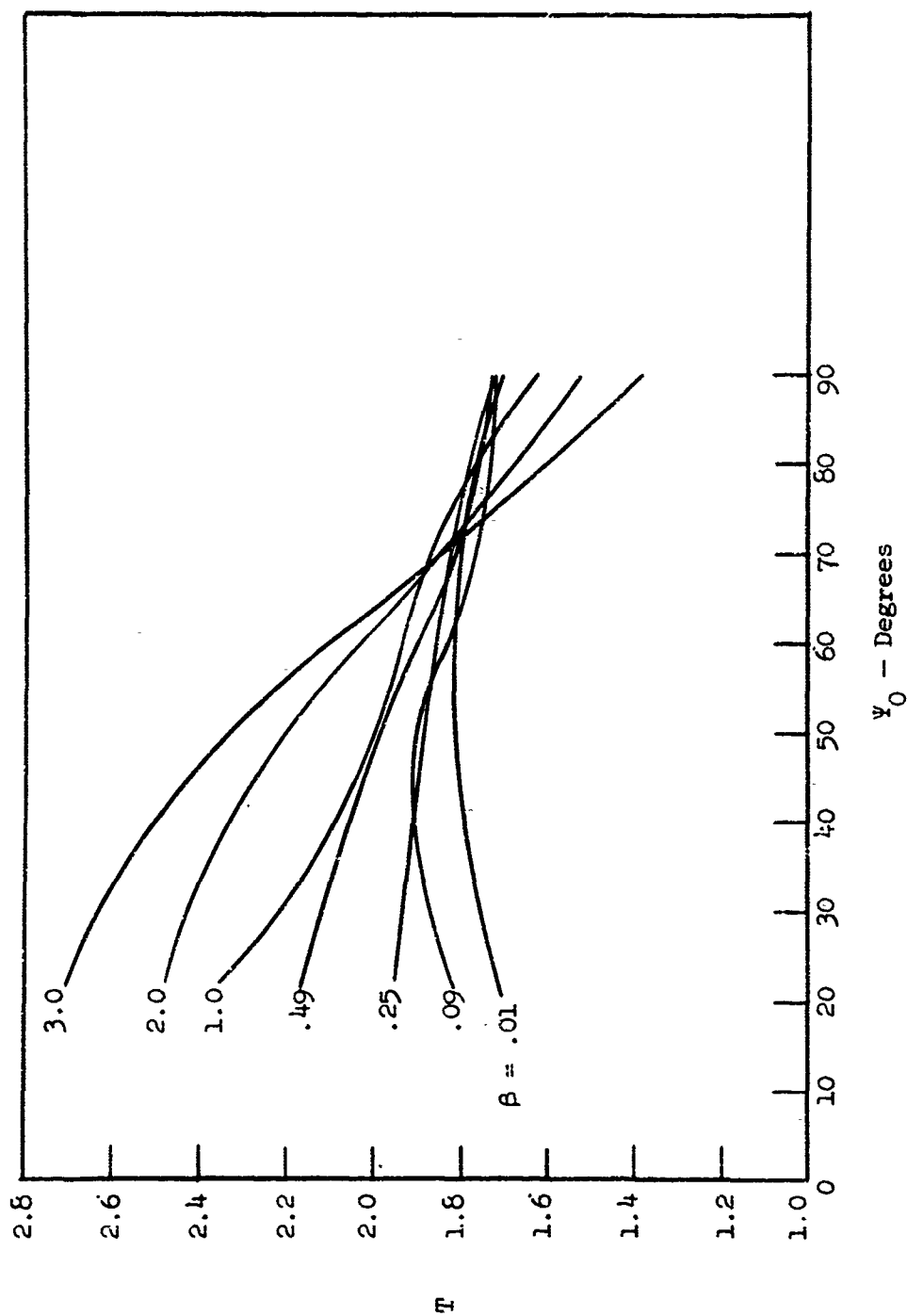
- 15 -

FIG. 7--Value of τ for maximum precession angle, Ψ , as a function of pulsing angle, Ψ_O .

B. Spin Wave Growth

A limitation on the operation of devices of the present kind results
from the intrinsic parametric pumping of spin waves, by which energy is
drawn from the uniform mode into spin waves where it is no longer avail-
able for useful extraction by radiation damping. In steady-state prob-
lems, spin wave phenomena of this kind have been widely studied and are
well known.[10-12] A study of the mechanisms of spin wave growth under
the present transient circumstances has been made using the digital
computer. This has been reported in a recent publication,[13] which
constituted part of the work under the present contract, and which gives
theoretical information on the detailed effect of spin waves on the
operation of the Type II generator. The material contained in this paper
is included in Appendix B below, for reference in the design of Type II
ferrite generators. In this investigation, the equations of motion for
spin wave modes in a ferrite subjected to linearly rising pulses of
magnetic field, for all regions of k-space which undergo pumping, are
integrated numerically, assuming initial spin wave excitation at the
level corresponding to thermal equilibrium. Again, no restrictions are
imposed on the values of H_0 , Ψ_0 , or dH_p/dt , and again the equa-
tions for the uniform mode are used in completely general form to allow
for arbitrary amplitude of the mode. In the spin wave equations, terms
to first order in the spin wave amplitudes are retained, and all spin
wave back-reaction terms are included in the uniform mode equations.
A numerical integration over k-space determines the aggregate of spin
wave growth as a function of time, and the energy in the uniform mode
as a function of time in the presence of the amplified spin wave.

Figure 8 is a typical example which shows pictorially the growth,
as a function of time, of both the uniform mode and spin waves in the
ferrite when subjected to a pulsed magnetic field of the type being
considered here. Figure 8 is a view looking down along the axis of the
net instantaneous field. The tip of the vector representing the instan-
taneous field is considered to be located at the center of coordinates
in the figure, and the plane of the paper is taken to be normal to the

- 17 -
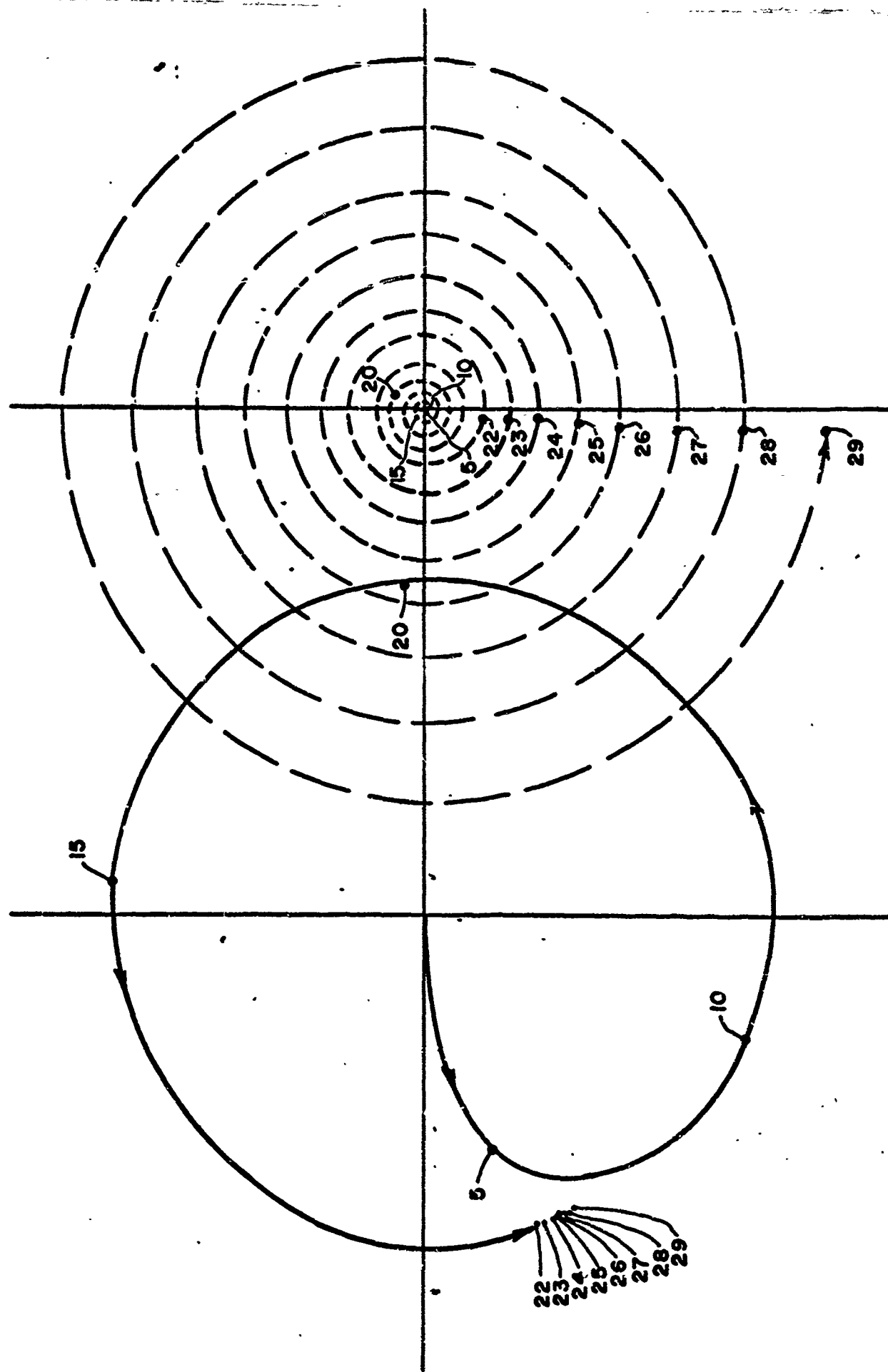
SPIN WAVES

UNIFORM MODE

net field vector. Thus, as the direction of the net field vector rotates in time, the observer is assumed to move correspondingly. The curves in Fig. 8 represent loci of the magnetization vector as a function of time. For example, if the circular uniform precession of Fig. 1(a) were represented in this kind of a diagram, the locus would consist of a circle with its center at the center of the coordinates in the figure.

The diagram of the uniform mode in Fig. 8 shows the build-up of the uniform precession as a function of time, illustrating the rotation of the magnetization vector about the axis of the instantaneous magnetic field. Note that the precession amplitude reaches essentially its full value before the magnetization has precessed one-fourth revolution. The numbered points on the uniform mode diagram are simply specific points which are used to correlate with corresponding points in time on the spin wave diagram. Considering the points on the uniform-mode locus labeled 22 - 29, each of these points in turn represents a point on a successive precession cycle. For example, the magnetization vector makes one complete revolution in traveling from point 22 to point 23, in a precession which is essentially circular and of constant amplitude, and the same holds for the other consecutive pairs of points.

The dashed diagram in Fig. 8 represents the corresponding build-up of spin waves which are pumped by the uniform precession mode. Actually the center of coordinates for both the solid and dashed diagrams should be coincident because both of these diagrams represent precessions centered on the same instantaneous field vector. However, for clarity, these two coordinate systems are displaced in the figure. The numbered points on the spin wave diagram correspond in time to the points bearing the same numbers on the uniform mode diagram. We see that the spin wave precession has negligible amplitudes for the first several cycles and then begins to spiral upward rapidly. We also note that the spin wave magnetization pulls into a steady time phase which is something less than 45° ahead of the uniform precession phase as time goes on.

For a more detailed picture of the spin wave build-up process and its effect on the uniform mode we return to Fig. 5 which, as stated above, is calculated for parameters which are sufficiently close to

those used in experiments on the Type II generator to give a very useful picture of the build-up process, as a function of time, as it occurs in the actual experiments. Note that the back-reaction effect of spin waves on the uniform mode, which is included in the graph of Fig. 5, was not taken into account in calculating the diagram of Fig. 8. In Fig. 5 curve 5 indicates the growth of total spin wave energy as a function of time. The effect of this spin wave growth on the precession angle θ of the uniform mode is indicated by curve 4, and similarly the decrease in uniform mode energy is shown by curve 2, representing energy associated with the uniform mode. We see that these theoretical curves predict that in a time of approximately 2 nsec the energy associated with the uniform mode has been degraded by approximately 10%, by the presence of spin waves, from the value which it would have without spin waves. The uniform mode energy decreases rapidly beyond this point. On this basis, one should design the experiment such that the energy removal by radiation damping of the uniform mode occurs before the elapsed time exceeds 2 nsec.

For any given set of parameters, the theoretical effect of spin waves on the amplitude of the uniform precession mode may be determined from the material in Appendix B. Recall that in the absence of spin waves, the uniform precession mode reaches an asymptotic value. It then remains at this asymptotic value until the usual, linear relaxation processes cause it to decrease. As has been stated above, the linewidth of low loss YIG materials is such that the linear relaxation methods do not come into play during the time interval involved in the generation and radiation of an rf pulse in the present type of device. In one formulation of the problem of the effect of spin waves on the uniform mode, then, we calculate the time involved, from the beginning of the magnetic field pulse, until nonlinear spin wave growth has proceeded to the extent that the energy in the uniform mode has been reduced to 10% below the value corresponding to the asymptotic amplitude of the uniform mode in the absence of spin waves. It is found that a universal curve for this time interval can be plotted which holds for an arbitrary combination of pulsing parameters. This curve is given in Fig. 4 of

Appendix B. The vertical scale is in terms of the asymptotic value of the uniform precession mode, irrespective of the combination of pulsing angle and initial pulsed-field slope which is used to achieve this asymptotic precession angle. The horizontal scale is the normalized time at which the uniform mode has been degraded 10% in energy by the spin-wave build-up. The values on this horizontal scale represent time in radians as measured at the initial precession frequency. As has already been seen, the initial precession frequency is determined entirely by the magnitude of the applied dc magnetic bias field. In Fig. 9 below this same curve is shown replotted using a horizontal time scale in terms of actual time in nanoseconds for the particular case in which the dc bias field is 700 Oe, which is the value used in most of the experiments described below. We see that a total time of the order of 1.5 nanoseconds is theoretically available in which to carry out the experiment of generation, translation and radiation of an rf pulse, if noticeable degradation of energy due to spin wave effects is to be avoided. Note that radiation damping of the rf output coupling in the crossover range is not included in the calculation, so that the prediction of Fig. 9 is actually pessimistic. It is clear, however, on the basis of these calculations, that one should attempt to reach the crossover region in a time of the order of one nanosecond, and this is the essential consideration which controls the total build-up time of the pulsed magnetic field. In summary, then, the requirements on non-adiabatic excitation of the initial uniform precession oscillation, as described in an earlier section, determine the requirement of the initial time-rate-of-rise of the pulsed magnetic field, while the present requirement defines the total rise time of the field up to the crossover region. It will be seen later that the actual pulsed magnetic field waveform developed in connection with the present project was designed to take these two requirements into account. It will also be seen that the total rise-time requirement has been better met than the initial rate-of-rise requirement, and that it can be anticipated that progress in the latter area would directly increase the peak power output of the device.
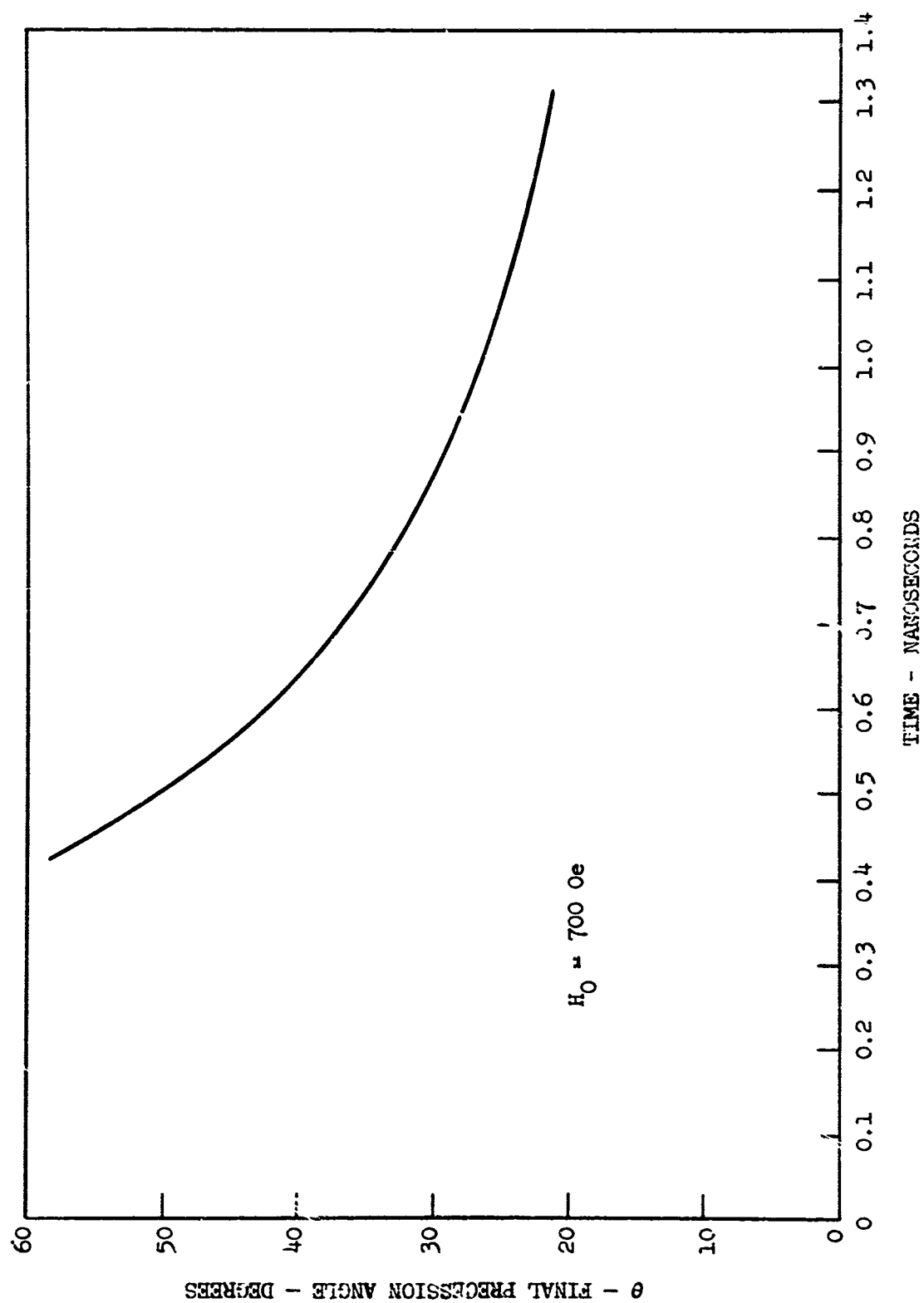
- 21 -

FIG. 9—Theoretical spin-wave buildup time.

C. Coupled Circuit Behavior

Radiation damping for extraction of energy from the ferrite at the desired frequency is provided by a coupled circuit resonator which is described below. This resonator, and the uniform mode resonance in the YIG sample, constitute a coupled circuit system. As the oscillation frequency of the uniform mode is swept through the resonant frequency of the circuit mode, a transfer of energy to the circuit takes place.

We use the equivalent circuit of Fig. 10 to simulate the behavior of this coupled system, in which we identify the ferrite with circuit 1 and the circuit resonator with circuit 2. The system consisting of these two coupled circuits contains two normal modes, which we will refer to as Modes A and B, as illustrated in Fig. 11. In the present problem, at the start of the pulse the resonant frequency ω_1 of circuit 1 is much less than the resonant frequency ω_2 of circuit 2, and the energy of the system is almost completely stored in Mode A. As ω_1 is swept upward in time, through the region of cross-over with the frequency ω_2, the energy transferred to circuit 2 depends on the sweep rate as well as on the circuit parameters. If the sweeping is sufficiently slow, the fields in the resonators readjust themselves as functions of time to essentially preserve Mode A, and the energy, which was originally stored in circuit 1, is nearly all transferred to circuit 2, as desired. In the other extreme, if the sweep rate is sufficiently high, a great deal of mode conversion takes place during cross-over, and the energy remains mostly in circuit 1, ending up in Mode B.

In the present experiments, an intermediate sweep rate is used, and computer calculations were carried out to determine the theoretical efficiency of transfer of energy from circuit 1 to circuit 2 during cross-over (see Appendix C). In this process the frequency ω_2 is held fixed, and ω_1 is assumed to vary with time as

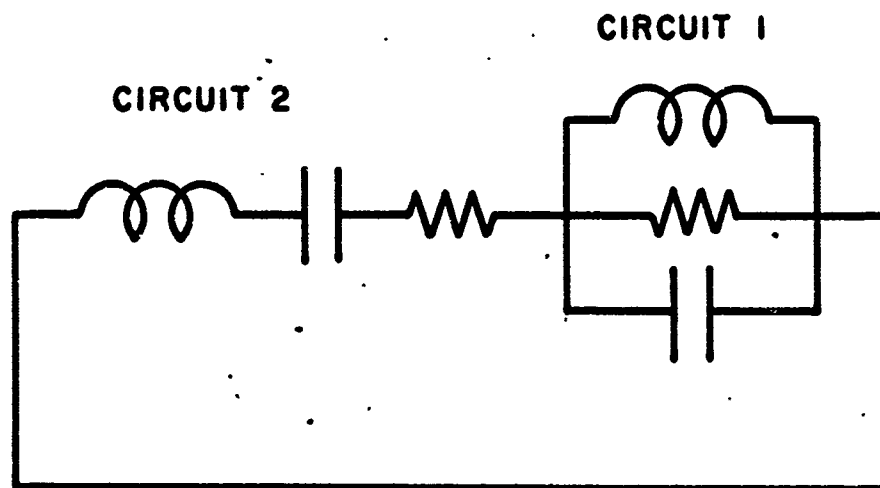$$\frac{\omega_1}{\omega_2} = A + B\tau \quad , \tag{1}$$

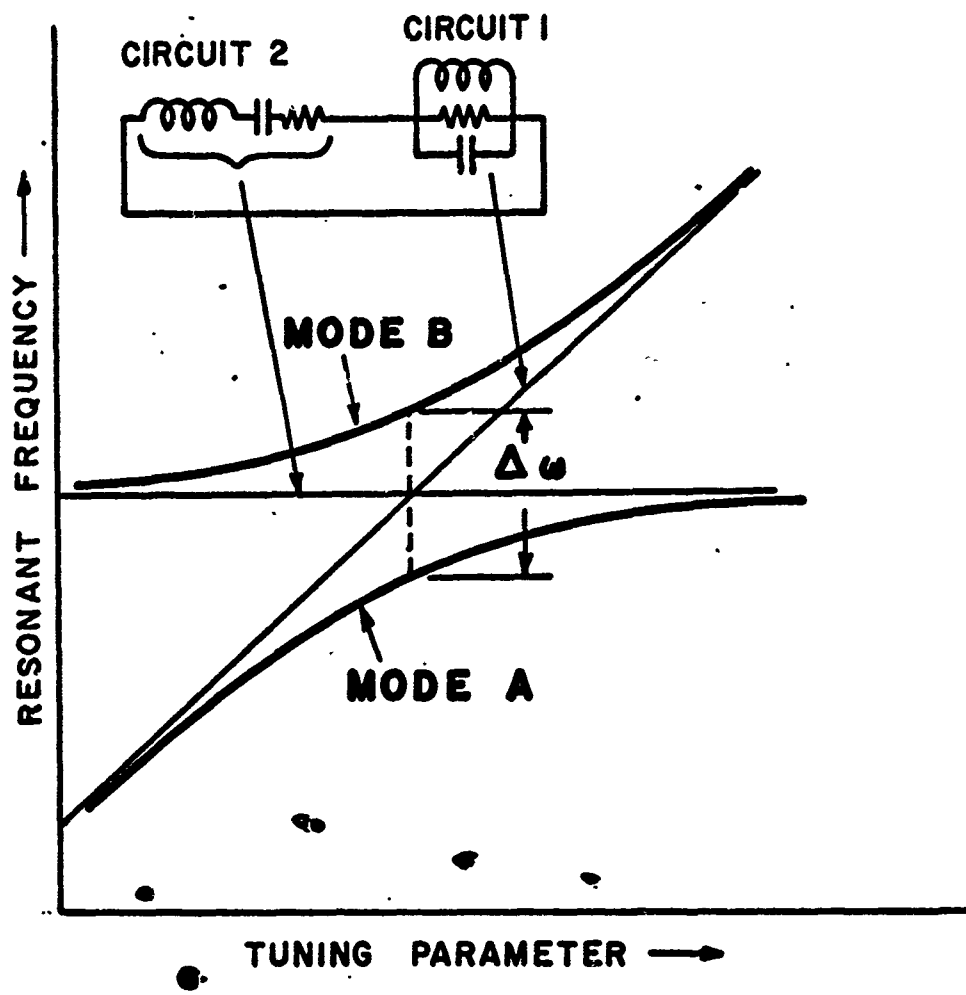FIG. 10--Equivalent circuit of coupled ferrite and circuit resonator.

FIG. 11--Illustration of coupled circuit modes.

where $\tau = \omega_2 t$. Figure 12 is a computer plot which illustrates typical behavior of the energies in circuits 1 and 2 as a function of time. The parameter values chosen for this figure are consistent with those used in experiments described later. The values are $A = 0.1$, $B = 1/20\pi$, $\kappa = 0.004$, $Q_1 = 1,000$, and $Q_2 = 50$. With the values of A and B shown, cross-over is reached at a time corresponding to nine periods at frequency ω_2 . Cross-over occurs at the time indicated by the vertical dashed line in Fig. 12. The parameter κ specifies the strength of coupling between circuits 1 and 2, and is related to the frequency separation of Modes A and B at cross-over by the expression

$$\kappa = \left(\frac{\omega_B - \omega_A}{\omega_2} \right)^2 \quad . \tag{2}$$

The quantity Q_1 represents the unloaded Q of circuit 1, while Q_2 is the loaded Q of resonator 2, including the loading due to an output waveguide to which the resonator is coupled. Calculation of the total energy per sweep delivered to circuit 2 shows this energy, for the case of Fig. 12, is 29% of the energy which would be stored in circuit 1 at cross-over in the absence of circuit 2, which latter value is indicated by the intersection marked U in the figure.

The dependence of this energy transfer efficiency on the coupling coefficient κ , for values of Q_2 of 50 and 100, and with all other parameters as in Fig. 12, is shown in Fig. 13. A family of curves showing the energy transfer ratio as a function of Q_2^{-1}, for several values of κ , is presented in Fig. 14. The curves of Figs. 13 and 14 were calculated using data taken from sets of computer curves of the kind shown in Fig. 12.

While the value of κ used with Fig. 12 is comparable to that involved in the experiments below, we note from Fig. 13 that a design using higher coupling coefficients could materially improve the energy transfer efficiency of the coupled circuits. We also note from Fig. 13 that the energy transfer ratio is predicted to be very insensitive to Q_2 , the loaded Q of the output circuit.

- 26 -
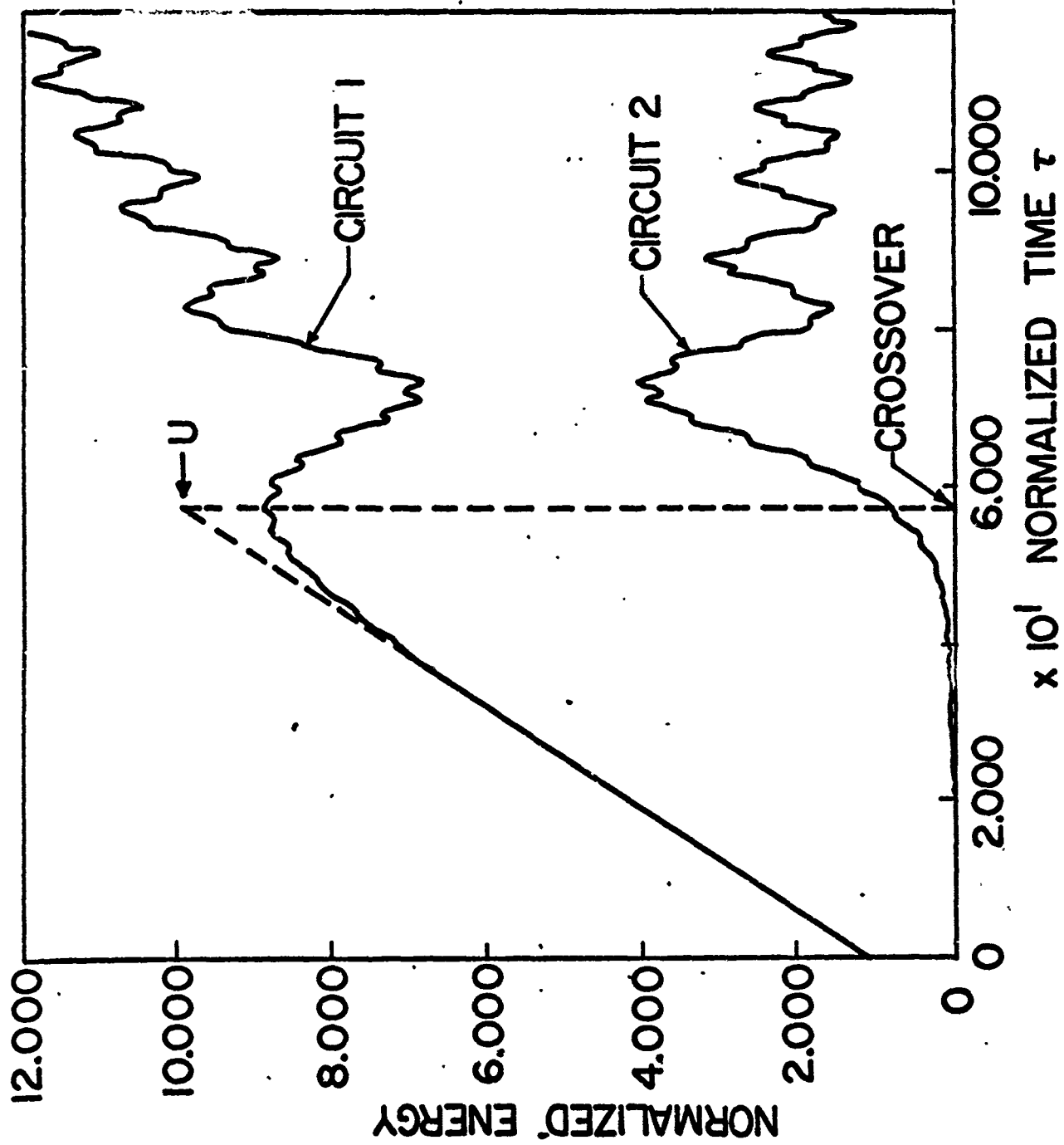
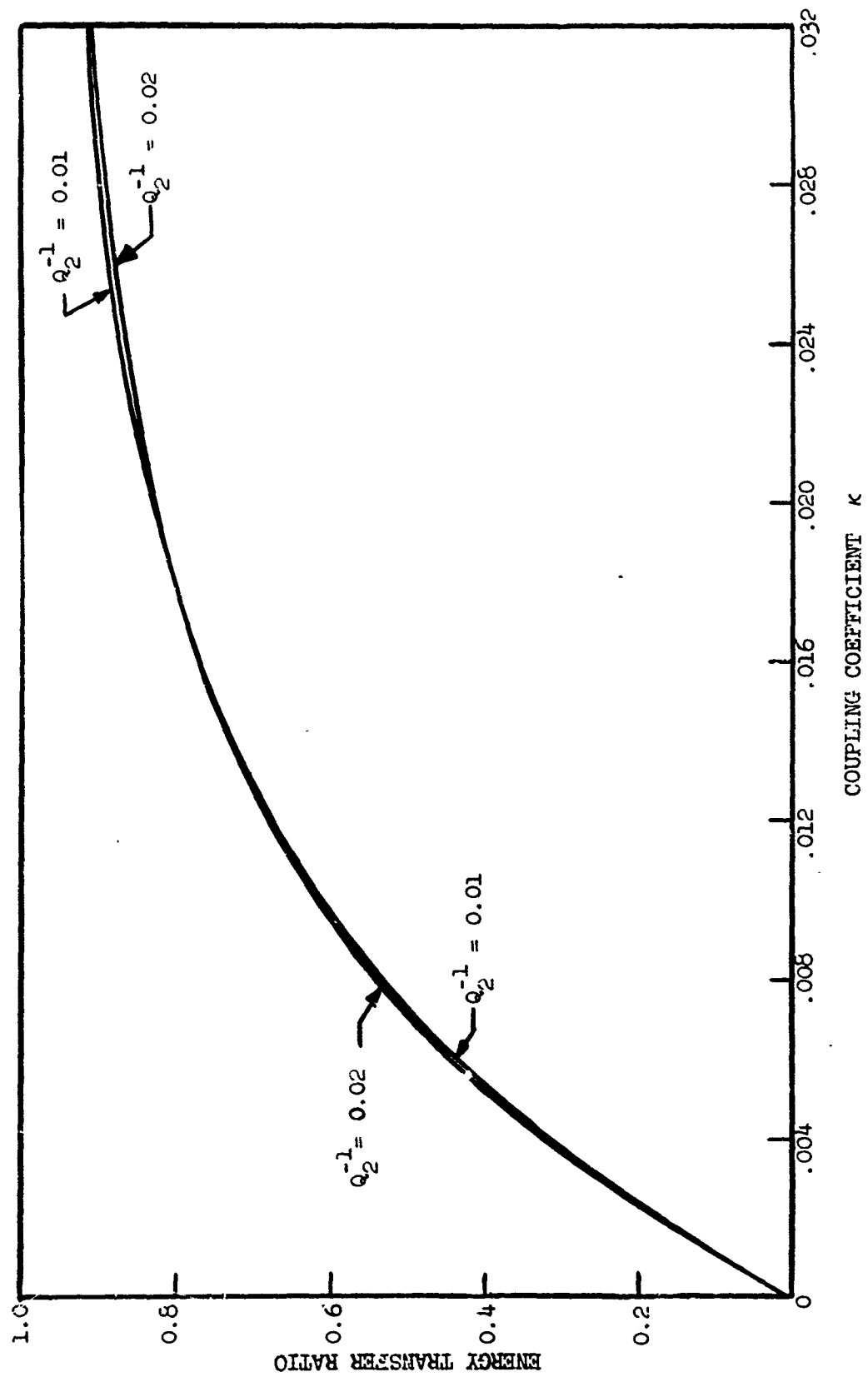FIG. 12.--Theoretical energy transfer etween ferrite and circuit as a function of time.

FIG. 13—Theoretical energy transfer ratio between ferrite and circuit as a function of coupling coefficient κ, with Q_2^{-1} as a parameter.
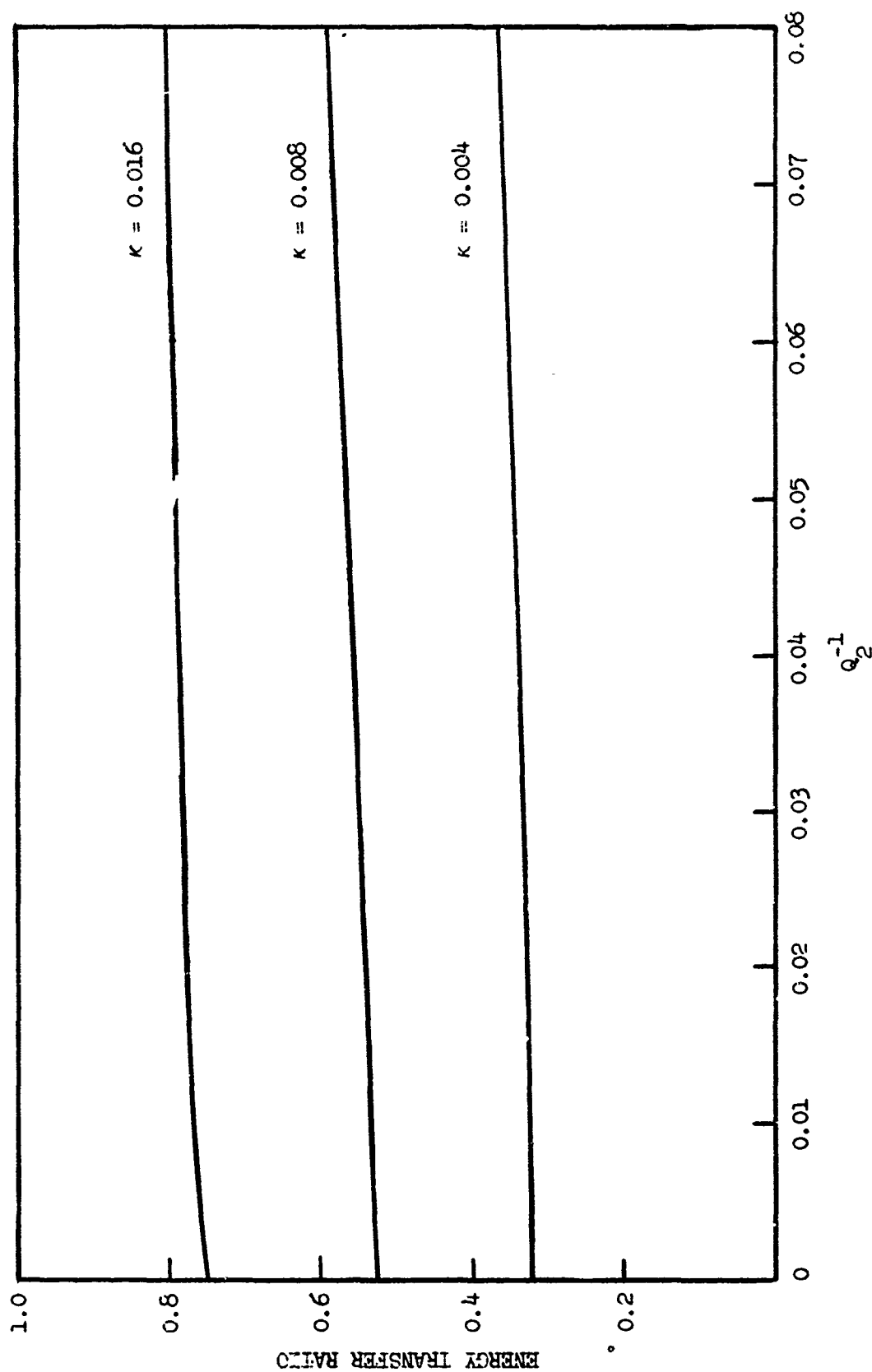
FIG. 14.—Theoretical energy transfer ratio between ferrite and circuit as a function of Q_2^{-1}, with coupling coefficient, κ, as a parameter.

III. PULSER DESIGN

Under the program on this contract a significant amount of effort was devoted to developing pulsed field generators having the characteristics required for high power operation of the Type II generator. As shown earlier in this report, the principal requirements are concerned with the initial time-rate-of-rise of the pulsed field, the total time required to reach the peak value, and the field magnitude at the peak value of the pulse. For an experimental program having the objectives of the present contract, spark gap switches have consistently appeared to represent the best solution. Surveys of other types of switches indicated that they were generally lacking either in total current handling capacity or switching rate, or that the complexity and development time involved could be expected to greatly exceed that involved in the case of spark gaps. As has been stated above, the objective of the present program was to test experimentally whether the Type II generator was capable of producing high power microwave pulses, and in order to focus the effort on this objective it was desirable to achieve the necessary pulsed field characteristics in the simplest and most direct way. The spark-gap and strip-line pulser approach performed this function satisfactorily. This is not to imply, at this point, that the spark gap approach would necessarily be best in a practical device development, as the comparisons between spark gaps and other possible approaches would have to be made on the basis of fully engineered systems and taking into account questions of lifetime and various practical and environmental factors.

The pulsed magnetic field is obtained by passing a current, in the form of a short, steeply rising pulse of high amplitude, through a single-turn coil which is described later. Typical magnitudes involved are a current amplitude of some 1.5 kA with a pulse width of several nanoseconds, and pulse risetime of somewhat under 1 nsec in a coil having an inductance of the order of 1 nH. In this section we describe the pulser apparatus which was developed to meet these specifications.

- 30 -

The pulser system is illustrated schematically in Fig. 15. The general approach involves the use of a pressurized spark gap to switch a relatively high voltage on a low-impedance strip line, to produce a current pulse of high amplitude in the strip line, and subsequently steepening the front edge of this pulse by passing it through a second spark gap, which constitutes a nonlinear circuit element.

The charged line section on the right-hand end in Fig. 15 is charged to a dc voltage in the range of 10 - 20 kV, upon which is superimposed a 60 cps ac voltage in the range of 1 - 3 kV. The dc voltage is set below the breakdown voltage of the primary (right-hand) spark gap, and gap firing takes place near the positive peaks of the ac voltage, which assures a constant average pulse repetition frequency. Stable operation with two pulses per positive peak of the ac waveform is readily achieved.

The primary and sharpening spark gaps are similar in design. The gap electrodes are machined from copper or silver-tungsten matrix such that the radius of curvature of the firing surfaces is greater than their spacing. Gap spacing is continuously adjustable during operation. Both gaps are enclosed in pressure chambers suitable for gas pressures up to some 15 atm. A drawing of the gap and chamber design is given in Fig. 16.

A large number of experiments were performed, aimed at optimizing the pulser performance as a function of all available parameters, such as characteristic impedance and geometry of the strip lines, the design of strip line junctions, gap electrode shapes, materials, and spacings, and gas type and gas pressure. Figure 17 is typical of curves obtained from sampling scope presentations of the leading edges of both unsharpened and sharpened voltage waves on the output strip line, with the various pulser parameters set near their optimum values. These voltage waves are viewed by tapping across the output line at the point V in Fig. 15 located halfway along the length of the line.

In the system of Fig. 15 all sources of reflection of traveling waves are isolated timewise from other circuit elements, to avoid reflection errors and to avoid any traveling wave resonance effects.

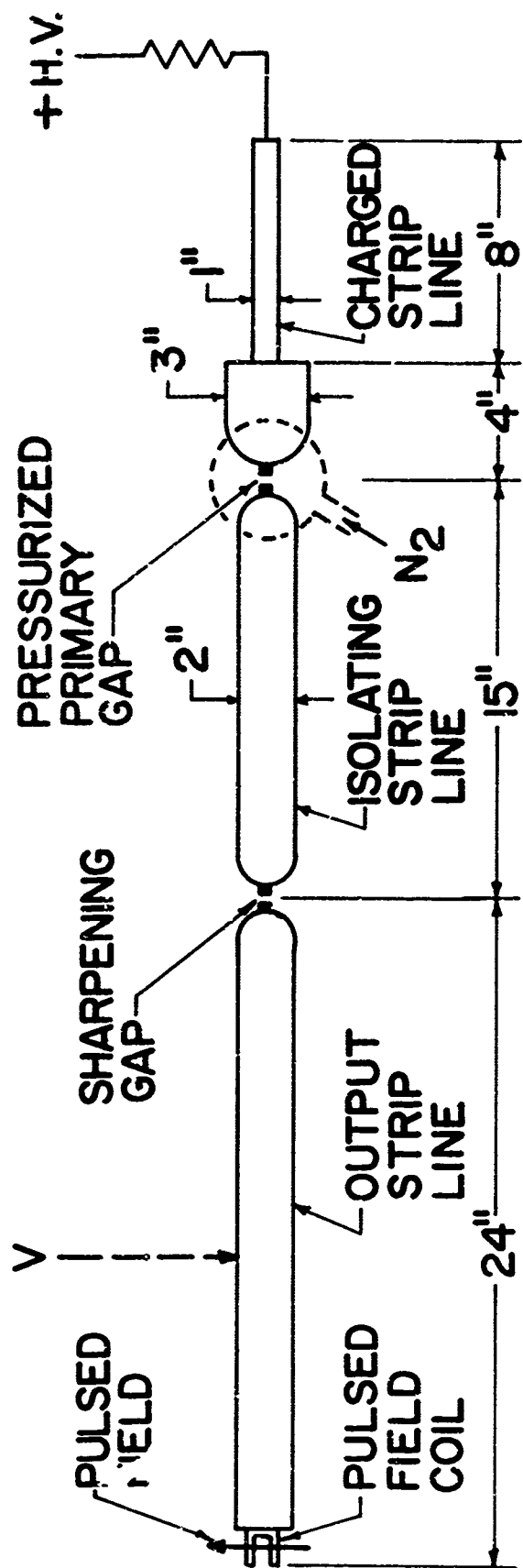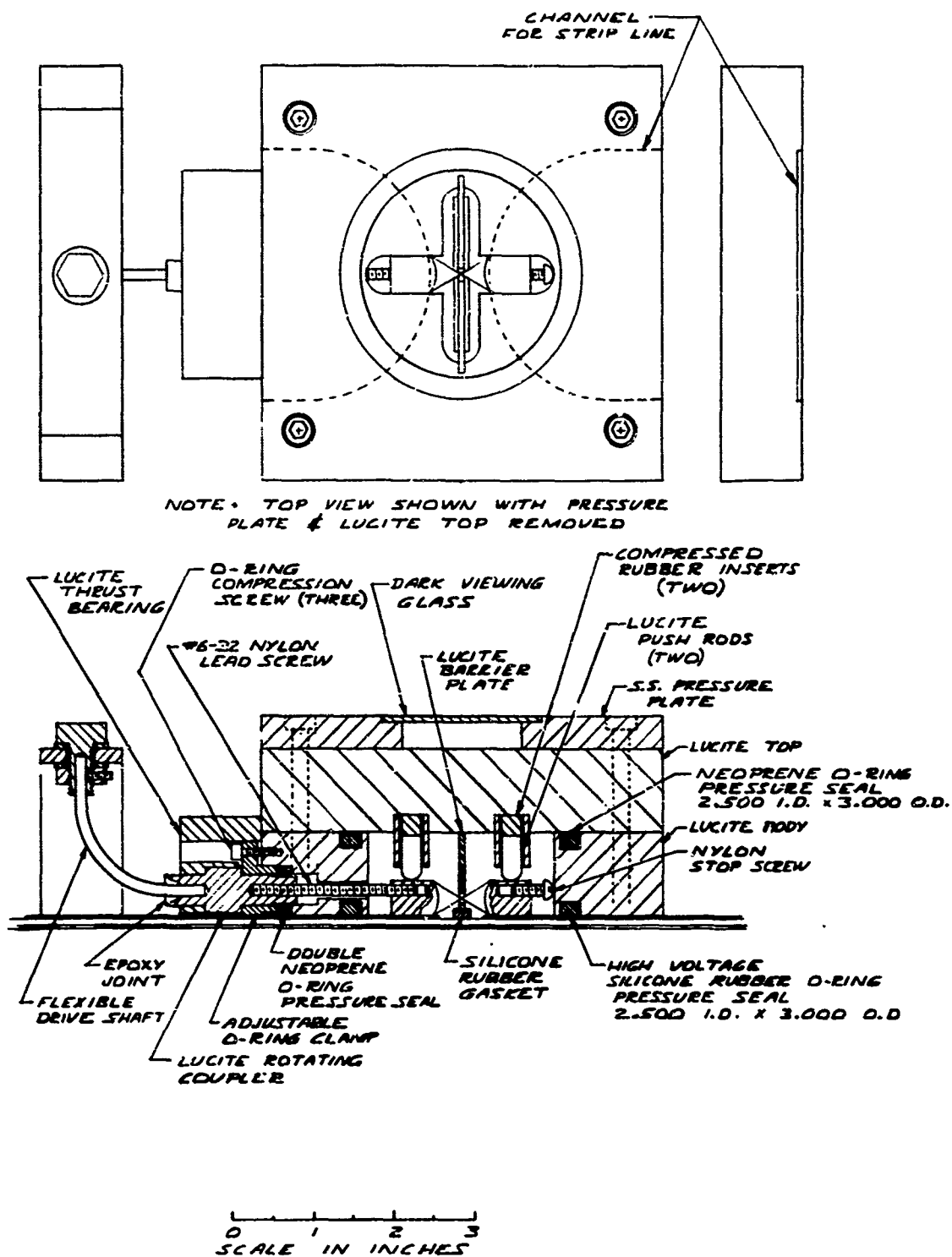FIG. 15--Strip-line layout for 7.6 ohm pulser (not to scale).

- 32 -

NOTE: TOP VIEW SHOWN WITH PRESSURE
PLATE & LUCITE TOP REMOVED
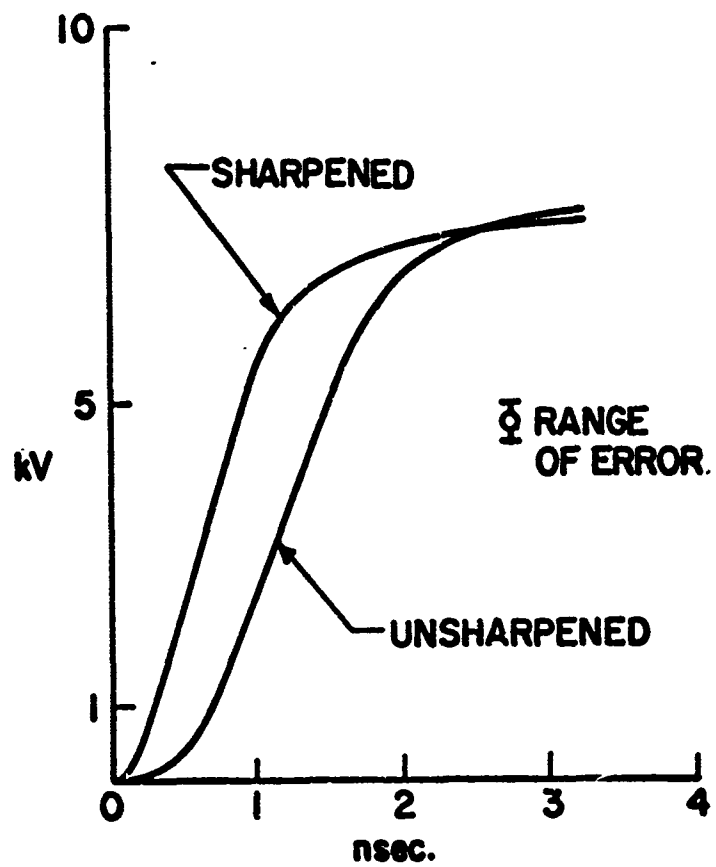
FIG. 16--Spark gap pressure chamber.

- 33 -

FIG. 17--Sharpened end unsharpened voltage waveforms on
output strip line.

The middle and output strip line sections have characteristic impedance of 7.6 Ω, as there was found to be a broad minimum in overall pulsed field risetime in the vicinity of this impedance level. These lines are constructed of copper strip of width 2 in. spaced 0.060 in. from a copper ground plane by sheet Mylar dielectric. This spacing avoids nonlinear effects in the dielectric material which were found to be troublesome at insufficient spacing. In the primary gap, nitrogen at a pressure in the vicinity of 100 lb/sq. in. provides a good compromise between risetime and gap voltage drop. Primary gap spacing is typically of the order of 0.020 in. Pressurizing of this gap improves its switching time by a factor of about 20 over atmospheric pressure operation. Pressurizing of the sharpening gap was found to provide no improvement of its functioning.

To produce the pulsed magnetic field H_p , the pulsed voltage wavefront of Fig. 17 is incident upon a single-turn pulsed field coil which provides essentially a short-circuit boundary condition at the left-hand end of the output strip line of Fig. 15, so that the final value of coil current is approximately $2V_p/Z_0$, where V_p is the instantaneous magnitude of the incident pulsed voltage wave and Z_0 the characteristic impedance of the output strip line.

The pulsed field coil is a single-turn loop machined in a brass fixture as shown in Fig. 18, which combines the pulsed field coil and a coupled rf circuit resonator, which is discussed later, in a single integrated element. The input leads to the loop indicated in the figure are connected directly to the strip line current source, resulting in a pulsed field directed along the axis of the loop. The YIG sample, which is not shown is located at the center point of the loop.

The loop itself is separated into two halves by means of a transverse saw cut made at the midpoint of its longitudinal axis. These two halves are spaced a finite distance and are parallel-connected with respect to the pulsed driving current.

In one design, the unit of Fig. 18 is mounted in an x-band waveguide flange as illustrated in Fig. 19. The flange introduces a shunt path for pulsed currents in parallel with the regular coil path, which is

- 35 -

PULSED FIELD
COIL AXIS

PULSED FIELD
COIL LEADS

X-BAND
RESONANT
SLOT

0   1/4"
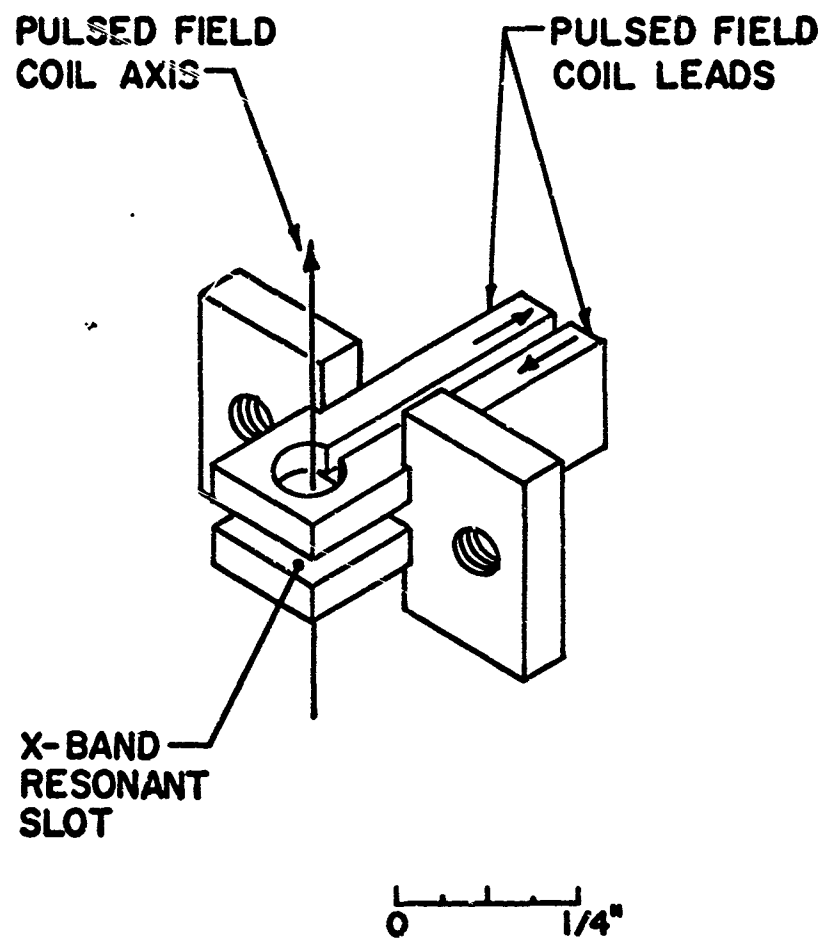
FIG. 18--Circuit element containing pulsed field coil and
X-band slot resonator.

STANDARD RECTANGULAR
WAVEGUIDE

PULSED FIELD COIL
AND SLOT RESONATOR

HOLE FOR FERRITE
SAMPLE HOLDER

COPPER STRIP-
LINE

WAVEGUIDE
TUNING
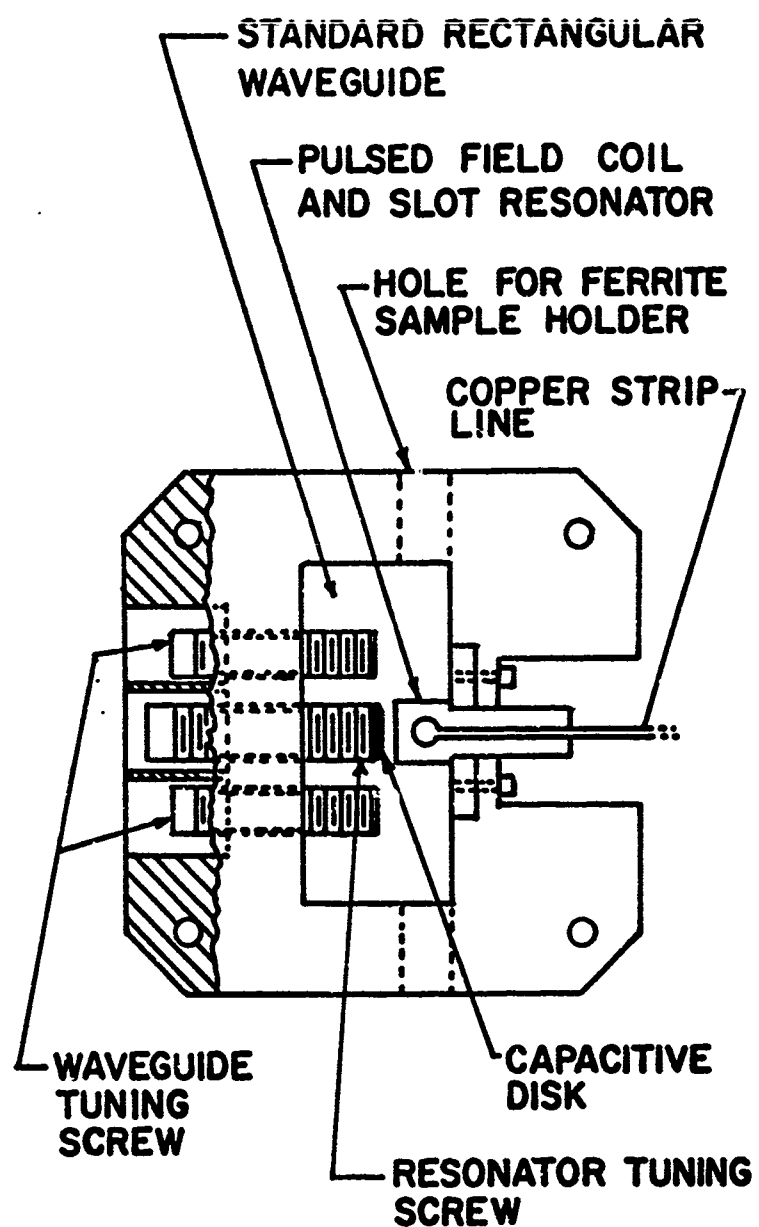SCREW

CAPACITIVE
DISK

RESONATOR TUNING
SCREW

FIG. 19--X-band waveguide coupling structure.

found to decrease the current in the coil by the order of 10%. The interfaces between this flange and external waveguide flanges, with which it mates on both sides, contain sheet lucite spacers which are essentially transparent to waveguide signals but prevent shorting of pulse current by the external waveguides. Chokes are used to prevent rf leakage between the flanges.

With the dimensions indicated in Fig. 18, the ratio of field to current for field at the center point of the loop is 2.75 kOe/kA. The inductance of this pulsed field coil is approximately one nanohenry which, in the 7.6 Ω strip line circuit, has a calculated risetime of 0.13 nsec.

The measured leading edge of the pulsed field waveform generated by the above circuitry is shown in Fig. 20. It is seen that this pulse is substantially linear over three-fourths of the region shown, with a slope of 5 kOe/nsec. However, the initial portion consists of a parabolic section which joins the linear portion with continuous first derivative at the point labeled the junction point.

The slope of the linear portion of this pulsed field waveform corresponds to a rise rate R of 0.6 when the dc bias field is 0.7 kOe. The dashed line in Fig. 4 shows that, when the angle between the pulsed field and the dc field is 90°, the present R value of 0.6 units should lead to a final precession angle of 32°.

The theoretical effect on the final precession angle of the initial parabolic portion of the pulsed field waveform is shown in Fig. 21. This is one of a family of such curves obtained from the digital computer. The horizontal scale is in terms of the number of radians, at the initial precession frequency, required for the pulsed field to reach the field magnitude corresponding to the junction point. In the pulsed field waveform of Fig. 20 the number of radians required to reach the junction point is six, and for this case the curve of Fig. 21 predicts a theoretical final precession angle of 13°.
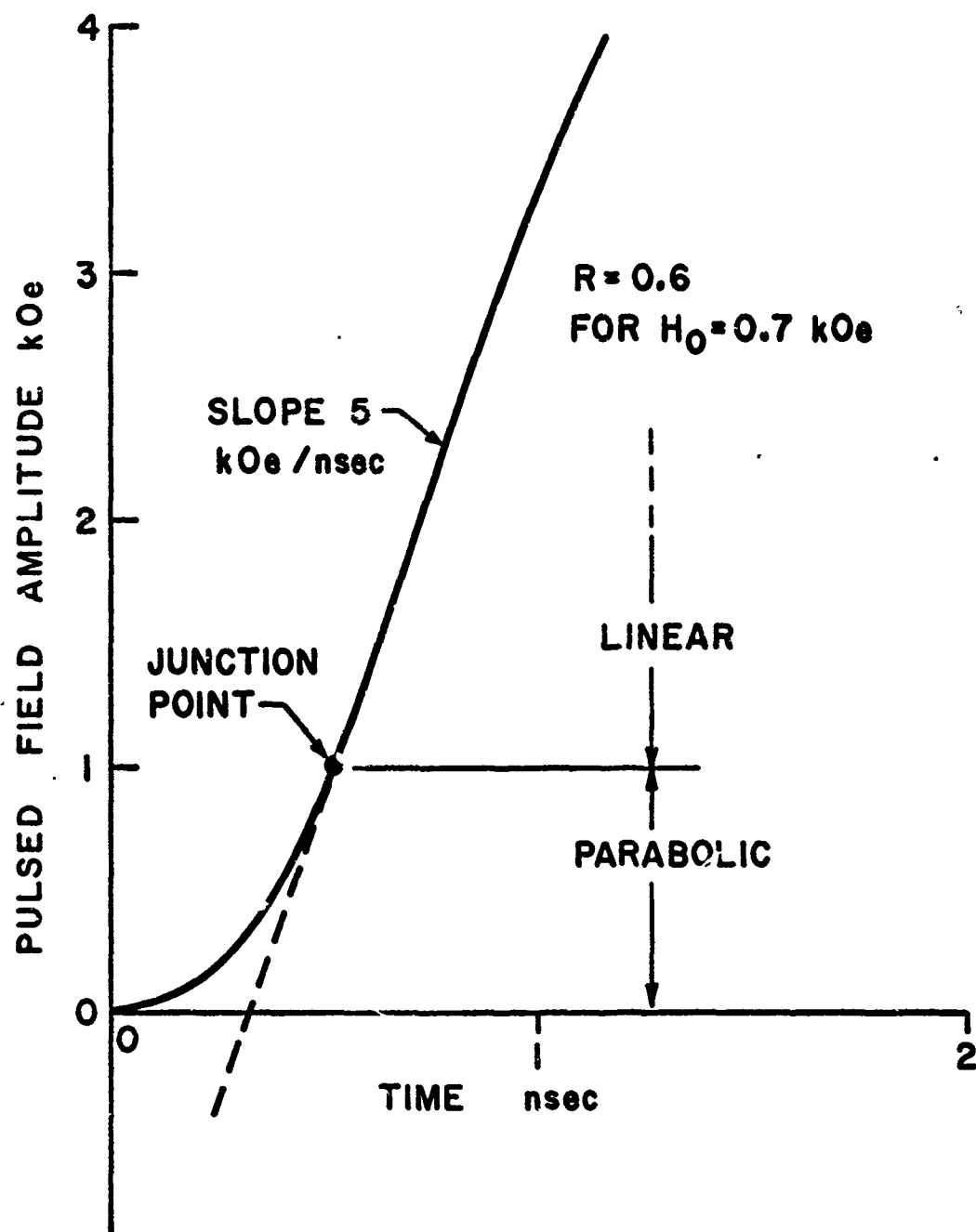
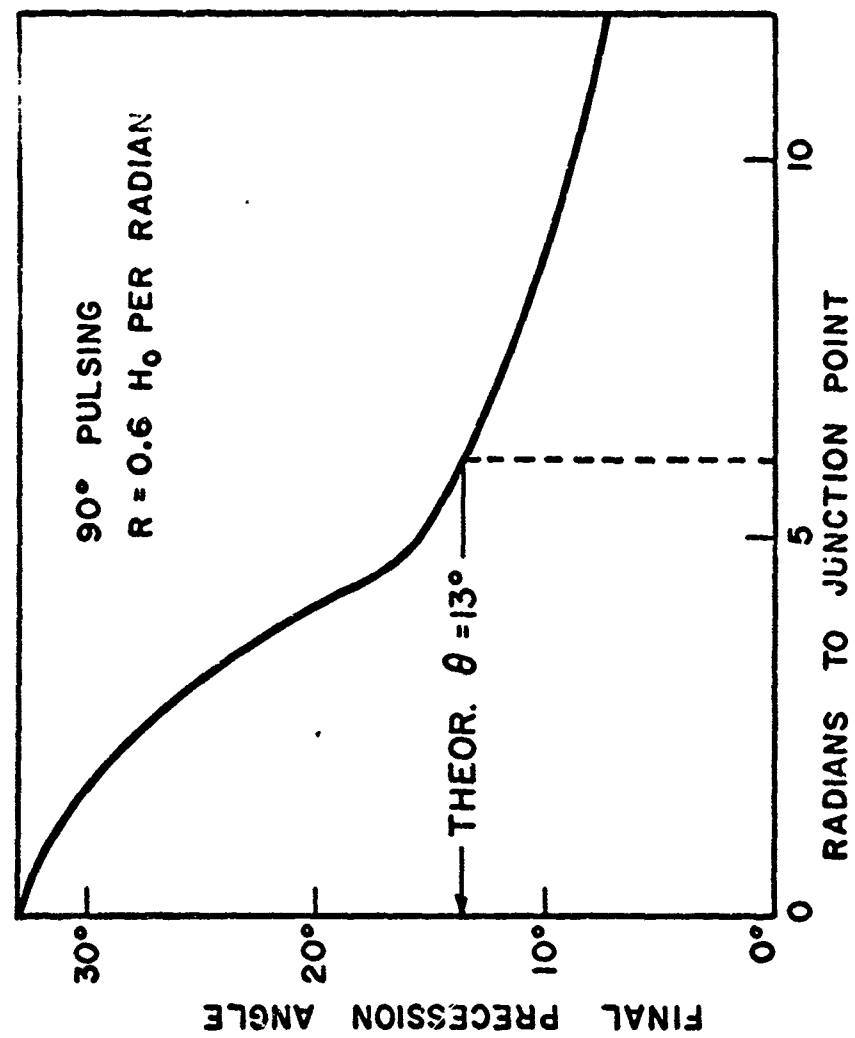FIG. 20--Measured pulsed field leading edge.

FIG. 21--Computer calculation of the final precession angle for a pulsed field having initial parabolic rounding.

IV. CIRCUIT DESIGN

The separation of the pulsed field loop into two halves forms a slot resonator which resonates in the x-band frequency range. The symmetry of this arrangement is such that the normal mode fields of the slot resonator are not coupled to the pulsed field circuit. The slot resonator, whose rf fields are linearly polarized and are oriented perpendicular to H_p, performs the function described above for circuit 2, extracting energy from the YIG sample by radiation damping.

With the coil-resonator assembly mounted in an x-band rectangular waveguide as in Fig. 19, the slot mode is tightly coupled to the TE_{01} waveguide mode. Also indicated in the figure is a capacitive tuner, consisting of a titanium dioxide disk whose spacing from the slot resonator can be varied, to accomplish tuning of the resonant frequency from approximately 7 to 10 Gc/sec. Control of the coupling between the resonator and the waveguide is afforded by means of an adjustable short located in the waveguide on one side of the resonator, and also by means of the two waveguide tuning screws which are shown.

As has been seen, the function of the present device is to convert energy from the source of the applied magnetic field into rf energy in an output waveguide. The function of the ferrite is to transfer the energy to the waveguide through the medium of the coupled circuit resonator. In this operation the ferrite behaves as a parametrically swept resonator and not as a simple linear transducer of energy in the Fourier components of the field pulse. In this connection, the latter are determined by the rate of rise of the field pulse, which is dictated by the initial precession frequency of the ferrite and by spin-wave buildup times, and is not related to the output frequency of the device. However, in the vicinity of the crossover point where energy transfer takes place, efficient transfer requires heavy coupling between the ferrite and the slot resonator as we have seen from Fig. 13, and it also requires over-coupling between the slot mode and the output waveguide.

We can write

$$E_{out} = F_{12}F_{23}E_{UM} \quad , \tag{3}$$

where E_{out} is the energy in the rf output pulse, E_{UM} is the energy associated with the uniform mode, F_{12} is the energy transfer efficiency between circuits 1 and 2 in the sense of Fig. 13, and F_{23} is the energy transfer efficiency between the slot resonator and the waveguide, for which we have

$$F_{23} = 1 - Q_2/Q_2' \quad , \tag{4}$$

where Q_2' and Q_2 are the unloaded and loaded Q's of the slot resonator.

In cold testing of the rf output circuit, a test signal from a swept-frequency signal generator is fed into the waveguide at the output flange. This signal flows back toward the ferrite, opposite to the normal direction of power flow when the device is operating as a generator. Reflections from the ferrite coupling circuit are used to analyze the behavior of these components. Reflection coefficient as a function of frequency is displayed on an oscilloscope. On this display, dips in the reflection coefficient are seen at frequencies corresponding to the resonant frequencies of the ferrite and the slot resonator. In these measurements the output circuit is located in a variable laboratory dc magnet, oriented such that the applied field lies along the pulsed coil axis, so that the resonant frequency of the ferrite can be tuned manually through the slot mode resonance. Also seen on the oscilloscope are absorption dips due to any other coupled resonances in the system. This includes resonances associated with the adjustable short and also miscellaneous spurious coupled resonances. The latter are, for the most part, weakly coupled modes. Some of these are associated with the dielectric spacers used to insulate the waveguide flanges as indicated in Fig. 24. It is found that these can be satisfactorily minimized by proper dimensioning of the parts, which is done empirically,

together with loading of these modes by resistance cloth as in Fig. 24. Absorption dips corresponding to the waveguide tuner were observed when that tuner was present.

The general behavior of the resonant modes is as follows. Assume that a relatively low value of dc magnetic field is initially applied to the ferrite. No pulsed fields are applied to the ferrite during these measurements, as the ferrite operates simply as a passive resonator for these cold test measurements. The ferrite absorption dip will appear as a very narrow resonance line whose width corresponds to the high unloaded Q of the YIG sphere. By contrast, the absorption dip for slot is much broader, under conditions of proper adjustment, corresponding to the much lower loaded Q of the slot mode, as loaded by the coupled output waveguide. As the dc magnetic field is increased, when the ferrite absorption line moves close to the slot resonance, the familiar "billiard-ball" effect of overcoupled circuits is observed, when the adjustments are such that the ferrite and slot modes are mutually overcoupled. In this process, the ferrite mode reaches a position of closest approach to the slot mode, and then becomes essentially stationary as the dc magnetic field is further increased. In this process, the ferrite resonance curve also broadens until the ferrite and slot mode curves are of essentially equal width. Of course, in this crossover range the two modes seen on the scope lose their original identifications with the individual ferrite and slot resonators. They are simply the two modes of the system of two coupled resonators, and as such, each of these modes has energy in each of the resonators. Upon further increase in the applied dc magnetic field, the higher-frequency mode of the pair, which was originally stationary and identified with the slot resonator, begins to move upward in frequency. It eventually narrows to the characteristic width of the unloaded YIG sphere, and takes on all of the characteristics of an independent, unloaded ferrite resonance.

The minimum frequency separation between the two resonance curves as a function of their tuning represents the frequency difference in Eq. (2), and thus determines the coupling coefficient K . Measurements on the slot resonance determine its unloaded Q , and also determine its loaded Q versus adjustments of the waveguide tuner.

- 43 -

Measured values of Q_2' and minimum usable Q_2 for the circuit of Fig. 24 are 300 and 50, respectively, so that Eq. (4) gives $F_{27} \approx 0.83$. The measured value of the ferrite coupling factor is $\kappa \approx 0.006$, so that from Fig. 13 we have $F_{12} \approx 0.43$.

V. DESCRIPTION OF II-B FERRITE GENERATOR

Scale drawings of the Model II-B x-band generator are shown in
Figs. 22, 23, and 24. Figure 22 shows plan and elevation views of the
overall device. It will be seen that all components are contained
within an electrostatic shielding enclosure, which consists of a length
of L-band rectangular brass waveguide, closed at both ends by brass
plates. A coax cable carrying the dc voltage for charging of the pulse
line enters at the right-hand end of this shielding enclosure.

Nitrogen pressure chambers are included for both the primary and
sharpening gaps in this system.

Figure 24 is a sketch of the x-band rf output circuit of the gen-
erator. The pulsed-field-coil is mounted in an rf circuit flange in
the manner which has been described above. This flange is insulated
from the adjoining waveguides by means of lucite plates which are shown
in the figure. These plates have been shaped to fit around the pulsed-
field-coil leads as indicated, to avoid minor sparking which otherwise
occurs in these areas.

It will be seen in Figs. 22, 23, and 24 that controls are brought
out of the shielding enclosure for operation of the rutile disk tuner
which adjusts the frequency of the slot resonator, and also for adjust-
ing the two tuning screws which are used to compensate for the suscep-
tance of the pulsed field coil in the waveguide. The waveguide on one
side of the rf circuit flange is terminated in a movable shorting
plunger, whose position is controlled from outside the shielding en-
closure.

The ferrite sphere, which is centered in the pulsed-field-coil,
is located on the end of an insulating rod which extends out through
the side wall of the output x-band waveguide and through the side wall
of the shielding enclosure, so that the position and orientation of the
ferrite within the coil can be controlled by a micrometer mechanism.

Figure 22 indicates that a small permanent magnet is located within
the shielding enclosure for providing the dc bias field for the ferrite.

FIG. 22--Assembly views of II-B generator.

- 46 -
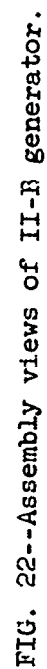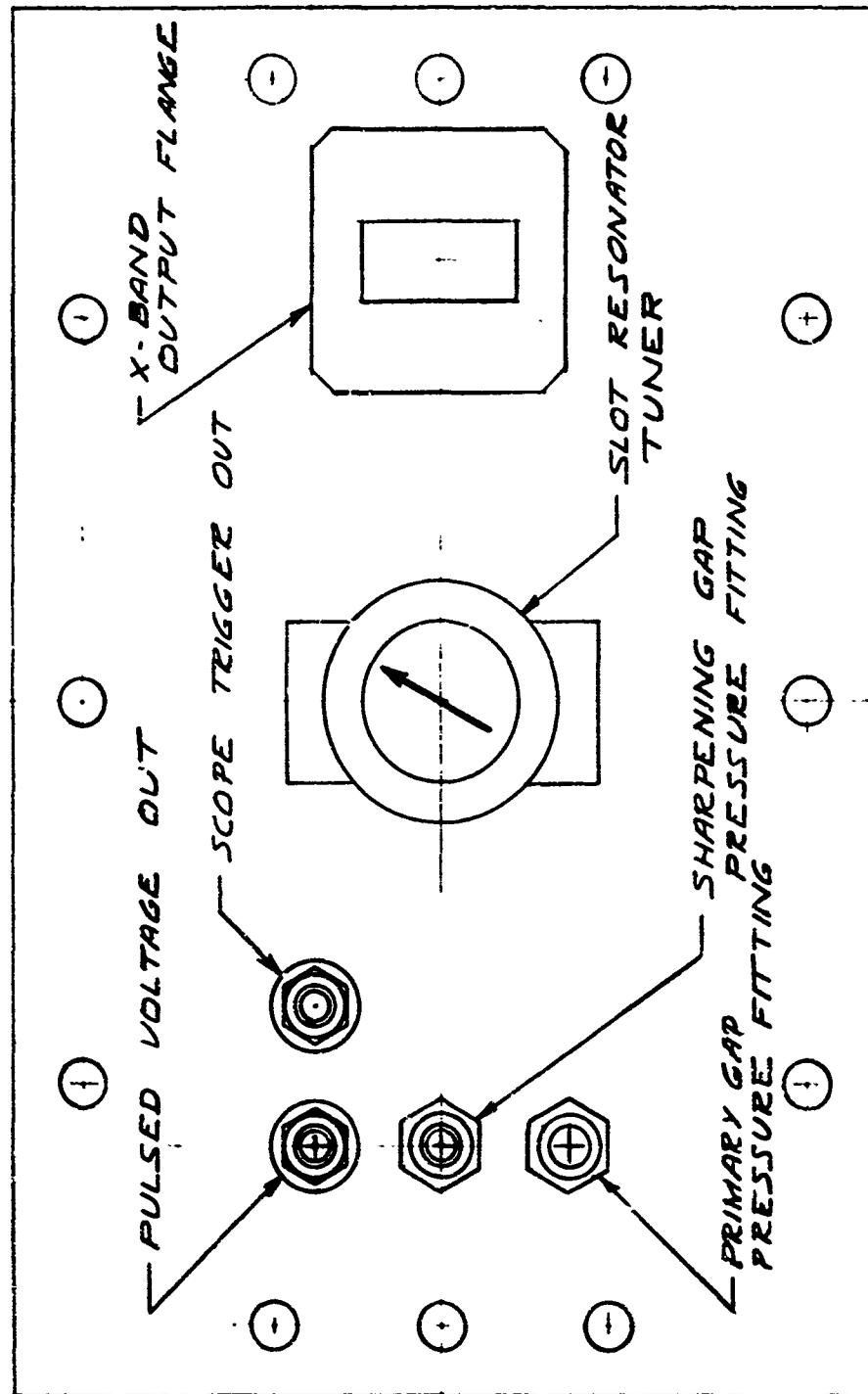
FRONT PANEL LAYOUT

SCALE IN INCHES

FIG. 23--Front panel layout.

FIG. 24(a)

EXPLODED VIEW OF
X-BAND WAVEGUIDE
COUPLING STRUCTURE

SCALE IN INCHES

#8-32
NYLON
SCREWS

RF CHOKE

HEAD CLEARANCE HOLE
TWO PLACES

LUCITE INSULATOR

PULSE LINE AXIS

ATTACH PULSE LINE

PULSED FIELD COIL
AND SLOT RESONATOR

RUTILE DISC

POLYSTYRENE POST

SLOT RESONATOR
TUNING SCREW

IRIS TUNING
SCREWS-BRASS

PULSE LINE

VERTICAL AXIS

PULSE
LINE
AXIS

ATTACH PULSE LINES

X-BAND
RESONANT
SLOT

SCALE IN INCHES

NOTE: ROTATED 90° ABOUT
VERTICAL AXIS
FOR CLARITY
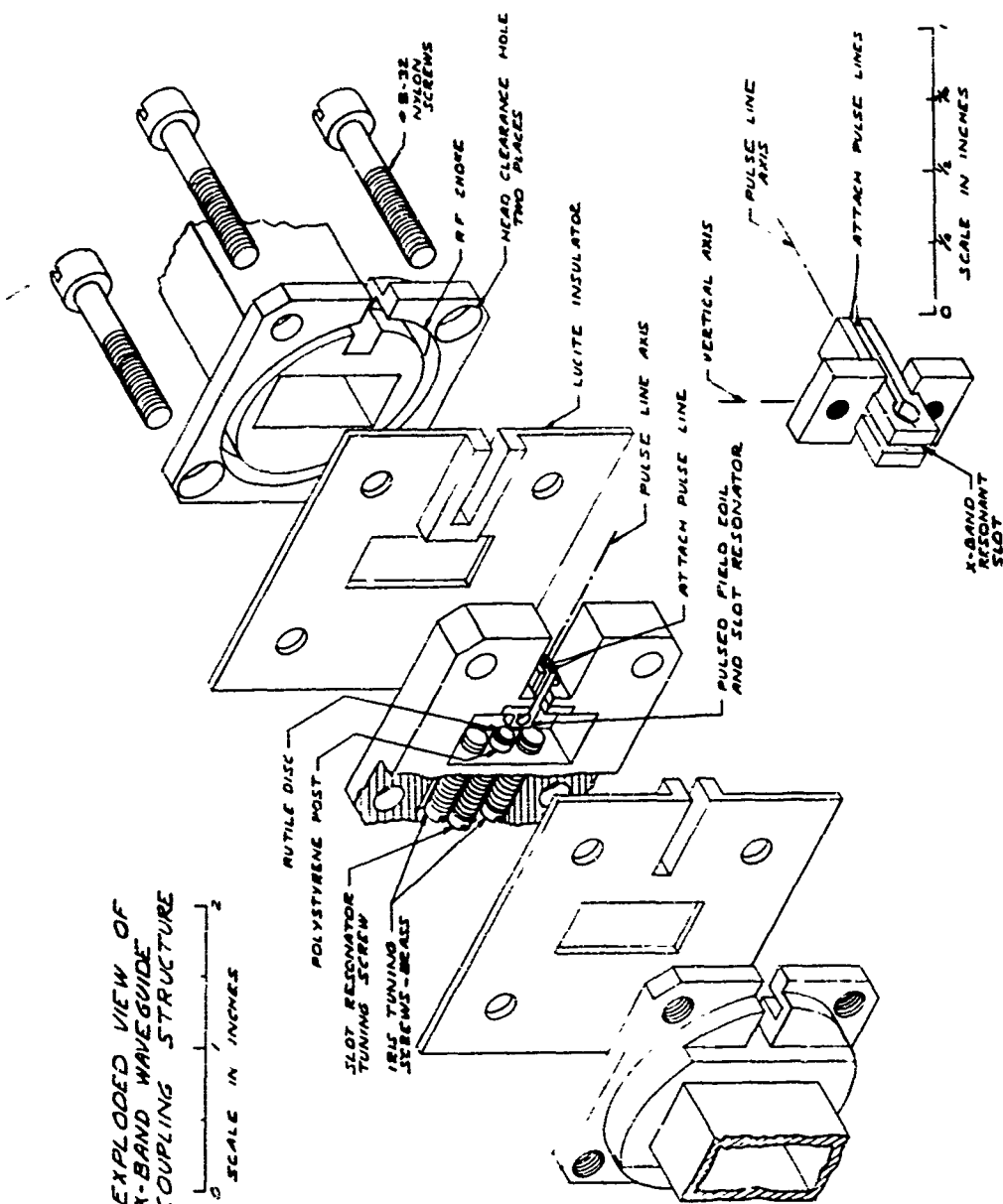
PULSED FIELD COIL AND
SLOT RESONATOR DETAIL

FIG. 24(b)

- 48 -

This is a yoke-type magnet, with a yoke fabricated from cold-rolled steel, and energized with ferrite circular-ring permanent magnets. This magnet assembly is capable of producing a field of 800 Oe at the ferrite, which is readily shunted down to the optimum operating value. This internal magnet is convenient when the generator is being operated routinely. For experimental measurements, to facilitate making rapid adjustments of the dc bias field, this magnet was not used, and a larger yoke-type magnet, whose pole pieces were capable of fitting over the outside of the shielding enclosure, was used. This was also a permanent magnet, having a mechanically adjustable shunt which allowed variation of the bias field level.

It will be seen in Fig. 22 that a pick-up loop for monitoring the pulsed field wave shape is available. This loop is encapsulated in polystyrene at the end of a small-diameter rigid coax line which is inserted into the device through an opening in the shielding enclosure, and also through an opening in the waveguide shorting plunger, so that the loop can be positioned arbitrarily close to the pulsed-field coil. A port is available for inserting a gauss-meter probe for measuring the dc bias field applied to the ferrite. Also in Fig. 22 can be seen two coax lines which attach to coax fittings on the front panel. One of these carries a trigger signal which is picked up by a loop coupled to the output strip line in the vicinity of the sharpening gap. The other is connected to a direct tap on the output strip line midway between the sharpening gap and the pulsed-field-coil, which is used to measure the amplitude of the pulsed voltage wave traveling on the output strip line. Since this latter voltage is of the order of 10 kV in peak amplitude, a high-voltage short-pulse fitting is required for the panel connection.

A photograph of the generator, removed from its shielding enclosure, is shown in Fig. 25.

It was not the purpose of the present work to study engineering problems connected with erosion and lifetime of spark-gap electrodes, corona or discharges associated with high voltage strip line conductors, or aging and breakdown phenomena associated with strip line dielectrics. The central purpose was to determine the maximum rf energy which can be
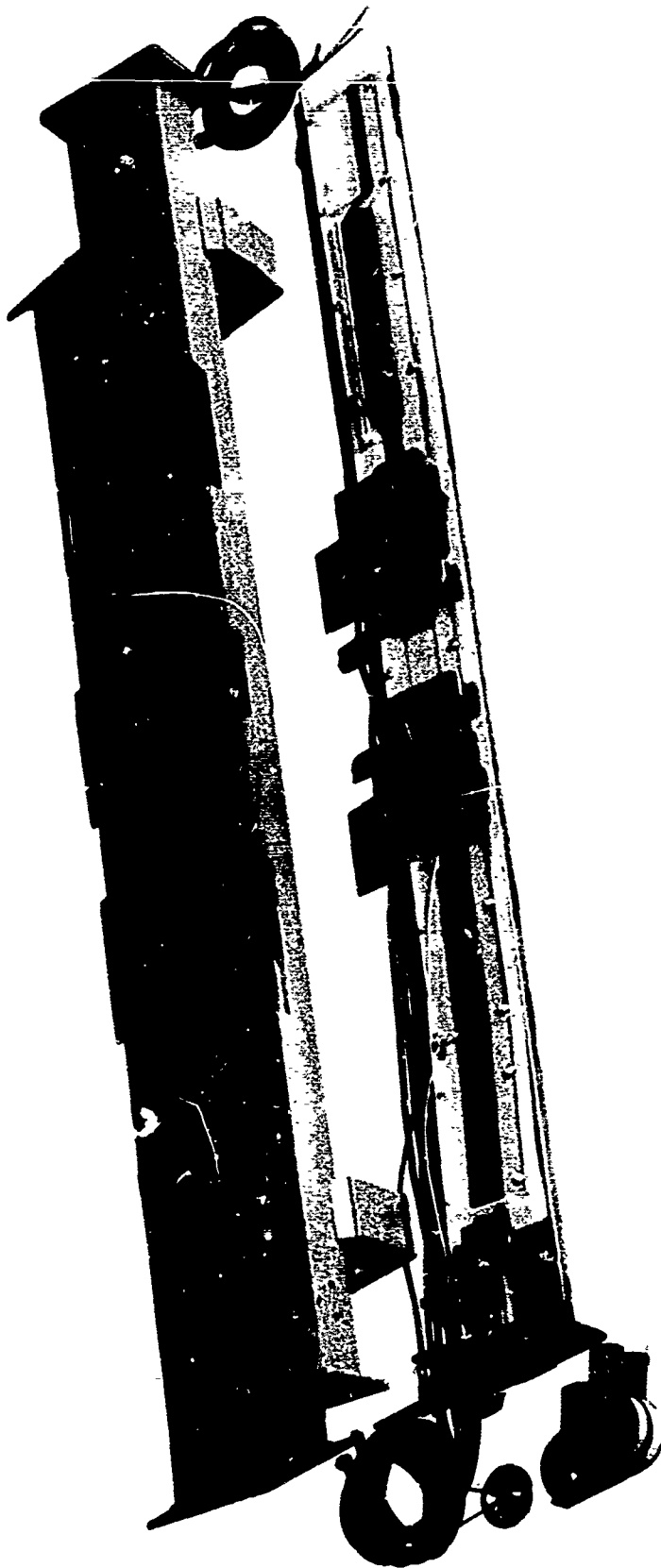
FIG. 25--Photograph of Model II-B generator removed from shielding enclosure.

extracted from a pulsed ferrite sample when a field pulse of suitable waveshape is applied. However, because of the large number of parameters involved, and the large number of measurements necessary in order to interpret the behavior of the device, measurements over a considerable period of time were involved. However, high voltage breakdowns were infrequent. The down time involved in the occurrence of such breakdowns was minimized by using a mechanical design in the pulser system which allows quick replacement of all components by means of spare parts which are kept on hand. Pulse-line dielectric sheets are fabricated from standard mylar strips which are easily pre-cut to the proper dimensions, with proper locations of holes and other cutouts, using a master template which was machined for the purpose. The assembly procedure is such that these new strips, as well as new spark-gap electrodes and pulse-line electrodes if required, can be easily dropped into place and the entire apparatus reassembled and placed back in operation within an hour's time, which in an experimental laboratory model of the present kind is entirely satisfactory. This avoided any necessity of spending time on the investigation of high voltage lifetime questions in order to gather rf operating data on the device.

Figure 26 shows a block diagram of the measuring circuits which
were set up for determining the rf and video pulse characteristics of
the Model II-B generator. Power in the rf output pulse is determined
by two methods. In one of these methods, average rf power output is
determined using a standard thermistor and power bridge, as indicated
in Fig. 26. As described in Section III, the average pulse repetition
frequency was accurately known by synchronizing the average firing rate
of the pulser with a signal of known frequency, so that average power
readings obtained from the thermistor bridge could be accurately con-
verted to rf energy per pulse. In the second approach to measuring rf
power output, the rf pulse height is compared directly with the scope
deflection produced by a signal from a reference generator, which is
indicated in Fig. 26. The power output of the reference generator is
measured directly on a power bridge. The crystal detector used for this
purpose is a Hewlett-Packard Model 424A fast-rise type, which has an
observed risetime of approximately 1.2 nsec. Precision attenuators were
used to adjust the output power of the ferrite generator to match the
output power of the reference generator in making peak power measure-
ments. In practice, the crystal detector sensitivity remains constant
for long periods of time, and it is possible to calibrate it and use
this calibration with only occasional rechecking. Note that the pro-
cedure of comparing power levels by means of attenuator adjustments
avoids any dependency of the power measurement on crystal power-law
characteristics.

Actually, the second method of power measurement, by comparison with
the reference signal generator, was used in the earlier measurements on
the generator. It was in subsequent measurements, when the power output
had been increased to higher ranges, that it became practical to employ
the thermistor bridge for power measurements. When this was done, a
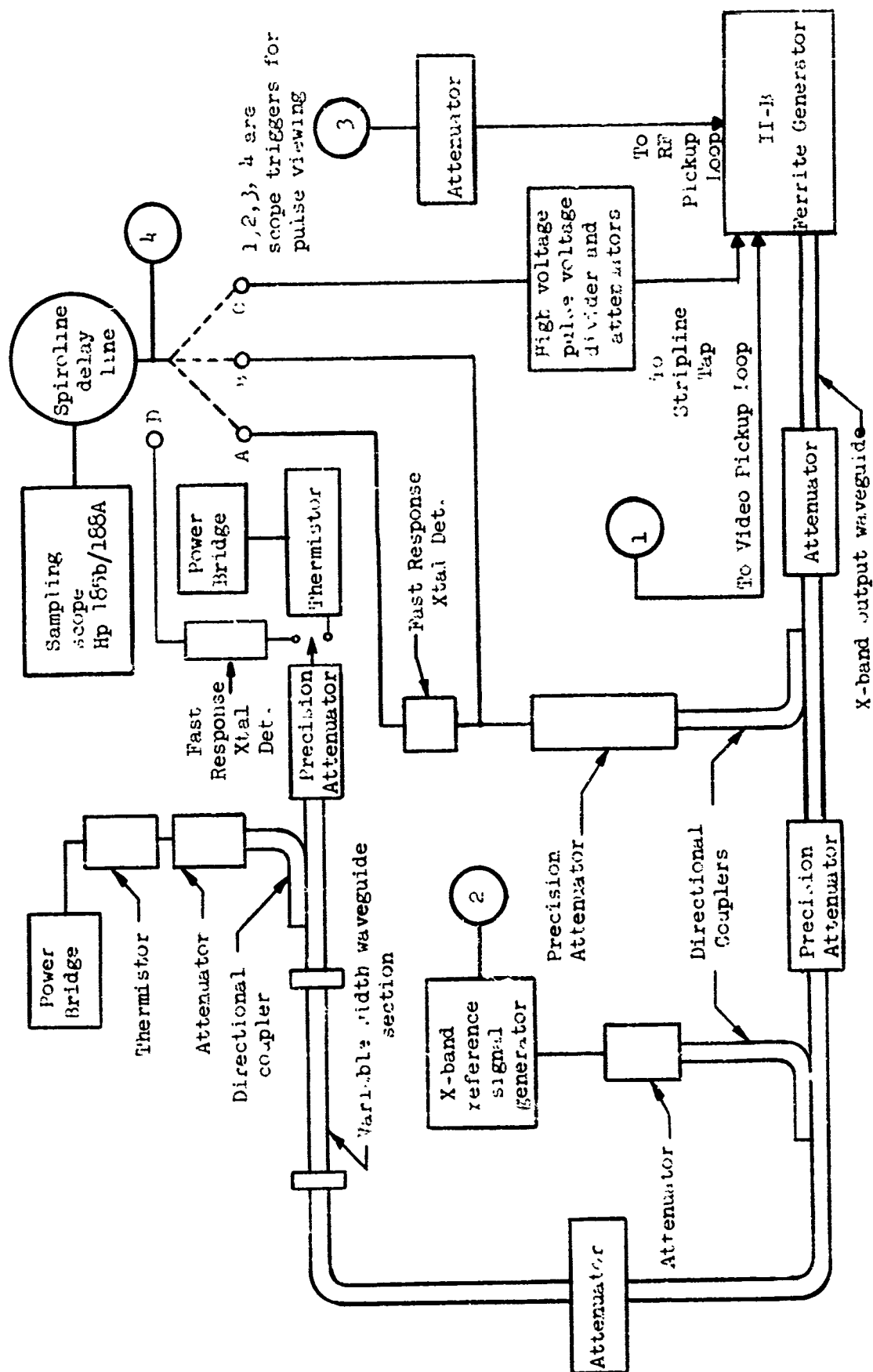disagreement by a factor of approximately 2 was found to exist between

FIG. 26.-Measurement circuit for Model II-B generator.

1,2,3,4 are scope triggers for pulse viewing

- 53 -

the two methods, with the thermistor bridge giving the lower readings. With the exception of Fig. 31 which is shown later, and whose purpose is to show the dependence of relative power output upon various parameter adjustments, all rf power figures quoted or used in calculations in this report are based upon the values obtained from thermistor bridge measurements.

Figure 26 also indicates provisions for measuring video pulse characteristics during the operation of the generator, by connecting the sampling scope to appropriate terminals of the generator which are shown in Figs. 22 and 23.

A photograph of the measurement setup for hot testing of the generator is shown in Fig. 27. The Model II-B generator may be seen on the table in the foreground. The earlier Model II-A device is in the large rectangular shield box in the left background. The two large coils of cable are the spiroline delay lines of Fig. 26, the larger being used for video pulse delay and the smaller for rf pulse delay.

In operation of the generator, the frequency of the rf output signal is controlled primarily by the slot-mode tuner, but it is necessary to also track the movable short in the output waveguide. Under these conditions, the output rf pulse train consists of single, nearly monochromatic pulses, whose frequency is tunable over the entire tuning range of the slot-mode tuner. In carrying out this procedure the proper position for the sliding short is a linear function of frequency and is readily preset. The primary tuning control is then adjusted for maximum average power as read on the average output power meter, and the rf waveform is observed on the sampling scope, while the primary tuner is readjusted slightly for the best rf envelope shape.

Figure 28(a) shows a sampling scope trace of the rf output pulse under proper adjustments. In viewing x-band waveforms care is necessary to eliminate junction reflections and higher mode excitation in the delay line circuit to the scope to obtain results as in Fig. 28. Circuits previously suitable for nanosecond video pulse viewing produced excessive echoes when used with x-band signals. The slightly increasing rf amplitude to the far right in Fig. 28(a), after the main pulse has ceased, is
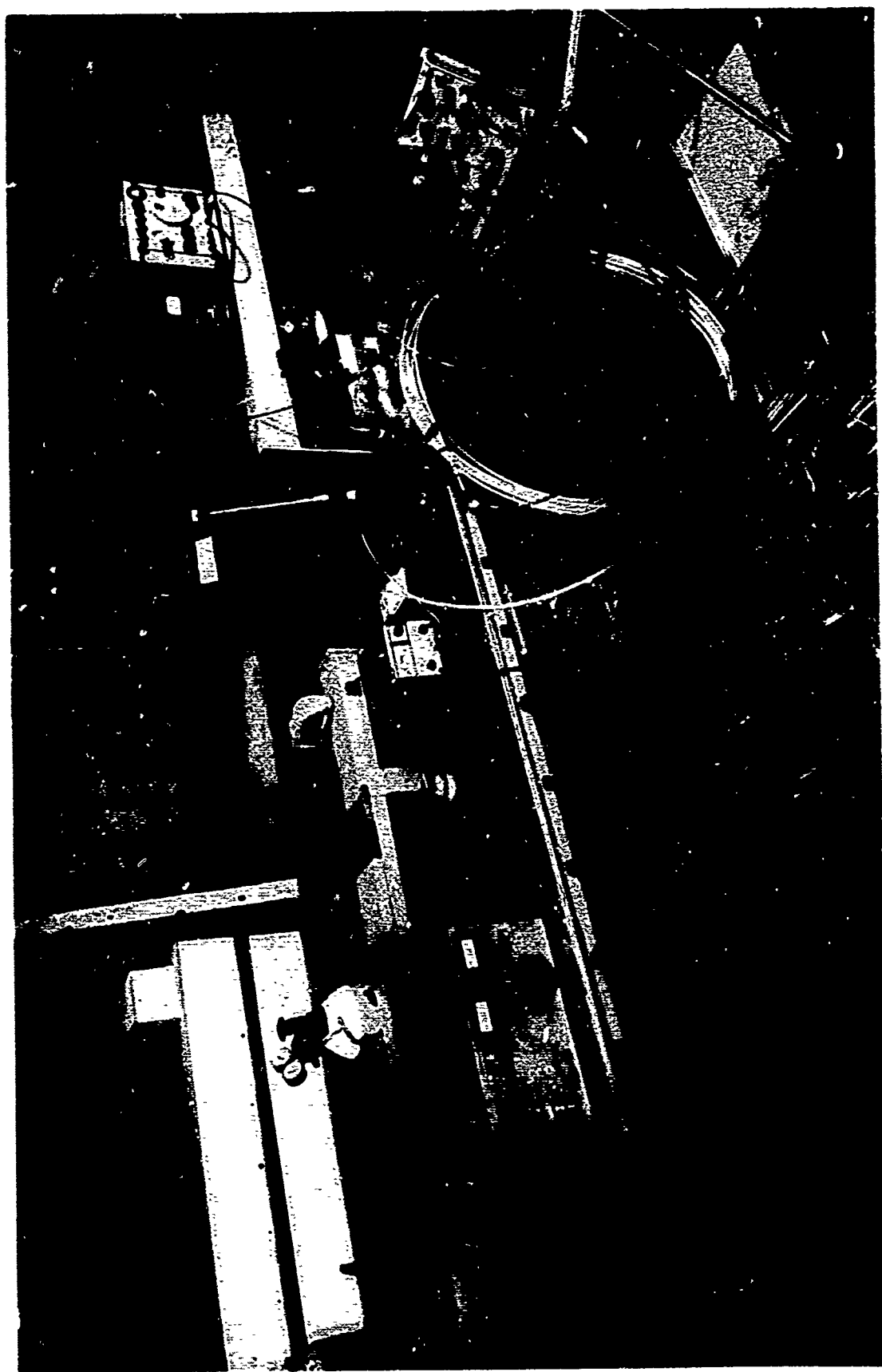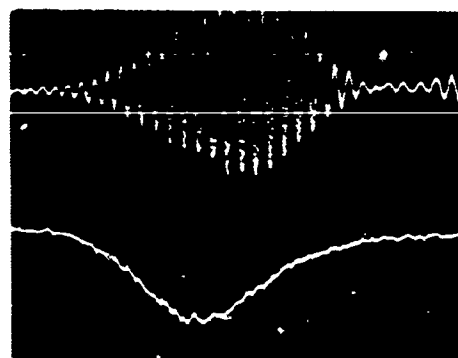
- 54 -

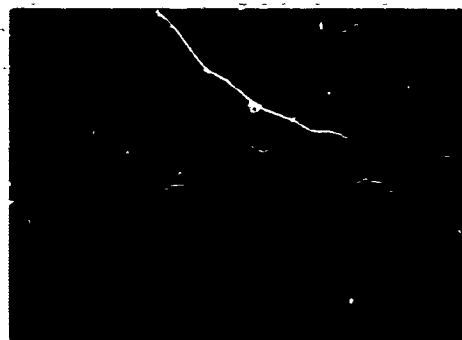FIG. 27.--Measurement setup for Model II-B generator.

rf WAVEFORM

DETECTED
WAVEFORM

400 PS/DIV

FREQUENCY 8 GC/S

FIG. 28(a)--Output pulses of Model II-B generator.

33 PS/DIV

EXPANDED rf WAVEFORMS

FIG. 28(b)--Expanded rf waveforms.

the beginning of an echo due to residual reflections at the scope input circuit after all other sources of reflection have been minimized.

In obtaining direct rf waveforms as in the upper trace of the figure, the output of the ferrite generator is sufficient to operate the sampling scope in this manner with some 70 dB of rf attenuation present in the rf transmission system between the generator and the Hewlett-Packard 188A sampling oscilloscope. In this operation the oscilloscope is triggered from a signal derived from a small pick-up loop coupled to the pulsed field. Figure 28(b) is an expanded view of the rf waveform of Fig. 28(a), which illustrates well the interpulse phase coherence. The smooth traces obtained in this way indicate a high degree of rf phase coherence from pulse to pulse in the output of the generator.

Also shown in Fig. 28(a), in the lower trace, is the rf output envelope obtained using a Hewlett-Packard Model 424A crystal detector working into 50 ohms. The crystal detector introduces distortions in the details of the output pulse, which are absent when the unrectified rf pulse is measured directly.

Tunability of the center frequency of the rf output pulse is illustrated in Fig. 29. The total tuning range observed is the same as the tuning range of the slot resonator mode. The rf energy per pulse is seen to generally increase as frequency increases, which is to be expected since the energy associated with the uniform precession mode in the present pulsing system is proportional to frequency of the mode, as has been seen above. During the measurements in Fig. 29, the pulsed field parameters were not adjusted for maximum rf energy per pulse.

Instantaneous frequency across the pulse can be determined from sampling scope pictures in the manner illustrated in Fig. 30. In this case the successive peaks in a sampling scope trace are numbered consecutively. The horizontal locations of the various peaks are determined using a traveling microscope, and these locations are plotted as a function of the peak number. If the instantaneous frequency, as averaged over half cycle intervals, were constant, the points so obtained would of course lie on a straight line whose slope would be a measure of this frequency. This procedure allows one to determine the instantaneous frequency at any
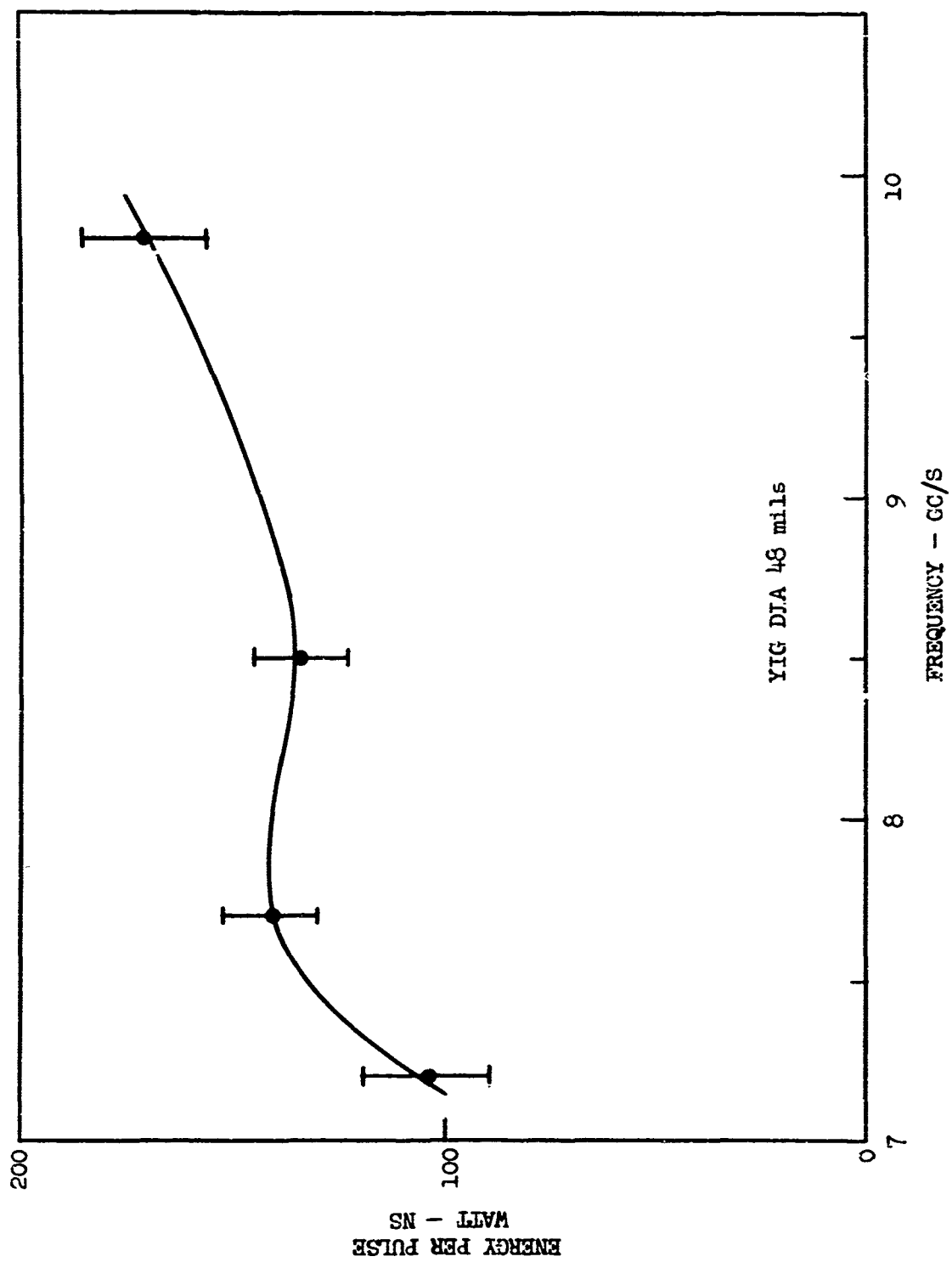
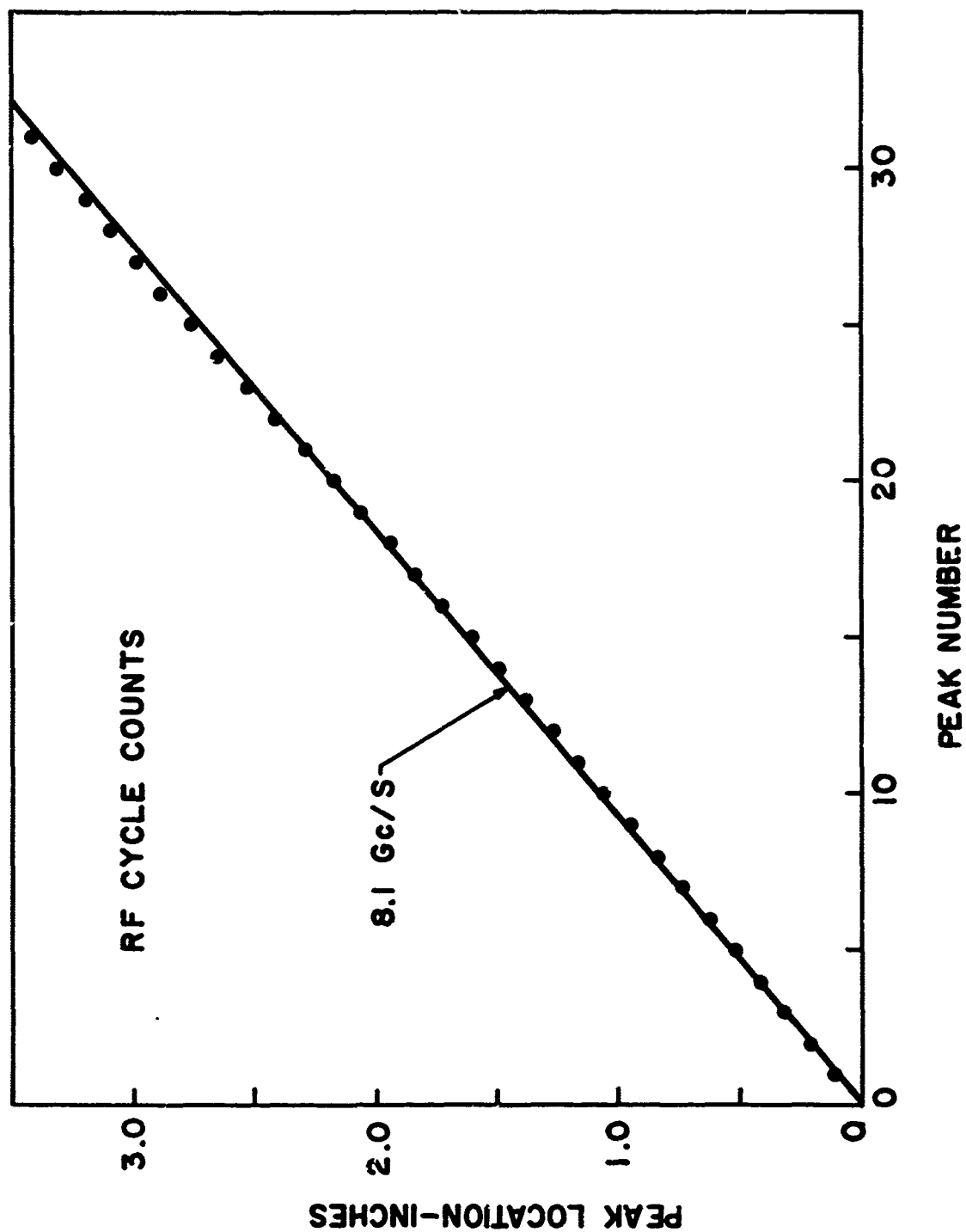FIG. 29.--Variation of rf energy with frequency.

FIG. 30--RF cycle counts.

point, as averaged over half cycle intervals. We see from Fig. 30 that the experimental points lie very nearly on a straight line, indicating only small deviations, across the pulse, from the average frequency for the entire wave train, the latter frequency being 8.1 Gc/sec in this particular case.

Because of the large number of variable parameters in this experimental model of the device, it was impracticable to attempt a straightforward optimization by running systematically through all possible combinations of these parameters in order to determine maximum rf power output. Instead, various adjustments were set up intuitively and were then varied in steps which, for the most part, tended to increase the power, and for each new result the parameter adjustments were recorded and the power output was plotted on a scatter graph which is shown in Fig. 31. In this figure the rf energy in the output pulse, measured in watt-nanoseconds, is plotted on the vertical scale, as a function of diameter of the YIG sample on the horizontal scale. The plotted points represent measured values of rf output energy. The solid lines on the graph represent the theoretical energy available from the uniform precession mode in a YIG sphere for several fixed values of precession angle, assuming that the process of extracting rf energy from the ferrite is 100% efficient. If a measured energy value lies on a straight line for a given value of precession angle, this indicates that the actual maximum precession angle achieved in the ferrite must exceed this value, because there will of necessity be some energy lost in the process of transferring energy from the ferrite to the rf circuit. This question is discussed further below. We notice from Fig. 31 that the maximum energy, in the present series of experiments, was obtained for YIG spheres of 46 and 48 mils diameter. We see that for these particular cases the maximum indicated energy per pulse in Fig. 31 is 660 watt-nanoseconds. For the measurements involved in this particular graph, rf power levels were determined by comparison with the power output of a standard laboratory signal generator used as a reference. As stated above, this procedure produces results which are not in agreement with power measurements obtained using a thermistor bridge. Thus, the plotted points in

- 60 -
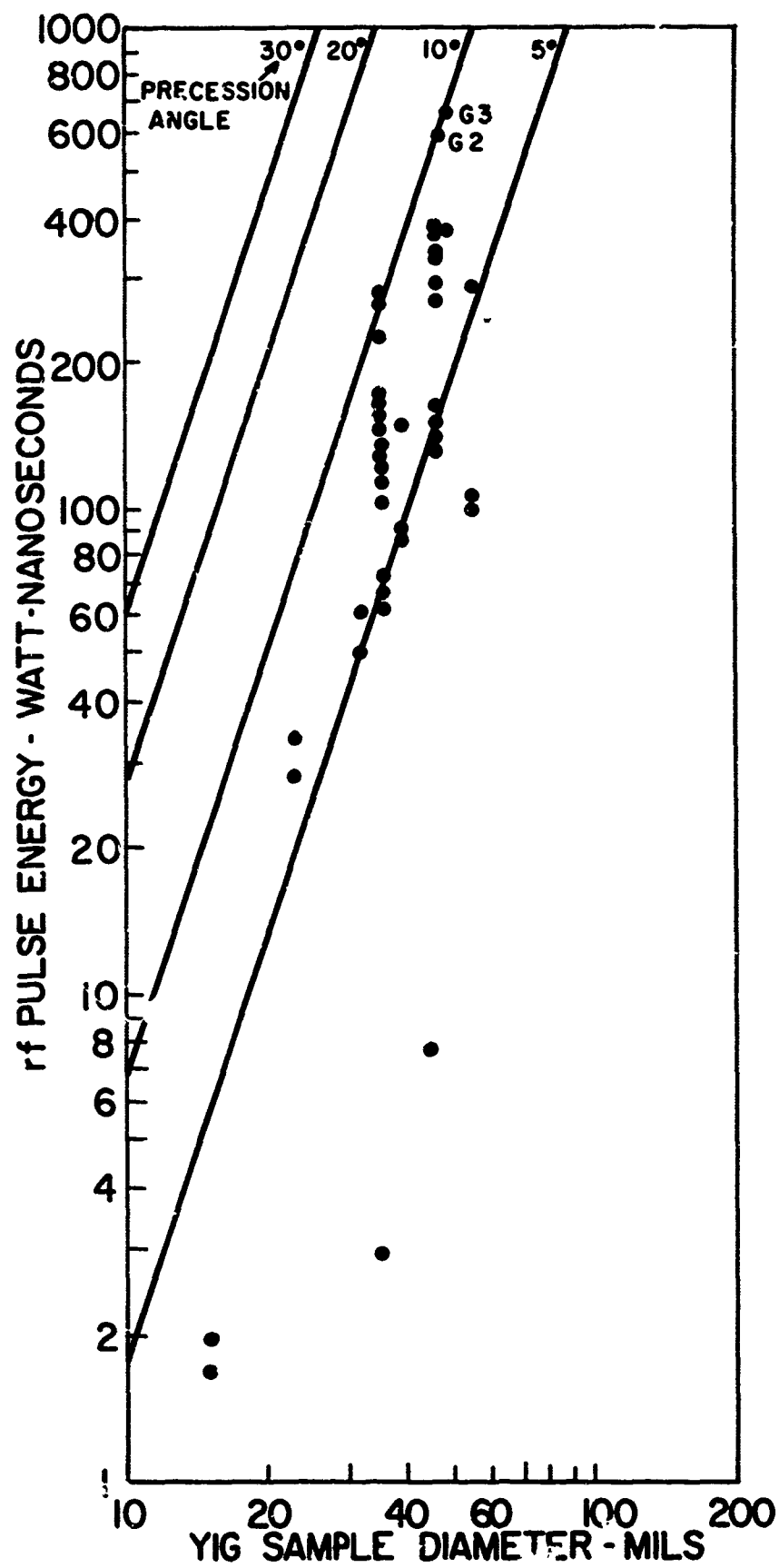
FIG. 31--Dependence of relative rf pulse energy on YIG sample diameter.

- 61 -

Fig. 31 are to be used for the purpose of illustrating relative power output variations as a function of parameter changes. The straight-line plots however, being theoretical, are quantitative.

The highest value of rf output energy which has been observed is 325 watt-nsec, determined by thermistor-bridge measurement of average power as discussed above. Using the values of F_{12} and F_{23} from Section IV, Eq. (3) gives, for the theoretical ratio of output energy to the energy available from the ferrite, $E_{out}/E_{UM} \approx 0.34$. We thus infer from rf output and cold test measurements that the maximum energy actually associated with the uniform mode in the ferrite was ≈ 1 kW-nsec. Referring to the straight lines in Fig. 31, this energy corresponds to a precession angle of approximately 13°. This is seen to be in favorable agreement with the precession angle predicted theoretically from the computer calculations of build-up kinematics, as shown earlier in connection with Fig. 21.

VII.   MODIFICATIONS

A.   RF Output Circuit Modifications

In the exploratory cold test work on the circuit of Fig. 24, the
adjustable waveguide short was important because it provided a simple
method of experimentally varying the coupling between the slot mode and
the waveguide fields while measurements were being made. The adjustable
coupling was similarly important during the first hot test measurements
when the circuit of Fig. 24 was incorporated in the Model II-B generator.

This was a carryover from an investigation of an earlier circuit
which preceded the slot resonator design. The former involved the use
of a miniature rutile dielectric resonator to provide the coupling be-
tween the YIG sphere and the waveguide field. In the case of dielectric
resonators of this kind, an adjustable short has become a standard means
of varying the coupling between the resonator and a waveguide. The
dielectric resonator was found capable of providing suitable values of
internal Q and external Q , but was not as compatible with the re-
quirements of the pulse field coil as is the slot resonator.

A considerable amount of cold test and hot test experience with the
circuit of Fig. 24 showed that the adjustable short has various dis-
advantages which made it desirable to redesign the output coupling cir-
cuit such as to eliminate the need for this component in a practical
generator. One disadvantage has been seen in Section VI in the fact
that in tuning the output frequency of the generator, it is necessary to
properly track the waveguide short. The variable short constitutes an
additional resonant circuit coupled to the rf output system. This
results from the fact that the pulsed-field-coil structure constitutes
an rf susceptance in the waveguide which, taken together with the mov-
able short, forms an x-band resonator. This, together with the YIG and
slot resonators makes, in all, a circuit of three coupled resonators,
all of which are tunable. This system is difficult to adjust for the
proper Q values for the two main resonators. Another disadvantage of

- 63 -

the movable waveguide short is that it requires a considerable amount
of space compared to the size of the other essential portions of the
output circuit.

Some work has been carried out on an output circuit design which
e iminates the need for the variable short. The arrangement is indi-
cated in Figs. 32 and 33. The pulsed-coil/slot-resonator element has
been moved from its original position in the broad side-wall of the
waveguide (Fig. 24) to a new position in the center of the waveguide
shorting plane. The fixed shorting plane in Fig. 32 replaces the mov-
able plunger of the earlier design. It will be seen that the shorting
plane is fabricated in two halves, which are separated and insulated
from the mating output waveguide flange, to avoid short-circuiting the
pulsed current fed to the coil. The leads to the pulsed coil are
directly connected electrically to the opposite halves of the shorting
plate. Just as in the previous design, this symmetrical arrangement
completely avoids radiation of rf energy back into the strip-line
pulser circuit.

Consideration of the circuit orientations of Fig. 32 and of the
normal distribution of rf magnetic fields in the waveguide, indicates
that strong coupling can exist between the slot resonator and the wave-
guide fields. It is found that when the slot resonator is located as
in Fig. 33, the external Q of the slot mode is the same as quoted
earlier for the circuit of Fig. 24 over part of the tuning range. This
circuit was installed in the II-B generator as in Fig. 32 and operated
briefly. It showed approximately the same rf power output as the pre-
vious circuit, but with simpler tuning since there is only one tuning
adjustment. In further cold test work with this circuit, a slot
resonator element was arranged to slide in the shorting plate, with a
micrometer drive to vary the depth of penetration of the resonator into
the waveguide. The resonator element was guided by cutouts in the two
halves of the shorting plate, and these halves were spring-loaded against
the pulsed coil leads to make electrical contact with them during the
motion. It was found that the coupling between the waveguide and the
slot resonator decreased as the penetration was decreased, as expected.

- 64 -

Polystyrene Spacer

Conducting Sheet

Pick-up Loop Coax

Choke Flange

Tuner Shaft

Shaft Slot

Resonator

Ferrite-Holder Shaft

Spring-Loaded Tuner Drive

St'd X-band Waveguide

Drive Clutch

Front Panel of Fig. 22.

TOP VIEW

Strip Line Tabs

Split Shorting Plate

SIDE VIEW

Pulsed Field Coil

(*FULL SCALE*)

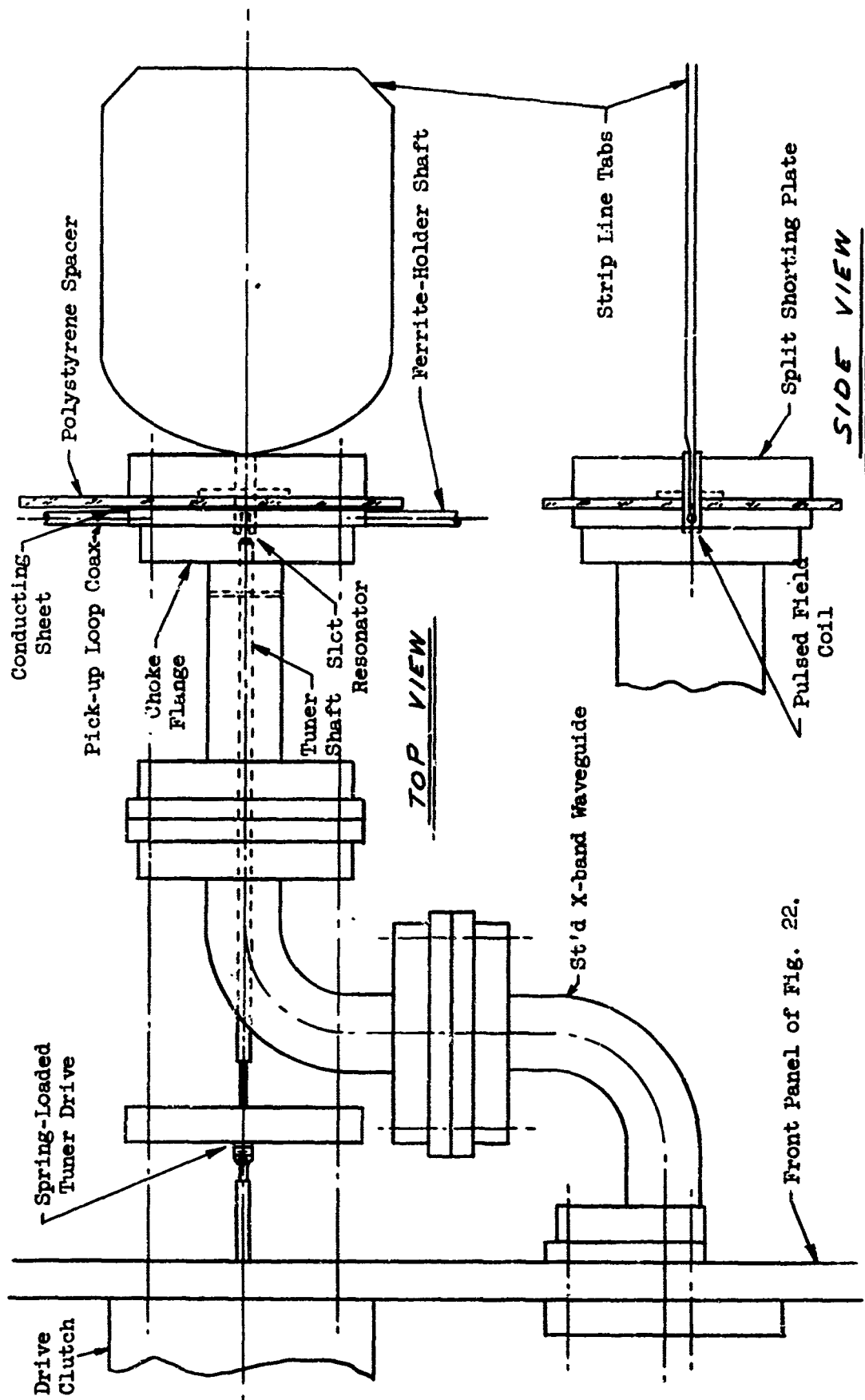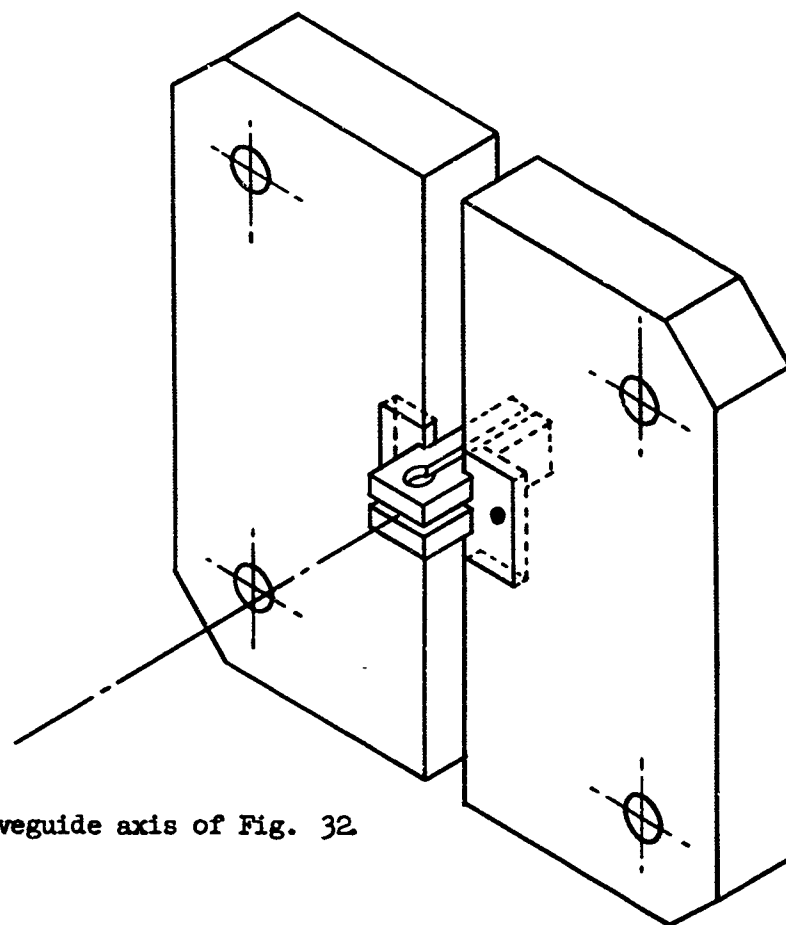FIG. 32.—Modified rf output circuit for II-B generator.

Waveguide axis of Fig. 32

FIG. 33--Detail of shorting plate of Fig. 32

It was also found that the addition of ridges in the waveguide could be
used to increase the coupling over that obtainable in unloaded guide.
These ridges were attached along the center lines of the two broad faces
of the waveguide, and started at the shorting end plate, so that the
waveguide in the vicinity of the slot resonator was a double-ridged
guide. The width of the ridges was 0.313 inches and the spacing between
opposing ridges was 0.170 inches. In going away from the slot circuit
these ridges were tapered out into standard waveguide. A typical set of
measurements of internal and external Q as a function of frequency for
the slot resonator with these ridges present is shown in Fig. 34. It is
seen that the external Q , Q_E , of the slot resonator dropped to low
values, as desired, but varies considerably with frequency. Beyond the
upper frequency range shown in the figure Q_E dropped below 20, to
values which were not directly measurable. These low values of Q_E are
of interest for high output circuit efficiency in the generator. Further
cold test work would be desirable, attempting to decrease the frequency
variation of Q_E . The objective would be to obtain a design having
Q_E which could be preset to any desired value, and which would remain
reasonably constant at this value over whatever frequency tuning range
is desired.

Note that the internal Q , Q_0 , of the slot resonator is approxi-
mately independent of frequency, as it should be. [Here, Q_0 corresponds
to Q_2' of Eq. (4).] However, its value is lower than for the case of
Fig. 24. This may be associated with details of the ridge construction
in the vicinity of the slot resonator; Eq. (4) shows that it would be
important to remove the source of loss to obtain maximum output circuit
efficiency.

A spurious resonance was found in the rutile tuning disk when tuning
to the low-frequency portion of the tuning range. A small block of sty-
cast dielectric, having dielectric constant of 12, was cut to fit directly
into the electric field region of the slot resonator. This provided a
fixed capacitor which lowered the frequency of the resonator and removed
this effect. However, the stycast contributed to the Q degradation,
so that one would want to either redesign the rutile tuner disk or replace
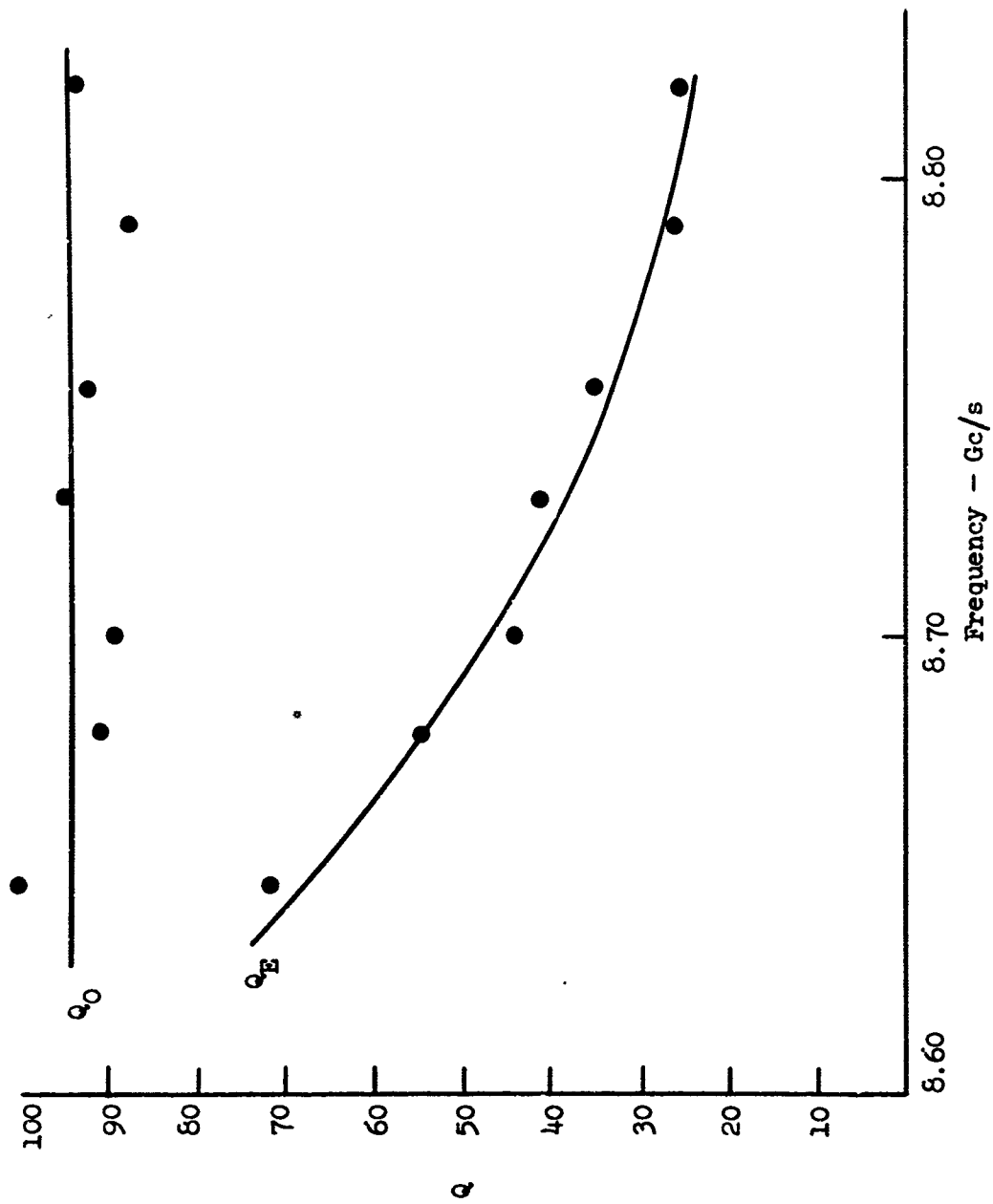the stycast sample with a dielectric of higher Q .

FIG. 34--Measured values of internal and external Q of slot resonator in modified circuit.

- 68 -

If these various modifications can be successfully carried out, the ridged output circuit may be capable of providing higher efficiency than the present output coupling system in the II-B generator, together with having the advantage of single-knob frequency tuning.

B. Proposed Modification of Pulsing Process

It is shown in Section III that the initial parabolic portion of the present pulsed field waveforms has, in theory, a very harmful effect on the precession angle. In fact, the present precession angle is seen to be near the bottom of the most steeply declining portion of the curve of Fig. 21, so that any reduction in the time required to reach the junction point would be of real value in increasing the precession angle. According to Fig. 21, the parabolic effect in the present generator reduces the precession angle by a factor of 2.5, which leads to a reduction of energy of 7.8 dB. It is to be expected that the output energy of the generator could be increased by this amount if the parabolic effect could be eliminated.

A new approach, aimed at overcoming the limitation of precession angle due to the prarabolic effect in the pulsed field, is illustrated by Fig. 35. Here the pulsed magnetic field $\dot{H}_p$ is applied at an angle to H_0 which exceeds 90°, i.e., the pulsing angle ψ_0 exceeds 90°. The vectors 1, 2 and 3 represent the total magnetic field at three successive instants of time during the pulsed field buildup. It is seen that the total field magnitude at first decreases monotonically with time until it reaches the value of vector 2, and thereafter increases monotonically with time. The parabolic range labeled in Fig. 35 covers the time interval required to reach the junction point. During this interval the precession frequency is relatively high and the sweep rate is low, so that very little precession angle is established. The interval between vectors 1 and 3, labeled excitation range, is the interval during which the precession frequency is lowest and the angular velocity of the total field vector is highest. This is the nonadiabatic region during which excitation of a large precession angle is expected to occur. The pumping range beyond vector 3 is the range during which the
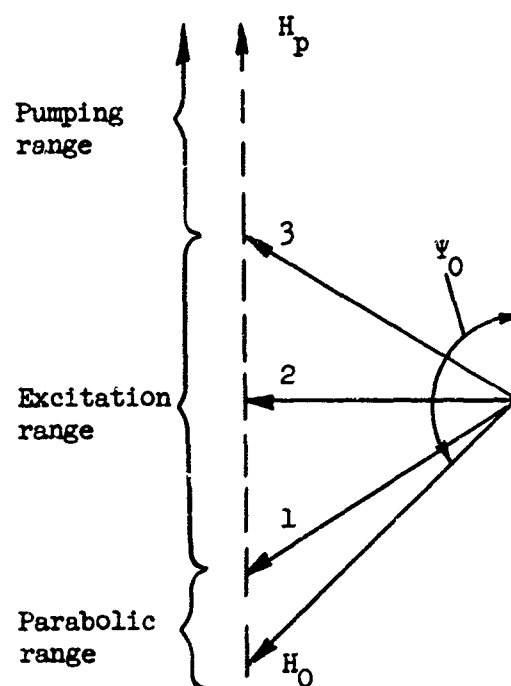
FIG. 35--Illustration of proposed process for increasing the final precession angle.

magnitude of the precession angle remains substantially constant while its frequency and energy are pumped upward by the pulsed field, just as in the present Type II generator.

The essential idea involved in this approach is that the parabolic region of the pulsed field rise, which involves a very low average rate of rise, is moved outside the critical region of low precession frequency. The low frequency region is then traversed with high angular velocity, a condition now known to be necessary for the establishment of large precession angle. We know that the entire precession angle is essentially established during the first one to two radians of precession in the region of lowest precession frequency. The behavior under the conditions proposed in Fig. 35 should be first studied on the digital computer, to determine the extent of improvement, and the optimum combination of parameters. This would represent an extension of computer cases solved previously for pulsing at angles of 90° and less. An experimental evaluation would involve simple mechanical modification of apparatus of the present type to permit pulsing at angles other than 90°, and to permit increased biased field amplitude.

This mode of operation has a further possible advantage which may be of importance. Theory and experiment both predict a rapid increase of energy with decrease in the magnitude of the dc bias field and the present approach, by pulsing rapidly through the region of minimum total field, instead of dwelling in that region for a long period of time (essentially continuously) as in the present operation, may allow the use of small minimum field before the formation of domains in the ferrite becomes harmful. That is, as the total field vector sweeps through the position 2 in Fig. 35, it may be possible for its magnitude to dip below the allowable field minimum required to maintain saturation in the case of a dc field. Due to the rapid sweep rate through this region, and to the reasonably small average angle between the total field and the magnitization in this region, this fact may be of importance in producing a second increase in the final precession angle and energy in the Type II device, over and above the increase due to elimination of the parabolic effect.

- 71 -

C. ·Other Possible Modifications

We list here a few additional topics which might be of value to explore for further development of Type II ferrite generators.

With regard to increasing the power output, one should consider possible use of multiple ferrite spheres, or larger-volume samples, to increase the energy associated with the uniform precession. Also of interest is the use of material of lower saturation magnetization, together with lower bias field to increase the uniform precession magnitude. Material with high crystalline anisotropy, such as single-crystal planar ferrite, which has been developed at the Signal Corps Engineering Laboratories in recent years, might be used to advantage to achieve larger precession angles, or to reach higher output frequencies with lower pulsed field magnitudes.

In terms of a practical device, great reduction of physical size should be possible. The active YIG sample and slot resonator circuit are extremely small. The bias field permanent magnet could be correspondingly small. In the pulser strip-line, segments which are presently employed for time-domain isolation of pulse reflections for measurement purposes, could be eliminated. Dimensions of the remainder of the pulser could be reduced very appreciably by rearranging strip-line layouts to equalize dimensions, employing recent techniques for miniature strip-line fabrication, and by miniaturizing the switching elements. It might be possible for the spark-gap switches, which have proved very satisfactory for the present laboratory experiments, to give way to other types of switches.

Regardless of the uniform precession amplitude which is developed in the device, the energy associated with the uniform precession mode in the ferrite sample is necessarily a small fraction of the pulse energy circulating in the strip-line circuitry. This circuitry has a reasonably high Q , and the Q could be further increased, and thus it is possible in principle to devise means for recirculating this unused energy back to the dc power supply after each pulse. This possibility was not investigated under the present program, as it was outside of the present objectives, but could be an important aspect of any practical development of devices of this kind.

REFERENCES

1. R. V. Pound, U. S. Patent No. 2,873,370.

2. B. J. Elliott, T. Schaug-Petterson, and H. J. Shaw, J. Appl. Phys. Suppl. $\underline{31}$, 400 (1960).

3. M. R. Stiglitz and F. R. Morganthaler, J. Appl. Phys. $\underline{31}$, 37 (1960).

4. A. P. Aleksandrov, V. I. Khonin, and E. G. Yaschen, JETP $\underline{38}$, 1334 (1960).

5. H. J. Shaw and B. J. Elliott, "Pulsed Magnetic Field Millimeter Wave Generator," Microwave Laboratory Report No. 856, Stanford University (September 1961); also, "Generation of Microwave Radiation with Ferrimagnetic Samples Subjected to Pulsed Magnetic Fields," Magnetic and Electric Resonance and Relaxation, Proc. of the XIth Colloque Ampere, Eindhoven, 2-7 July 1962 (North Holland Publishing Co., Amsterdam, Holland, 1963), p. 770.

6. H. Brunet, Compt. Rend. $\underline{252}$, 2860 (1961).

7. H. J. Shaw, B. J. Elliott, K. J. Harker, and A. Karp, J. Appl. Phys. $\underline{37}$, 1060 (March 1966).

8. Status Reports Numbers 1, 2, and 3 under contract DA 28-043-AMC-00397(E), Stanford University Microwave Laboratory Reports Numbers 1336, 1345, and 1360, respectively (1965).

9. K. J. Harker, Trans. IEEE, $\underline{MAG-2}$, 39 (March 1966).

10. H. Suhl, Proc. IRE $\underline{44}$, 1270 (1956).

11. E. Schlömann, "Ferromagnetic Resonance at High Power Levels," Raytheon Report No. R-28 (October 1, 1959), Research Div., Raytheon Company, Waltham 54, Mass.

12. E. Schlömann. J. Appl. Phys. $\underline{33}$, 2822 (1962).

13. K. J. Harker and H. J. Shaw, J. Appl. Phys. $\underline{37}$, 3035 (July 1966).

APPENDIX A

FINAL PRECESSION ANGLES FOR

PULSED FERRITE SAMPLES

Final Precession Angles for Pulsed Ferrite Samples

KENNETH J. HARKER, MEMBER, IEEE

Abstract—A theoretical study has been made of the transient motion of the magnetization vector in isotropic ferrite spheres during the application of pulsed magnetic fields at an angle to the dc saturating field. Results are presented which permit the determination of the final precession angle for 1) arbitrary pulse-rise rates and pulsing angles when the pulse is linear, and 2) arbitrary pulsing angles when the pulse is slowly rising and nonlinear.

INTRODUCTION

IT HAS BEEN SHOWN theoretically [1], [2] and experimentally [3], [4] that small ferrite samples subjected to pulsed magnetic fields can transfer energy from the pulsed magnetic field to a suitably coupled RF circuit in the form of microwave energy. The basic process involved is the establishment of an angle between the magnetization vector in the ferrite and the applied magnetic field vector by orienting the applied field at an angle to the magnetization, and by introducing the applied field in the form of a pulse whose rate of rise is sufficiently rapid that an appreciable fraction of this physical angle is maintained until the field has reached its desired magnitude. This is a question of the kinematics of electron spin motion in a pulsed magnetic field. As the magnetic field rises, torques are exerted upon the magnetization in the sample, resulting in a motion of the magnetization which generally tends to reduce the angle between the magnetization and the field during the build-up interval of the field. The RF energy which can be extracted from the ferrite increases monotonically with the magnitude of the final value of the angle between the magnetization and the applied field, this increase being quadratic for small angles. Because of the fundamental importance of the final precession angle, this paper will present a theory for predicting its magnitude in isotropic spherically shaped samples as a function of the angle to the magnetization at which the applied field pulse is oriented, the rate of rise of the applied field pulse, and the magnetic properties of the ferrite sample.

In practice, additional processes also operate to affect the final value of precession angle obtained. One such process is the amplification of spin waves from their thermal levels to high levels, which decrease the energy available from the desired uniform precession mode and increase the energy associated with spin modes which, unlike the uniform precession, cannot transfer their energy to a coupled microwave circuit. In steady state problems, spin wave phenomena of this kind have been widely studied [5], [6], [7] and are well known. Under the present

transient circumstances a new study of these mechanisms is required, and such a study has been carried out using the digital computer [8]. Another factor which, in principle, influences the final precession angle is the existence of dissipation mechanisms within the ferrite, which have been ignored in the analysis being reported in this paper. In practice, it can be expected that the effect of such dissipation during the rise time of the applied field will be very small, because the avoidance of serious spin wave effects typically limits the total rise time of the applied magnetic fields to values much shorter than the relaxation time of common YIG materials. Under these circumstances, any effects of attenuation within the ferrite would, in practice, occur during the interval devoted to extraction of RF energy from the ferrite, which process is not within the scope of this paper. Also, it should be recognized that in practice, of course, the amount of RF energy attainable from the ferrite will be strongly dependent upon the efficiency of the RF coupling system used to extract the RF energy, which again is not within the scope of this paper.

The question of spin-wave effects was noted, has been the subject of a separate theoretical investigation, and the other factors previously listed, which also combine to limit the final precession angle, are the subject of extensive experimental studies which are now in progress in this laboratory. In the meantime, the particular aspect which is studied theoretically in this paper has a basic relationship to these other aspects in that it shows the maximum possible precession angles which one can hope to attain on simple kinematic grounds, quite apart from the various experimental parameters which enter into the other effects mentioned above. While this present kinematic problem has received earlier theoretical study [1], the present paper presents the first solutions which are both precise and free of approximating assumptions, and which also extend to the range of large precession angles.

EQUATIONS OF MOTION

In the fixed coordinate system $(x'y'z')$ shown in Fig. 1, the sample is initially magnetized to saturation by a constant magnetic field, H_0, with components

$$H_{x'} = H_0 \sin \Psi_0 \tag{1}$$

$$H_{y'} = 0 \tag{2}$$

$$H_{z'} = H_0 \cos \Psi_0 \tag{3}$$

A pulsed field $H_p(t)$ is then applied along the z'-axis.

It is convenient to introduce the moving coordinate system (x,y,z), also shown in Fig. 1. The z-axis of this system is chosen to coincide with the total magnetic field

Fig. 1. Coordinate system.

Fig. 2. Variation of M_z with $\beta^{1/2}\tau \sin \psi_0$ for $\psi_0 = 30°$.

H(t), and the y-axis with the fixed system's y'-axis. The angle Ψ is defined in the figure, and Ψ_0 is chosen to be the value of Ψ at the initiation of the pulse.

The equations of motion in the moving coordinate system for the magnetization vector components M_x, M_y, and M_z are given by

$$\dot{M}_x = -\gamma M_y H - M_z \dot{\Psi} \tag{4}$$

$$\dot{M}_y = \gamma M_x H \tag{5}$$

$$\dot{M}_z = M_x \dot{\Psi}, \tag{6}$$

and

$$H^2 = (H_0 \sin \Psi_0)^2 + (H_0 \cos \Psi_0 + H_p)^2 \tag{7}$$

$$\cot \Psi = \frac{H_0 \cos \Psi_0 + H_p}{H_0 \sin \Psi_0} \tag{8}$$

where γ is the gyromagnetic ratio, and the dot represents differentiation with respect to time. The initial conditions are

$$\left. \begin{array}{l} M_x = M_y = 0 \\ M_z = 1 \end{array} \right\} \text{ at } t = 0,$$

the magnetization vector being normalized so that

$$M_x^2 + M_y^2 + M_z^2 = 1.$$

Terms due to the demagnetizing field do not appear inasmuch as the sample is spherical.
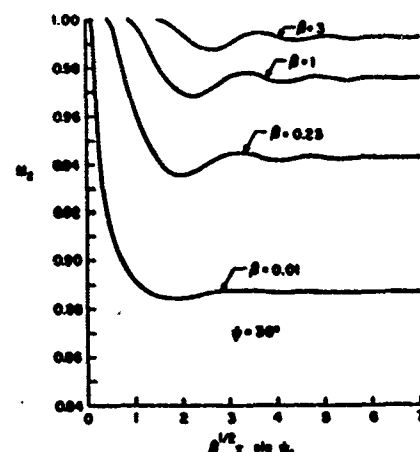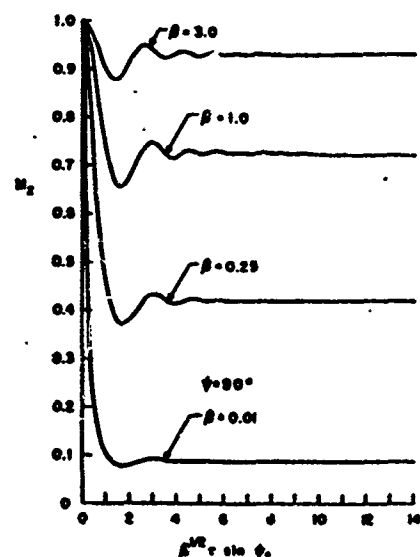
LINEAR PULSE SHAPES

In this section we will investigate the motion of M for linearly rising pulse shapes. If we change the independent variable from t to

$$\tau = \cot \overset{\circ}{\Psi},$$

then our equations assume the form

$$\frac{dM_x}{d\tau} = -\beta \sin^2 \Psi_0 (1 + \tau^2)^{1/2} M_y + \frac{M_z}{1 + \tau^2} \tag{9}$$

$$\frac{dM_y}{d\tau} = \beta \sin^2 \Psi_0 (1 + \tau^2)^{1/2} M_x \tag{10}$$

Fig. 3. Variation of M_z with $\beta^{1/2}\tau \sin \psi_0$ for $\psi_0 = 90°$.

$$\frac{dM_z}{d\tau} = \frac{-M_x}{1 + \tau^2}, \tag{11}$$

where

$$\beta = \frac{\gamma H_0^2}{\dot{H}_p}. \tag{12}$$

Starting at $\tau = \tau_0 = \cot \Psi_0$, these equations were numerically integrated on a digital computer with respect to τ until M_z approached a limiting value. This was repeated for various fixed values of Ψ_0 and β. A representative set of runs showing the variation of M_z with respect to $\beta^{1/2}\tau$ $\sin \Psi_0$ is shown in Figs. 2 and 3 for Ψ_0 equal to 30° and 90°, respectively. It can be seen from these solutions that there is very little oscillation in M_z when $\beta^{1/2}\tau \sin \Psi_0$ is greater than 10. The actual runs were carried out until $\beta^{1/2}\tau \sin \Psi_0$ equaled about 17.

In the case of each run, the limiting precession angle was determined by inserting the limiting value of M_z in the equation
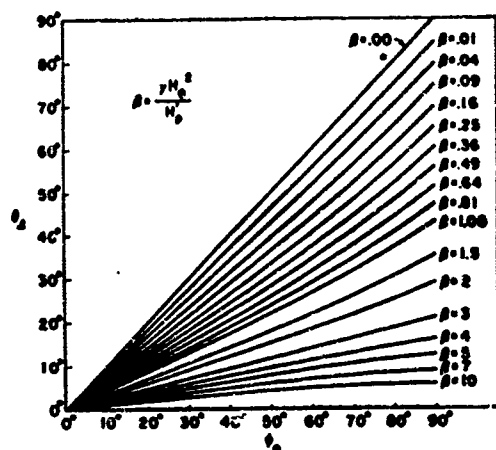
Fig. 4. Final precession angle Θ_l as a function of pulsing angle Ψ_0 with β as a parameter.
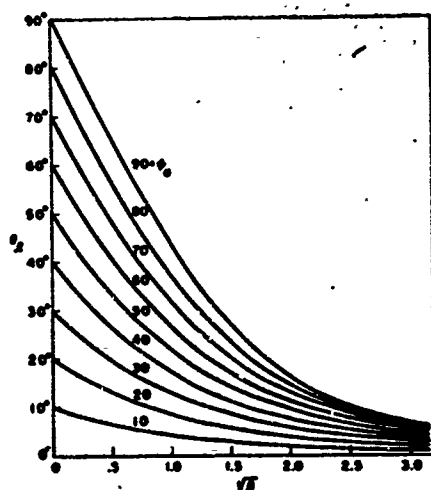

Fig. 5. Final precession angle Θ_l as a function of $\sqrt{\beta}$ with pulsing angle Ψ_0 as a parameter.

$$\Theta_l = \tan^{-1}\frac{(1 - M_z^2)^{1/2}}{M_z}.$$

The final precession angle Θ_l is plotted in Fig. 4 as a function of Ψ_0 with β as a parameter, while in Fig. 5, Θ_l is plotted as a function of $\sqrt{\beta}$ with Ψ_0 as a parameter. In the latter figure, the quantity $\sqrt{\beta}$ was chosen in order to straighten out the curves as much as possible. The choice of β and Θ_l as parameters for these curves is not unique, of course, and was chosen because the pulse-rise rate was varied and the precession angle held constant during the experiments, or vice versa.

Fortunately, it is also possible to obtain a closed-form solution for the final precession angle under simplifying assumptions which are often compatible with experimental conditions. In some experiments β is greater than 10, and consequently, as Fig. 5 suggests and more detailed calculations show, the precession angle under these circumstances is small. It is then valid to set M_z to unity in the

equations of motion. If we define

$$m = M_x + iM_y \tag{13}$$

and

$$u = \sqrt{\beta}\sin\Psi_0, \tag{14}$$

then (9)–(11) reduce to the single linear differential equation

$$\frac{dm}{d\tau} = iu^2(1 + \tau^2)^{1/2}m + \frac{1}{1 + \tau^2}. \tag{15}$$

It is known that this has a solution of the form

$$m = e^{-\int_0^\tau P\,d\tau}\int_{\tau_0}^\tau Qe^{\int P\,d\tau}\,d\tau, \tag{16}$$

where

$$P = -iu^2(1 + \tau^2)^{1/2}$$

$$Q = \frac{1}{1 + \tau^2}.$$

The precession angle is given by the relation.

$$\Theta = |m|,$$

when Θ is small. By letting τ approach infinity in (16) we obtain the expression for Θ_l. Since P is a pure imaginary, it follows that

$$\Theta_l = \left|\int_0^\infty Qe^{\int P\,d\tau}\,d\tau\right|. \tag{17}$$

Substitution then yields the final formula for Θ_l:

$$\Theta_l = \left|\int_{\tau_0}^\infty \frac{d\tau}{1 + \tau^2}\exp\left[i\frac{u^2}{2}\left\{\tau(1 + \tau^2)^{1/2} + \ln\left((1 + \tau^2)^{1/2} + \tau\right)\right\}\right]\right|. \tag{18}$$

The situation is even simpler when Ψ_0 is small. Since this implies that Θ is small also, it follows that (18) is again valid. Furthermore, since τ is now large, we can replace $(1 + \tau^2)^{1/2}$ by τ, and also neglect the term $\ln(1 + \tau^2)^{1/2}$. In this case, (18) reduces to

$$\Theta_l = \left|\int_{\tau_0}^\infty \frac{d\tau}{\tau^2}\exp\left(\frac{iu^2\tau^2}{2}\right)\right|. \tag{19}$$

Further reduction leads finally to the formula

$$R = \left\{\left[\cos\frac{\beta}{2} + \sqrt{\pi\beta}\left(S\left(\frac{\beta}{2}\right) - \frac{1}{2}\right)\right]^2 + \left[\sin\frac{\beta}{2} - \sqrt{\pi\beta}\left(C\left(\frac{\beta}{2}\right) - \frac{1}{2}\right)\right]^2\right\}^{1/2}, \tag{20}$$

where R is the ratio of Θ_l to Ψ_0, and S and C are the familiar Fresnel integrals. This formula has already been derived by E. Schlömann [2]. It is extremely useful since
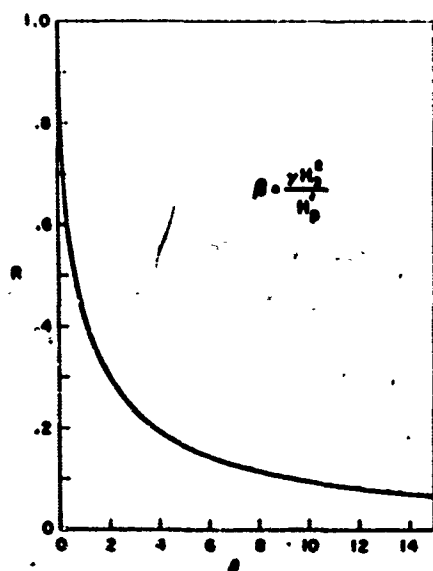
Fig. 6. Ratio R of Θ_t to ψ_0 as a function of β. This curve is valid only for small ψ_0.
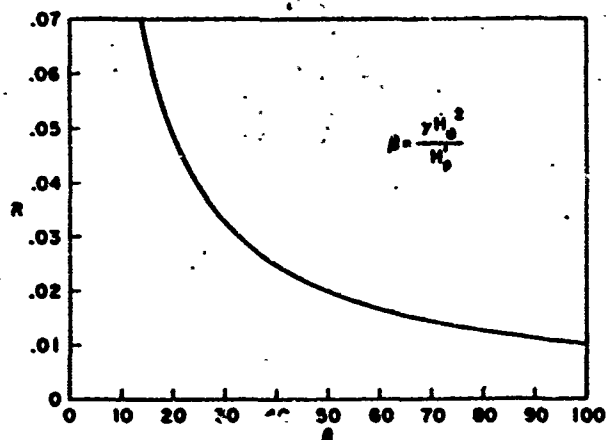
Fig. 7. Ratio R of Θ_t to ψ_0 as a function of β. This curve is valid only for small ψ_0.

it depends on only one parameter, β. Ratio R was evaluated numerically and has been plotted in Figs. 6 and 7 as a function of β.

NONLINEAR PULSE SHAPES

It is also possible to derive a simple formula for the final precession angle which holds for both linear and nonlinear pulses when the pulse-rise rate is slow.

If we assume that the pulse rises slowly enough to keep Ψ small, then M_t can be set to one. By using the variable m of (13), we obtain from (4)–(6) the relation

$$\dot{m} = i\gamma H m + \frac{H_0 \sin \Psi_0}{H^2} \dot{H}_p. \qquad (22)$$

If we let

$$m = m_0 e^{i\lambda},$$

where

$$\lambda = \int_0^t \gamma H \, dt,$$

then (22) reduces to

$$\frac{dm_0}{d\lambda} = \frac{H_0 \sin \Psi_0}{\gamma H^2} \dot{H}_p e^{-i\lambda}. \qquad (23)$$

By integrating, we obtain the solution

$$m_0 = \int_0^\lambda \frac{H_0 \sin \Psi_0}{\gamma H^2} \dot{H}_p e^{-i\lambda} d\lambda. \qquad (24)$$

Because Ψ is small, the precession angle is given by

$$\Theta = |m| = |m_0|.$$

The final precession angle is given, therefore, by

$$\Theta_t = \left| \int_0^\infty \frac{H_0 \sin \Psi_0}{\gamma H^2} \dot{H}_p e^{-i\lambda} d\lambda \right|. \qquad (25)$$

We now make an asymptotic expansion of (25) in inverse powers of H_0 by partial integration. The first integration by parts yields the relation

$$\Theta_t = \left| \frac{\sin \Psi_0}{\gamma H_0^2} \dot{H}_{p0} + \int_0^\infty e^{-i\lambda} \frac{d}{d\lambda} \left(\frac{H_0 \sin \Psi_0}{\gamma H^2} \dot{H}_p \right) d\lambda \right|, \qquad (26)$$

where $\dot{H}_{p0}$ is the value of $\dot{H}_p$ at $t = 0$. If the pulse-rise rate is slow, it seems plausible that the integral in this expression can be neglected. This premise is consistent with the results of a number of digital computer runs.

We obtain, therefore, the expression

$$\Theta_t = \frac{\sin \Psi_0}{\gamma H_0^2} \dot{H}_{p0}, \qquad (27)$$

for the final precession angle. This expression holds for slowly rising linear and nonlinear pulse shapes. One should note that for small Ψ_0 this result is identical to the asymptotic form of (20) for large β. In terms of computer studies made in connection with this work, the condition of slow pulse-rise rate corresponds to the condition

$$\beta = \frac{\gamma H_0^2}{\dot{H}_{p0}} \gg 1.$$

For example, when β is 10, accuracies of the order of one to two percent are obtained in Θ_t. It should be noted, however, that the transition from (26) to (27) is not justified if $\dot{H}_{p0}$ is sufficiently small.

The reason why the initial portion of the pulse is so important in determining the final precession angle stems from the fact that $\dot{\Psi}$ approaches zero, provided $\dot{H}_p$ is bounded, as H_p grows large. This is most easily seen by examining the equation obtained from (8) by differentiating with respect to t. Referring to (4)–(6), it is clear then that changes in H_p change only the magnitude of H, thus raising the precession frequency without changing the precession angle.

SUMMARY

By using the results of this paper it should be possible to determine the precession angle set up by pulsed magnetic fields under a variety of conditions. Figures 4 and 5

give these results for large pulsing angles and fast linear pulses. Equation (20) or Figs. 6 and 7 are valid for small pulsing angles and linear pulses. Equation (27) can be used for slow pulses, linear and nonlinear, and arbitrary pulsing angles.

REFERENCES

[1] F. R. Morgenthaler, "Microwave radiation from ferrimagnetically coupled electrons in transient magnetic fields," *IRE Trans. on Microwave Theory and Techniques*, vol. MTT-7, no. 1, pp. 6–11, January 1959.

[2] E. Schlömann, Microwave Lab. Rept., Stanford University Stanford, Calif., unpublished.

[3] H. Brunet, *Compt. Rend.*, vol. 252, p. 2860, 1961.

[4] H. J. Shaw and B. J. Elliott, "Generation of microwave radiation with ferrimagnetic samples subjected to pulsed magnetic fields," *1963 Conference on Magnetic and Electric Resonance and Relaxation*. Amsterdam: North Holland Publishing Co., p. 770.

[5] H. Suhl, "The nonlinear behavior of ferrites at high microwave signal levels," *Proc. IRE*, vol. 44, pp. 1270–1284, October 1956.

[6] E. Schlömann, "Ferromagnetic resonance at high power levels," Raytheon Co., Waltham, Mass., Research Div., Raytheon Rept. R-48, October 1, 1959.

[7] E. Schlömann, *J. Appl. Phys.*, vol. 33, p. 2822, 1962.

[8] K. J. Harker and H. J. Shaw, *J. Appl. Phys.*, vol. 35, p. 902, 1964.

APPENDIX B

TRANSIENT SPIN WAVE BUILDUP IN FERRITES[*]

by

K. J. Harker and H. J. Shaw
Stanford University
Stanford, California

ABSTRACT

The equations of motion for spin waves in a ferrite, together with
the equations for the uniform mode, have been numerically integrated for
the case in which the ferrite is subjected to an applied magnetic field
which rises linearly in time. The equations for the uniform mode are
completely general and allow for arbitrary amplitude of the mode, so
that parametric couplings which lead to spin wave instabilities of
various orders are accounted for, including the ordinary first-order
and second-order spin wave instabilities. The spin wave equations are
solved to first order in the spin wave amplitudes.

The equations have been solved under the conditions of a linearly
rising magnetic field having arbitrary rate of rise, together with a dc
applied magnetic field of arbitrary magnitude, and for arbitrary angle ·
between the orientations of the rising and dc fields. Assuming that
spin waves are initially excited to thermal amplitudes, a numerical inte-
gration is performed over $\underline{k}$-space to find the aggregate spin wave growth

as a function of time, and the energy in the uniform mode as a function of time in the presence of the amplified spin waves. These results define the conditions under which useful transient devices can be operated for the generation of microwave energy in pulsed magnetic fields, to take advantage of the large rf magnetization available in ferrites when operated beyond the usual limiting values of the uniform mode which apply under steady-state operation.

INTRODUCTION

It has been shown[1,2] that a small ferrite sample subjected to a
suitable pulsed magnetic field can constitute a coherent oscillator for
the generation of microwave energy. Theoretical considerations involved
in this device have been studied by several authors,[3-6] and also some
studies of another, but closely related, pulsed ferrite device are
relevant[7-9] to some aspects of the present device.

The basic process involved is the establishment of an angle Θ
between the total applied magnetic field and the magnetization in the
ferrite, by applying a pulsed magnetic field at a geometrical angle Ψ_0
to the initial direction of the magnetization, the latter being determined
by a dc bias field. The final precession angle Θ , for the uniform
mode, which results when spin wave amplification is ignored, has been
investigated theoretically over a broad range of physical parameters.[6]

An important practical limitation on the operation of such devices
results from the intrinsic parametric pumping of spin waves, by which
energy is drawn from the uniform mode into spin waves where it is no
longer available for radiative extraction. In steady state problems,
spin wave phenomena of this kind have been widely studied and are well
known.[10-12] A study of the mechanisms of spin wave growth under the
present transient circumstances was reported recently,[13] but this study
did not take into account analytically the back reaction of the spin
waves on the uniform mode.

This paper presents a theory and calculations which specify quantitatively the limitations imposed by spin-wave growth on the energy available for radiative extraction from spherical, isotropic samples subjected to linearly rising pulses of magnetic field. The equations of motion for the uniform mode and the equations of motion for spin-wave modes for all regions of k-space which undergo pumping are integrated numerically, assuming initial spin-wave excitation at the level corresponding to thermal equilibrium. No restrictions are imposed on the values of the dc bias field, the pulsing angle, mode amplitude, or the rate of rise of the pulsed field. All terms are retained in the equations for the uniform mode. In the spin-wave equations, terms to first order in the spin-wave amplitudes are retained. The integration of the uniform mode equations requires a repeated integration over that region of k-space in which spin waves are being pumped. Another integration over k-space at each time step gives the spin-wave energy as a function of time.

The paper concludes with a discussion of the asymptotic spin-wave growth rates and an investigation of the region in k-space over which pumping would be expected to occur.

CALCULATION OF THE PATH OF THE SPIN WAVE AND UNIFORM MODE MAGNETIZATION

Because of the unwieldy nature of the equations to be dealt with, tensor notation will be used throughout. In particular, δ_{ij} and δ_{ijk} will represent the Kroniker delta symbol and Levi-Civita tensor density, respectively. Vector quantities and components are referred to with an upper bar and subscript, respectively; for example, $\bar{H}$ and H_n . Referring to the fixed coordinate system shown in Fig. 1, the sample is assumed to be initially magnetized to saturation by a constant field with components

$$H_1' = H^0 \sin \psi_0$$

$$H_2' = 0 \qquad\qquad\qquad (1)$$

$$H_3' = H^0 \cos \psi_0 \qquad ,$$

where H^0 is the magnitude of the saturation field.

A linear pulse of magnetic field, $\overline{H^p}$ is then assumed to be applied along the x_3-axis. It is convenient to introduce the moving coordinate system also shown in Fig. 1. The x_3-axis of this system is chosen to coincide with the total applied magnetic field, $\bar{H} = \overline{H^0} + \overline{H^p}$, and the x_2-axis with the fixed systems x_2'-axis. The angle ψ lies between the x_3 and x_3'-axes, and ψ_0 is chosen to be the value of ψ at the initiation of the pulse. In this coordinate system the magnetization obeys the equation of motion given by

$$\frac{dM_n}{dt} = -\delta_{npq} M_p (\gamma H_q^s - \delta_{2q} \frac{d\psi}{dt}) \qquad , (2)$$

where $\overline{M}$ is the total magnetization vector, $\overline{H}^s$ is the total field, t is the time, and γ is the gyromagnetic ratio. The second term arises from the motion of the coordinate system about the y-axis. We may expand $\overline{M}$ into a spatial Fourier series

$$M_m = M\left(\alpha_{om} + \sum_{k \neq 0} \alpha_{km}\, e^{ik_r x_r}\right) \quad , \qquad (3)$$

where M is the magnitude of $\overline{M}$,

$$H_q^s = \delta_{3q}H - (4\pi M/3)\alpha_{oq} - \sum_{\overline{k} \neq 0} \frac{4\pi M}{k^2} k_r \alpha_{kr} k_q\, e^{ik_r x_r} - \sum_{\overline{k} \neq 0} Dk^2 \alpha_{kq}\, e^{ik_r x_r} \quad ,$$

$$(4)$$

D is the product of the exchange field times the square of the lattice spacing, and k is the magnitude of the propagation vector $\overline{k}$. By substituting Eqs. (3) and (4) into the equation of motion, setting the coefficient of each term in the Fourier expansion to zero, and ignoring quadratic terms in α_{km} in the spin wave equations we find that

$$\frac{d\alpha_{on}}{dt} = -\gamma\left[\delta_{npq}\alpha_{op}\delta_{3q} H - \sum_{\overline{k} \neq 0} \frac{4\pi M}{k^2} \delta_{npq}\, \alpha_{kp}\, k_q k_r\, \alpha_{kr}^*\right] + \delta_{npq}\alpha_{op}\delta_{2q}\frac{d\psi}{dt} \quad ,$$

$$(5)$$

and

$$\frac{d\alpha_{kn}}{dt} = \gamma\left[\delta_{npq}\alpha_{kp}\left(\frac{4\pi M}{3}\alpha_{oq} - H\delta_{3q} - Dk^2\alpha_{oq}\right) + \frac{4\pi M}{k^2}\delta_{npq}\alpha_{op}k_q k_r\, \alpha_{kr}\right] \quad .$$

$$+ \delta_{npq}\,\alpha_{kp}\,\delta_{2q}\frac{d\psi}{dt} \quad . \qquad (6)$$

It is convenient at this point to introduce a change of variables. We define

$$\tau = \text{ctn } \psi = \frac{H^o \cos \psi_o + H^p}{H^p \sin \psi_o} \qquad (7)$$

$$\beta = \frac{\gamma (H^o)^2}{\dfrac{dH_p}{dt}} \qquad (8)$$

$$\ell_1 = \frac{k_1}{k} = \sin \Theta_k \cos \phi_k \qquad (9)$$

$$\ell_2 = \frac{k_2}{k} = \sin \Theta_k \sin \phi_k \qquad (10)$$

$$\ell_3 = \frac{k_3}{k} = \cos \Theta_k \quad , \qquad (11)$$

where H^p is the magnitude of $\overline{H^p}$. In terms of the new variable τ , we note that

$$H = H^o \sin \psi_o (1 + \tau^2)^{1/2} \qquad (12)$$

$$\frac{d\tau}{dt} = \frac{\gamma H^o}{\beta \sin \psi_o} \qquad (13)$$

$$\frac{d\psi}{d\tau} = - \frac{1}{1 + \tau^2} \quad . \qquad (14)$$

By substituting these equations into Eqs. (5) and (6) we obtain

$$\frac{d\alpha_{on}}{d\tau} = \beta \sin^2 \psi_o (1 + \tau^2)^{1/2} \delta_{npq} \delta_{3p} \alpha_{oq} + \frac{4\pi M}{H^o} \beta \sin \psi_o \sum_{k \neq 0} \delta_{npq} \ell_q \ell_r \alpha_{kp} \alpha^*_{kr}$$

$$- \frac{\delta_{npq} \alpha_{op} \delta_{2q}}{1 + \tau^2} \tag{15}$$

and

$$\frac{d\alpha_{kn}}{d\tau} = \delta_{npq} \alpha_{kp} \left[\beta \sin \psi_o \frac{4\pi M/3 - Dk^2}{H^o} \alpha_{oq} - \beta \sin^2 \psi_o (1 + \tau^2)^{1/2} \delta_{3q} \right]$$

$$+ \beta \sin \psi_o \frac{4\pi M}{H^o} \delta_{npq} \alpha_{op} \ell_q \ell_r \alpha_{kr} - \frac{\delta_{npq} \alpha_{kp} \delta_{2q}}{1 + \tau^2} \quad . \tag{16}$$

The calculations in this paper will be based on the assumption that the spin waves are initially in thermal equilibrium. Statistically, one can obtain no information from studying the components of $\bar{\alpha}_k$, since they average to zero. The quantities that must be considered are the quadratic terms in α_{km} . Accordingly, we define the tensor

$$\epsilon_{kmn} = \frac{4\pi M^2 V}{3KT} \operatorname{Re} \langle \alpha_{km} \alpha^*_{kn} \rangle_{AV} \quad , \tag{17}$$

where K is Boltzmann's constant, V is the periodic volume, and T is the temperature in degrees Kelvin. Taking the ensemble average of

Eq. (15) and then substituting Eq. (17) gives

$$\frac{d\alpha_{on}}{d\tau} = \beta \sin^2 \psi_o (1 + \tau^2)^{1/2} \delta_{npq} \delta_{3p} \alpha_{oq} + \overset{\circ}{\beta} \sin \psi_o \frac{3K\,T}{MV\hbar^o} \sum_{\bar{k}\neq 0} \delta_{npq} \ell_q \ell_r \epsilon_{kpr}$$

$$- \frac{\delta_{npq} \alpha_{op} \delta_{2q}}{1 + \tau^2} \quad , \tag{18}$$

where α is now understood to henceforth represent the ensemble average.
In order to obtain equations for the ϵ_{kmn} , we multiply Eq. (16) by
α_{km}^* . We then permute m and n , take the complex conjugate, and
add the original and permuted equations, obtaining an expression for
$d/d\tau(\alpha_{kn}\alpha_{km}^*)$. Taking the real part of the ensemble average then gives

$$\frac{d\epsilon_{kmn}}{d\tau} = (\delta_{npq} \epsilon_{kpm} + \delta_{mpq} \epsilon_{kpn}) \left[\beta \sin \psi_o \frac{4\pi M/3 - Dk^2}{H^o} \alpha_{oq} \right.$$

$$\left. - \beta \sin^2 \psi_o (1 + \tau^2)^{1/2} \delta_{3q} \right]$$

$$+ \beta \sin \psi_o \frac{4\pi M}{H^o} \alpha_{op} \ell_q \ell_r (\delta_{npq} \epsilon_{krm} + \delta_{mpq} \epsilon_{krn}) + \frac{\delta_{2p}(\delta_{npq} \epsilon_{kmq} + \delta_{mpq} \epsilon_{kng})}{1 + \tau^2}$$

$$\tag{19}$$

Since ϵ_{kmn} is symmetric, this represents six equations for each value
of $\bar{k}$.

In order to bring Eq. (18) into final form, it will be necessary
to replace the summation over $\bar{k}$ by a suitable approximating integral.

If we define c and $\mathcal{L}$ by the relations

$$c = \frac{k}{(4\pi M/3D)^{1/2}} \tag{20}$$

$$\mathcal{L} = \frac{KT(4\pi M/3)^{1/2}}{H^o D^{3/2} \pi^2} \quad , \tag{21}$$

then it can be shown that

$$\sum_{\bar{k} \neq 0} = \frac{MV\mathcal{L}H^o}{3K T} \int_0^1 c^2 dc \int_0^{2\pi} d\phi_k \int_0^{\pi/2} \sin \Theta_k \, d\Theta_k \quad . \tag{22}$$

In deriving this relation we have used the fact that the integrand is
identical for $\bar{k}$ and $-\bar{k}$. The limits on c are chosen to include
only that portion of the spin wave manifold which is pumped, as will be
shown in the last section of this paper. By substituting into Eq. (18)
we have

$$\frac{d\alpha_{on}}{d\tau} = \beta \sin^2 \psi_o (1 + \tau^2)^{1/2} \delta_{npq} \delta_{3p} \alpha_{oq}$$

$$+ \beta\mathcal{L} \sin \psi_o \int_0^1 \int_0^{2\pi} \int_0^{\pi/2} c^2 dc \, d\phi_k \sin \Theta_k \, d\Theta_k \, \delta_{npq} \ell_q \ell_r \epsilon_{kpr} - \frac{\delta_{npq} \alpha_{op} \delta_{2q}}{1 + \tau^2} \quad . \tag{23}$$

In order to integrate Eqs. (19) and (23), the initial conditions must
be obtained. Since the only spin waves which will be pumped are of long
wavelength, classical statistics will suffice. The first step is to obtain

an expression for the energy by classical methods. This is done by calculating the energy retrieved from the system by forcing the spins back into the positions they would occupy at absolute zero. To establish the energy of a given state, one must evaluate the integral

$$E = -\int\int H_n^s \, dM_n \, dV \, , \qquad (24)$$

where the lower limit corresponds to the configuration where all spins are parallel to the applied magnetic field, and the upper limit corresponds to the configuration associated with the given state. Here H_n is given by Eq. (4) and dM_n is given by the differential of Eq. (3):

$$dM_n = M(d\alpha_{on} + \sum_{k \neq 0} d\alpha_{kn} \, e^{ik_r x_r}) \qquad . \qquad (25)$$

By substituting into Eq. (24) and integrating we obtain

$$E = VM\left\{-H\Delta\alpha_{o3} + \frac{4\pi M}{6}\Delta(\alpha_{or}\alpha_{or}) + \sum_{k \neq 0}\left[2\pi M|\ell_r \alpha_{kr}|^2 + \frac{Dk^2}{2}\alpha_{kr}\alpha_{kr}^*\right]\right\} \qquad , \qquad (26)$$

where Δ signifies difference between the final and initial values. We find that

$$\Delta\alpha_{o3} = \cos\Theta\left(1 - \sum_{k=0}\alpha_{kr}\,\alpha_{kr}^*\right)^{1/2} - 1$$

$$= \cos\Theta\left(1 - \frac{1}{2}\sum_{k \neq 0}\alpha_{kr}\,\alpha_{kr}^*\right) - 1 \qquad (27)$$

- 90 -

and

$$\Delta(\alpha_{or}\,\alpha_{or}) = \alpha_{or}\,\alpha_{or} - 1 = -\sum_{\vec{k}\neq 0} \alpha_{kr}\,\alpha_{kr}^{*} \quad , \qquad (28)$$

where Θ is the angle between $\vec{\tilde{\alpha}}_o$ and $\vec{H}$. By substituting into Eq. (26) and simplifying we obtain

$$E = E_{UM} + E_{SW} \quad , \qquad (29)$$

where

$$E_{UM} = MVH(1 - \cos \Theta)(\alpha_{or}\,\alpha_{or})^{1/2} \qquad (30)$$

is the energy in the uniform mode and

$$E_{SW} = \frac{MV}{2} \sum_{\vec{k}\neq 0} \left[\left(H - \frac{4\pi M}{3} + Dk^2 \right) \alpha_{kr}\,\alpha_{kr}^{*} + 4\pi M\, |\ell_r \alpha_{kr}|^2 \right] \quad (31)$$

is the energy of the spin waves. Taking the ensemble average of Eq. (31) and substituting Eqs. (17) and (22) reduces the equation for E_{SW} to the form

$$E_{SW} = \frac{MVH\mathcal{E}}{6 \sin \psi_c (1 + \tau^2)^{1/2}} \int_0^1 \int_0^{2\pi} \int_0^{\pi/2} c^2 dc \, d\phi_k \, \sin \Theta_k \, d\Theta_k$$

$$\times \left[\left(\frac{3H}{4\pi M} - 1 + c^2 \right) \left(\sum_m \epsilon_{kmm} \right) + 3\ell_m \ell_n \, \epsilon_{kmn} \right] \quad , \qquad (32)$$

where

$$H = (1 + \tau^2)^{1/2} (\sin \psi_o) H^0 \quad . \tag{33}$$

Since the summand in Eq. (31) is independent of the sign of $\bar{k}$, the total energy associated with the $\bar{k}$ and $-\bar{k}$ spin waves is given by

$$E_k = MV \left[\left(H - \frac{4\pi M}{3} + Dk^2 \right) \alpha_{kr} \alpha_{kr}^* + 4\pi M |\ell_r \alpha_{kr}|^2 \right] \quad . \tag{34}$$

At thermal equilibrium α_{k3} is taken as zero. Letting subscripts r and i stand for real and imaginary parts, respectively, we can write this equation as

$$E_k = MV \left\{ \left(H - \frac{4\pi M}{3} + Dk^2 \right) \left(\alpha_{k1,r}^2 + \alpha_{k2,r}^2 \right) + 4\pi M (\ell_1 \alpha_{k1,r} + \ell_2 \alpha_{k2,r})^2 \right.$$

$$\left. + \left(H - \frac{4\pi M}{3} + Dk^2 \right) \left(\alpha_{k1,i}^2 + \alpha_{k2,i}^2 \right) + 4\pi M (\ell_1 \alpha_{k1,i} + \ell_2 \alpha_{k2,i})^2 \right\} \quad .$$

$$\tag{35}$$

Note that r and i are not running symbols. The mean-squared values of α_{k1}^2 , α_{k2}^2 , etc., are then calculated according to the formulae

$$\langle \alpha_{km,r} \alpha_{kn,r} \rangle_{AV} = \frac{\iint \alpha_{km,r} \alpha_{kn,r} e^{-E_k/kT} \, d\alpha_{km,r} \, d\alpha_{kn,r}}{\iint e^{-E_k/kT} \, d\alpha_{km,r} \, d\alpha_{kn,r}} \quad . \tag{36}$$

Note here again that m and n are not running symbols in this equation. By evaluating these integrals we obtain the relations

$$\langle \alpha_{k1,r}^2 \rangle_{AV} = \frac{KT}{2MVX} (H^o - \frac{4\pi M}{3} + Dk^2 + 4\pi M \ell_2^2) \qquad (37)$$

$$\langle \alpha_{k2,r}^2 \rangle_{AV} = \frac{KT}{2MVX} (H^o - \frac{4\pi M}{3} + Dk^2 + 4\pi M \ell_1^2) \qquad (38)$$

$$\langle \alpha_{k1,r} \alpha_{k2,r} \rangle_{AV} = - \frac{KT}{2MVX} 4\pi M \ell_1 \ell_2 \quad , \qquad (39)$$

where

$$X = (H^o - \frac{4\pi M}{3} + Dk^2)(H^o - \frac{4\pi M}{3} + Dk^2 + 4\pi M \sin^2 \theta_k) \quad .$$

$$(40)$$

Identical expressions are obtained for $\langle \alpha_{k1,i}^2 \rangle_{AV}$, $\langle \delta_{k,2i}^2 \rangle_{AV}$, and $\langle \alpha_{k1,i} \alpha_{k2,i} \rangle_{AV}$. Substituting the above equations

$$\text{Re} \langle \alpha_{km} \alpha_{kn}^* \rangle_{AV} = 2 \langle \alpha_{km,r} \alpha_{kn,r} \rangle_{AV} \qquad (41)$$

into Eq. (17), we obtain, finally, the initial values of ϵ_{kmn} :

$$\epsilon_{k11} = (3H^o/4\pi M - 1 + c^2 + 3 \ell_2^2)/\xi \qquad (42)$$

$$\epsilon_{k22} = (3H^o/4\pi M - 1 + c^2 + 3\ell_1^2)/\xi \qquad (43)$$

$$\epsilon_{k33} = 0 \qquad (44)$$

$$\epsilon_{k12} = - 3\ell_1 \ell_2/\xi \qquad (45)$$

$$\epsilon_{k23} = 0 \qquad\qquad (46)$$

$$e_{k31} = 0 \qquad\qquad (47)$$

where

$$\xi = (\frac{3H^o}{4\pi M} - 1 + c^2)(\frac{3H^o}{4\pi M} - 1 + c^2 + 3\sin^2\theta_k) \qquad . \qquad (48)$$

Equations (19) and (23) were integrated simultaneously by the Kutta-Runge numerical method for discrete set of $\bar{k}$ values covering the region of growing waves described by the limits of the integral in Eq. (22). The initial conditions for these equations are given by Eq. (42) - (47) with $H^o = 4\pi M/3$. The uniform mode was given an initial amplitude of

$$\alpha_{o3} = \alpha_R = 0.761 \qquad , \qquad\qquad (49)$$

corresponding to YIG at room temperature.[14] . The other numerical constants chosen were $D = 4.4 \times 10^{-9}$ Oe-cm^2 , $T = 293^o$K , $K = 1.38 \times 10^{-10}$ erg/deg, and $\gamma = 17.6$ (nsec-koe)$^{-1}$. The value of D was taken from Schlömann.[15] At each point in the Runge-Kutta integration of Eq. (23) where the derivatives of the dependent variable are evaluated the integral appearing in the equation was evaluated by Simpson's rule using the discrete set of $\bar{k}$ values as mesh points. The spin wave energy was evaluated with Eq. (31) by Simpson's rule in the same manner as the integral in Eq. (23).

The end result of these calculations is the variation of α_{kn} , ϵ_{kmn} , E_{UM} , and E_{SW} as a function of time. In all, six different cases,

corresponding to six pairs of values of β and ψ_o, were studied. Two of these cases are plotted in Figs. 2 and 3, where $\alpha_N = (\alpha_{or} \alpha_{or}^*)/\alpha_R$, Θ, E_{UM}/MVH, and E_{SW}/MVH are plotted as a function of normalized time:

$$\gamma H_o t = \beta \sin \psi_o (\tau - ctn\psi_o) \quad . \tag{50}$$

An important quantity related to the use of pulsed ferrites as a microwave energy source is the amount of energy available for radiative extraction. The ratio

$$R = \frac{(1 - \cos \Theta)(\alpha_{or} \alpha_{or})^{1/2}}{(1 - \cos \Theta_\ell) \alpha_R} \tag{51}$$

representing the ratio of the energy in the uniform mode to the energy in the uniform mode without spin waves was chosen as a measure of this. The ultimate precession angle Θ_ℓ attained by the uniform mode without spin waves has been calculated in a previous report.[5] Values of Θ_ℓ from the report are presented in Table I for the six cases studied. Also presented in the table are the values of E_{UM}/MVH corresponding to a 10% degradation in the uniform mode energy $(R = 0.9)$ as calculated from the formula

$$E_{UM}/MVH = R\alpha_R(1 - \cos \Theta_\ell) \quad . \tag{52}$$

In the last row of the table are given the normalized times, $\gamma H_o t$, corresponding to the 10% degradation of the uniform mode energy as read off from curves for the six cases of which Figs. 2 and 3 are examples. These results are further summarized in Fig. 4, where the final precession

- 95 -

angle Θ_ℓ , is plotted versus the normalized time, $\gamma H_o t$, corresponding

to $R = 0.9$. One will note that the normalized time for R to attain

a particular value is dependent primarily on Θ_ℓ , and not on the

particular combination of β and ψ_o required to give Θ_ℓ .

TABLE I

NORMALIZED TIME FOR 10% DEGRADATION OF UNIFORM CODE

ψ_o	$90°$	$90°$	$90°$	$70°$	$50°$	$45°$
β	.4	.6	.8	.6	.4	.8
Θ_ℓ	58.9.	52.7	47.6	38.5	29.8	21.2
$0.9(1 - \cos \Theta_\ell) \alpha_R$	.331	.270	.223	.1485	.0903	.0465
$\gamma H_o t$	5.14	5.82	6.5	8.23	11.0	16.5

We may obtain a useful relation from Eq. (3). Taking the dot

product of this equation by itself gives a spatial Fourier series, the

constant term of which yields the well known relation

$$\alpha_{or} \, \alpha_{or} \; = \; 1 - \sum_{k \ne 0} \alpha_{kn} \, \alpha_{kr}^{*} \qquad . \qquad (53)$$

Introduction of normalized variables then leads to the equation

$$\alpha_{or} \, \alpha_{or} \; = \; 1 - \frac{\ell}{3} \frac{3H^o}{4\pi M} \int_0^1 \int_0^{2\pi} \int_0^{\pi/2} c^2 dc \; d\phi_k \; \sin \Theta_k \; d\Theta_k \sum_r \epsilon_{krr} \qquad .$$

$$(54)$$

This equation was used as a second means for calculating $(\alpha_{or} \alpha_{or})^{1/2}$ and thus also as a consistency check on the numerical results obtained from integrating Eqs. (19) and (23).

ASYMPTOTIC SPIN WAVE GROWTH

Wh.. e pulse of magnetic field has been applied long enough for the initial transient to die out, but not long enough for the uniform mode to have been seriously degraded, the spin wave growth rate approaches an exponential value which is readily calculable. The analytical results obtained here are particularly useful in evaluating the range in k-space in which pumping occurs. It will also be seen that the domain of growth is radically different for large and small precession angles. Our starting point is Eqs. (5) and (6) without the back-reaction terms in $\alpha_{kp} \alpha_{kr}^{*}$ and without the term in $\dot{\psi}$

$$\frac{d\alpha_{on}}{dt} = -\gamma \delta_{npq} \alpha_{op} \delta_{q3} H \tag{55}$$

$$\frac{d\alpha_{kn}}{dt} = \gamma \left[\delta_{npq} \alpha_{kp} \left(\frac{4\pi M}{3} \alpha_{oq} - H\delta_{3q} - Dk^2 \alpha_{oq} \right) + \frac{4\pi M}{k^2} \delta_{npq} \alpha_{op} k_q k_r \alpha_{kr} \right] \tag{56}$$

From these simplified equations we can show that $\alpha_{or} \alpha_{kr} = 0$, or for $\ell \neq 0$, or

$$\alpha_{k3} = -(\alpha_{01} \alpha_{k1} + \alpha_{02} \alpha_{k2})/\alpha_{03} \tag{57}$$

Let us make the definitions

$$\alpha_0 = \alpha_{01} + i\,\alpha_{02} \tag{58}$$

$$\alpha_k = \alpha_{k1} + i\,\alpha_{k2} \tag{59}$$

$$\ell = \ell_1 + i\,\ell_2 \tag{60}$$

and

$$\rho = \ell_3\,\alpha_0 - \alpha_{03}\,\ell \quad . \tag{61}$$

We then obtain

$$\frac{d\alpha_k}{dt} = i\gamma\left\{ H\alpha_k + \left(\frac{4\pi M}{3} - Dk^2\right)(\alpha_0\alpha_{k3} - \alpha_{03}\alpha_k) - \frac{4\pi M}{2\alpha_{03}}\,[\alpha_{03}(\ell\alpha_k^* + \ell^*\alpha_k) \right.$$
$$\left. - \ell_3(\alpha_0\,\alpha_k^* + \alpha_0^*\,\alpha_k)]\,(\ell_3\,\alpha_0 - \alpha_{03}\,\ell)\right\} \quad . \tag{62}$$

By substituting Eq. (57) and simplifying we obtain

$$\frac{d\alpha_k}{dt} = i\gamma\left\{\left[H + \frac{4\pi M|\rho|^2}{2\alpha_{03}} - \frac{(4\pi M/3 - Dk^2)}{2\alpha_{03}}(1 + \alpha_{03}^2)\right]\alpha_k + \left[\frac{4\pi M\rho^2}{2\alpha_{03}} - \frac{4\pi M/3 - Dk^2}{2\alpha_{03}}\alpha_0^2\right]\alpha_k^*\right\} \quad . \tag{63}$$

Using Eq. (61), we see that

$$\rho^2 = \ell_3^2\,\alpha_0^2 - 2\,\ell\ell_3\,\alpha_0\,\alpha_{03} + \alpha_{03}^2\,\ell^2$$

$$|\rho|^2 = \ell_3^2\,\alpha_{0T}^2 + \alpha_{03}^2\,\ell_T^2 - \alpha_{03}\ell_3(\ell\alpha_0^* + \ell^*\alpha_0) \quad , \tag{64}$$

- 98 -

where

$$\alpha_{OT} = |\alpha_0| \quad , \quad \alpha_{kT} = |\alpha_k| \quad , \quad \text{and} \quad \ell_T = |\ell| \quad . \tag{65}$$

It is clear from Eq. (55) that the solution for α_0 can be written as

$$\alpha_0 = \alpha_{OT} \, e^{i\omega t} \quad , \tag{66}$$

where $\omega = \gamma H$, provided the time origin is properly chosen. If we write α_k as $\hat{\alpha}_k \, e^{i\omega t}$, then it is clear that most terms will vary as $e^{i\omega t}$, corresponding to second-order pumping. Terms in other time variations than $e^{i\omega t}$ will also be present which correspond to first-order pumping and small frequency shifts, but more detailed analysis shows that they play a negligible role. Retaining only terms in $e^{i\omega t}$, we obtain from Eq. (63) the relation

$$\frac{d\hat{\alpha}_k}{dt} = ia\hat{\alpha}_k + ib\hat{\alpha}_k^* \quad , \tag{67}$$

where

$$a = \frac{\gamma}{2\alpha_{03}} \left[4\pi M(\ell_3^2 \, \alpha_{OT}^2 + \alpha_{03}^2 \, \ell_T^2) - (1 + \alpha_{03}^2)\left(\frac{4\pi M}{3} - Dk^2\right) \right] \tag{68}$$

$$b = \frac{\gamma}{2\alpha_{03}} [4\pi M \ell_3^2 - (4\pi M/3 - Dk^2)] \, \alpha_{OT}^2 \quad . \tag{69}$$

Asymptotically, as t becomes large, α_{03} and α_{0T} becomes constant. Equations (68) and (69) show that this also applies to a and b . Consequently, we can set $\hat{\alpha}_k$ equal to a real constant multiplied by $e^{\kappa t + i\phi}$. Substituting this into Eq. (67), we obtain the relations

$$\kappa^2 + a^2 = b^2 \tag{70}$$

and

$$\cos 2\phi = -\frac{a}{b} \ . \tag{71}$$

Substituting Eqs. (68) and (69), we have the equations for κ and ϕ :

$$\kappa = \pm \gamma \left[\frac{4\pi M}{3}\left(1 - \frac{3\ell_T^2}{2}\right) - Dk^2\right]^{1/2} \left[Dk^2 - \frac{4\pi M}{3}\left(1 - \frac{3\ell_T^2}{2}\right)\left(1 - 3\alpha_{0T}^2\right)\right]^{1/2} \tag{72}$$

$$\cos\phi = \frac{\alpha_{03}}{\alpha_{0T}} \left[\frac{\left(1 - \frac{3\ell_T^2}{2}\right) - \frac{Dk^2}{4\pi M/3}}{2\left(1 - \frac{3\ell_T^2}{2}\right) + \frac{Dk^2}{4\pi M/3}}\right]^{1/2} \ . \tag{73}$$

It is convenient to also write the growth rate with respect to the variable τ , which is given by the expression

$$\kappa_\tau = \kappa \frac{dt}{d\tau} \quad .$$

Substituting Eqs. (13) and (72) yields the relation

$$\kappa_\tau = \beta \sin \psi_0 \frac{4\pi M}{3H^0} \left[1 - \frac{3\ell_T^2}{2} - \frac{3Dk^2}{4\pi M}\right]^{1/2} \left[\frac{3Dk^2}{4\pi M} - \left(1 - \frac{3\ell_T^2}{2}\right)(1 - 3\alpha_{0T}^2)\right]^{1/2} \quad . \tag{74}$$

From Eq. (57), it also follows that, for large t, α_{k3} and α_{kT} are related through the relation

$$\frac{\alpha_{k3}}{\alpha_{kT}} = - \left[\frac{\left(1 - \dfrac{3\ell_T^2}{2}\right) - \dfrac{Dk^2}{4\pi M/3}}{2\left(1 - \dfrac{3\ell_T^2}{2}\right) + \dfrac{Dk^2}{4\pi M/3}} \right]^{1/2} . \qquad (75)$$

When Eq. (72) is maximized with respect to Dk^2, one obtains the condition

$$(Dk^2)_{max} = \frac{4\pi M}{3} \left(1 - \frac{3\ell_T^2}{2}\right) \left(1 - \frac{3\alpha_{OT}^2}{2}\right) , \qquad (76)$$

for maximum growth for fixed ℓ_T^2. Since ℓ_T^2 and α_{OT}^2 are both less than unity, we immediately verify from the equation our earlier assertion that $c = k/(4\pi M/3D)^{1/2}$ also has a maximum value of unity. Substitution back into Eq. (72) shows that the corresponding value of κ is given by

$$\kappa_{max} = 2\pi M \gamma \alpha_{OT}^2 \left(1 - \frac{3\ell_T^2}{2}\right) . \qquad (77)$$

It is important to note that Eqs. (73) - (75) take the simple forms

$$\phi = 45^{\circ} \qquad (78)$$

$$\alpha_{k3}/\alpha_{kT} = \alpha_{OT}/\sqrt{2} , \qquad (79)$$

when α_{kT} is small and the maximum growth condition given by Eq. (76) pertains.

Referring to Eq. (72), it is clear that pumping only occurs when the expression within the square root is positive. Subject to the condition that $0 < \alpha_{OT}^2 < 1$ and $0 < \ell_T^2 < 1$, and $Dk^2 > 0$, it can be seen that one passes into the pumping region whenever one traverses the curves,

$$\frac{3Dk^2}{4\pi M} = 1 - \frac{3}{2}\ell_T^2 \tag{80}$$

and

$$\frac{3Dk^2}{4\pi M} = (1 - \frac{3}{2}\ell_T^2)(1 - 3\alpha_{OT}^2) \quad . \tag{81}$$

Three possible cases arise, depending on whether $0 < \alpha_{OT}^2 < 1/3$, $1/3 < \alpha_{OT}^2 < 2/3$, or $2/3 < \alpha_{OT}^2 < 1$. These cases have been sketched in Fig. 5.

The spin wave equations of motion were solved numerically for a number of different values of $\bar{k}$. This was done by integrating Eq. (15) numerically without the spin wave back reaction term (i.e., without the $\sum_k$ term) simultaneously with Eq. (16). The results for a particular value of k are given in Figs. 6 - 8, where $(\alpha_{k3}/\alpha_{kT})$, ϕ, and α_{kT} are plotted versus τ with $H_o = 4\pi M/3$. The subscripts 1 and 2 refer to solutions whose spin wave magnetization vector is initially oriented in the x_1 and x_2 directions, respectively. The asymptotic values assumed by these solutions were compared with the results calculated from the equations of this section. The results are compared in Table II and, as can be seen, are in close agreement. Similar comparisons for other spin wave parameters showed like agreement.

- 102 -

TABLE II

COMPARISON OF NUMERICAL INTEGRATION WITH ASYMPTOTIC FORMULA

FOR $\beta = 0.8$, $\psi_o = 50^o$, $\theta_k = 10^o$, $\alpha_{03}/\alpha_{0T} = 2.27$,

$3Dk^2/4\pi M = .5625$, AND $4\pi M/3 = H^o$

Quantity	Numerical Integration		Asymptotic Formula	
	Figure No.	Result	Formula No.	Result
α_{k3}/α_{kT}	6	.397	75	0.397
ϕ	7	$25^o\ 36'$	73	$25^o\ 41'$
κ_T	8	0.104	74	0.102

FIGURE CAPTIONS

Figure 1   Coordinate system.

Figure 2   Variation with normalized time of spin wave energy and
            uniform mode amplitude, precession angle, and energy
            for $\beta = 0.6$ and $\psi_0 = 90^{\circ}$.

Figure 3   Variation with normalized time of spin wave energy and
            uniform mode amplitude, precession angle, and energy
            for $\beta = 0.8$ and $\psi_0 = 45^{\circ}$.

Figure 4   Variation of final precession angle with normalized
            time for 10% degradation of the uniform mode energy.

Figure 5   Regions of spin wave growth.

Figure 6   Variation of α_{k3}/α_{kT} with τ for $\beta = 0.8$, $\psi_0 = 50^{\circ}$,
            $\theta_k = 10^{\circ}$, $3Dk^2/4\pi M = .5625$, and $H_0 = 4\pi M/3$.
            Subscripts 1 and 2 denote initial orientation of spin
            wave vector in x_1 and x_2 directions, respectively.

Figure 7   Variation of ϕ with τ for $\beta = 0.8$, $\psi_0 = 50^{\circ}$,
            $\theta_k = 10^{\circ}$, $3Dk^2/4\pi M = 0.5625$, and $H_0 = 4\pi M/3$. Sub-
            scripts 1 and 2 denote initial orientation of spin wave
            vector in x_1 and x_2 directions, respectively.

Figure 8   Variation of α_{kT} with τ for $\beta = 0.8$, $\psi_0 = 50^{\circ}$,
            $\theta_k = 10^{\circ}$, $3Dk^2/4\pi M = 0.5625$, and $4\pi M/3 = H_0$. Subscripts
            1 and 2 denote initial orientation of the spin wave vector
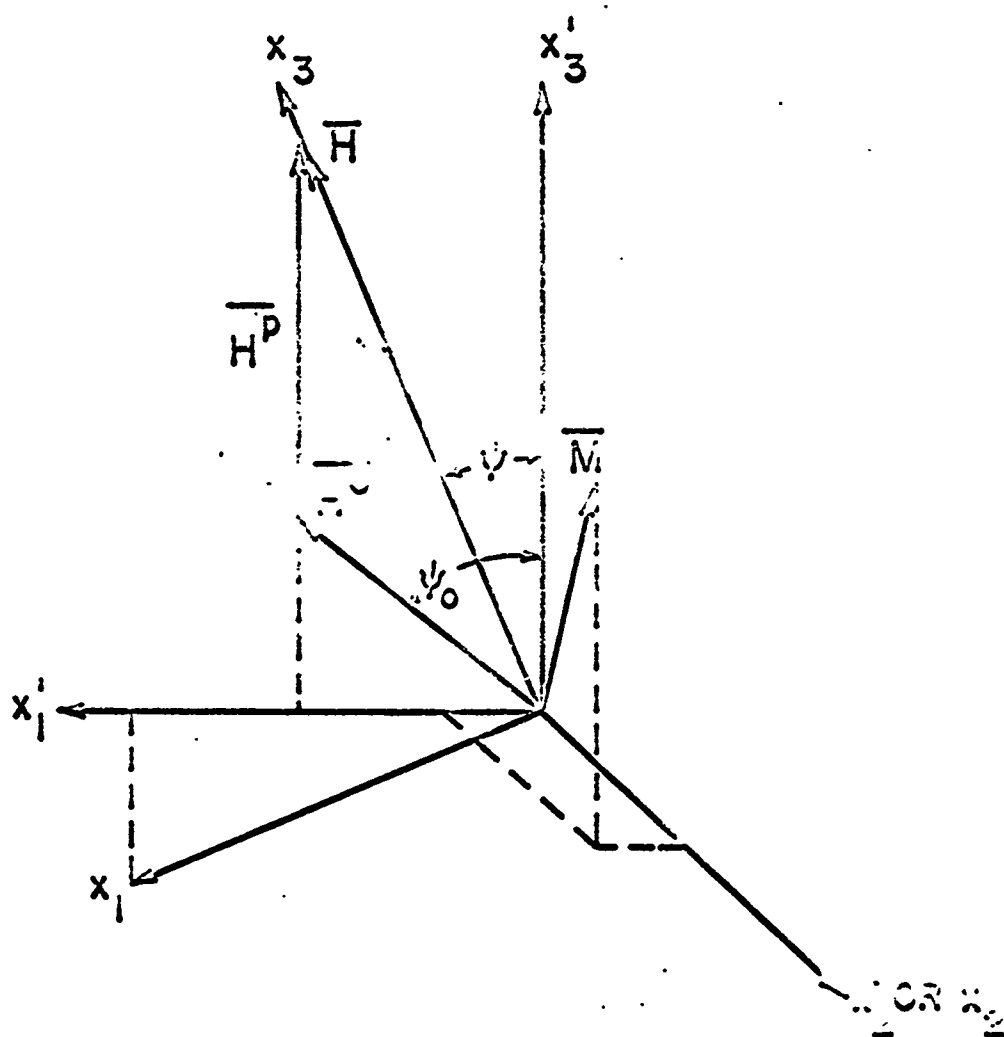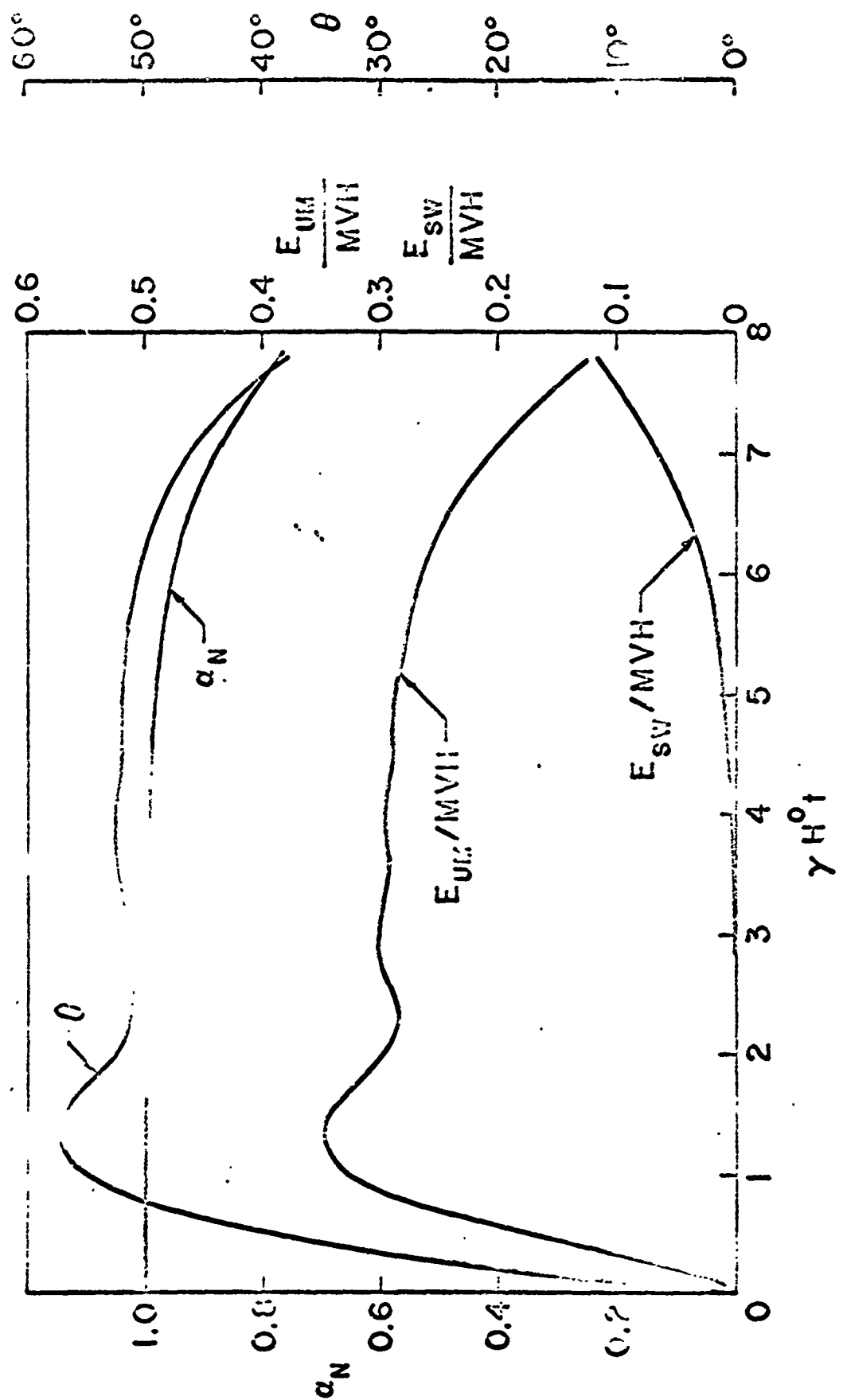   in x_1 and x_2 directions, respectively.
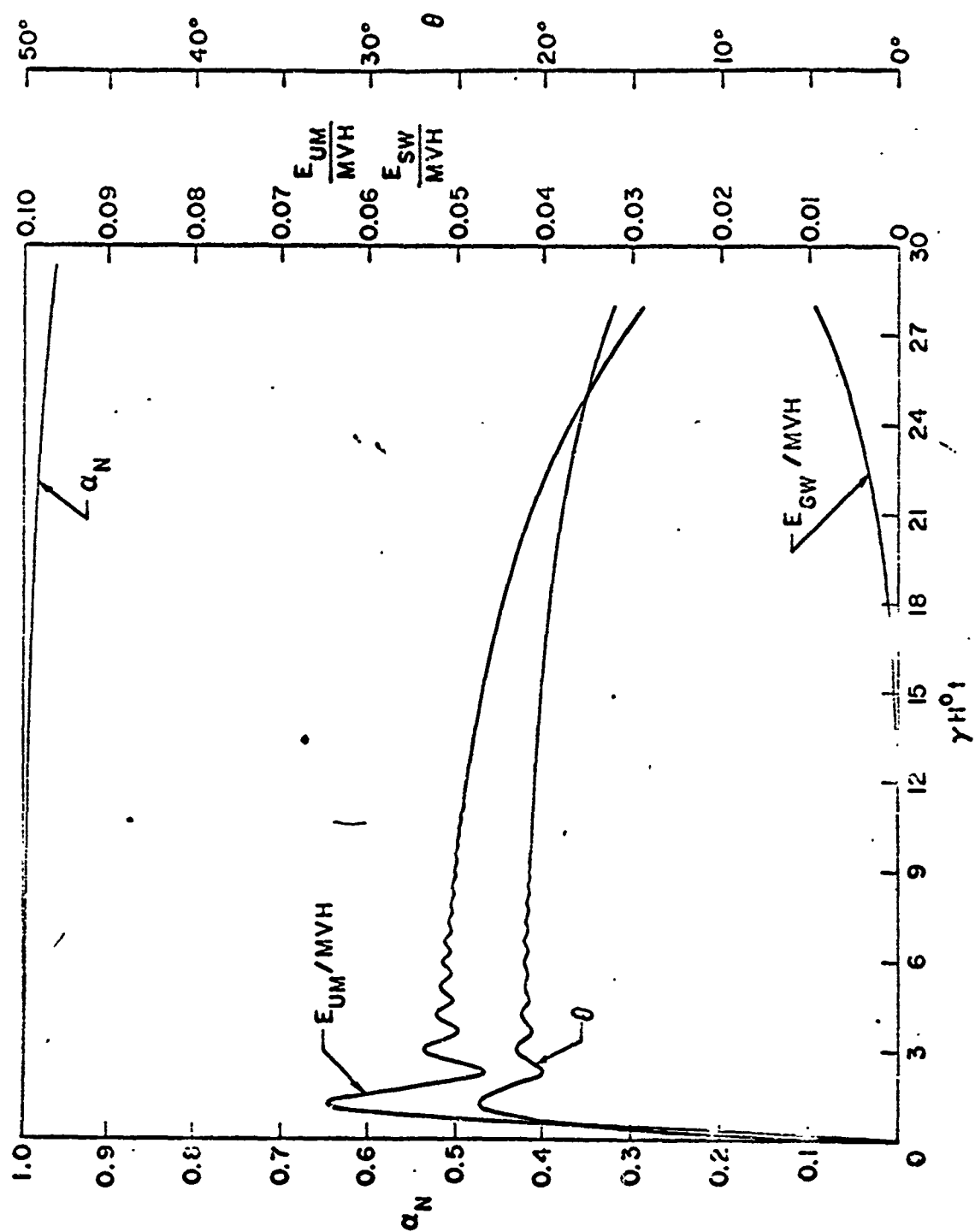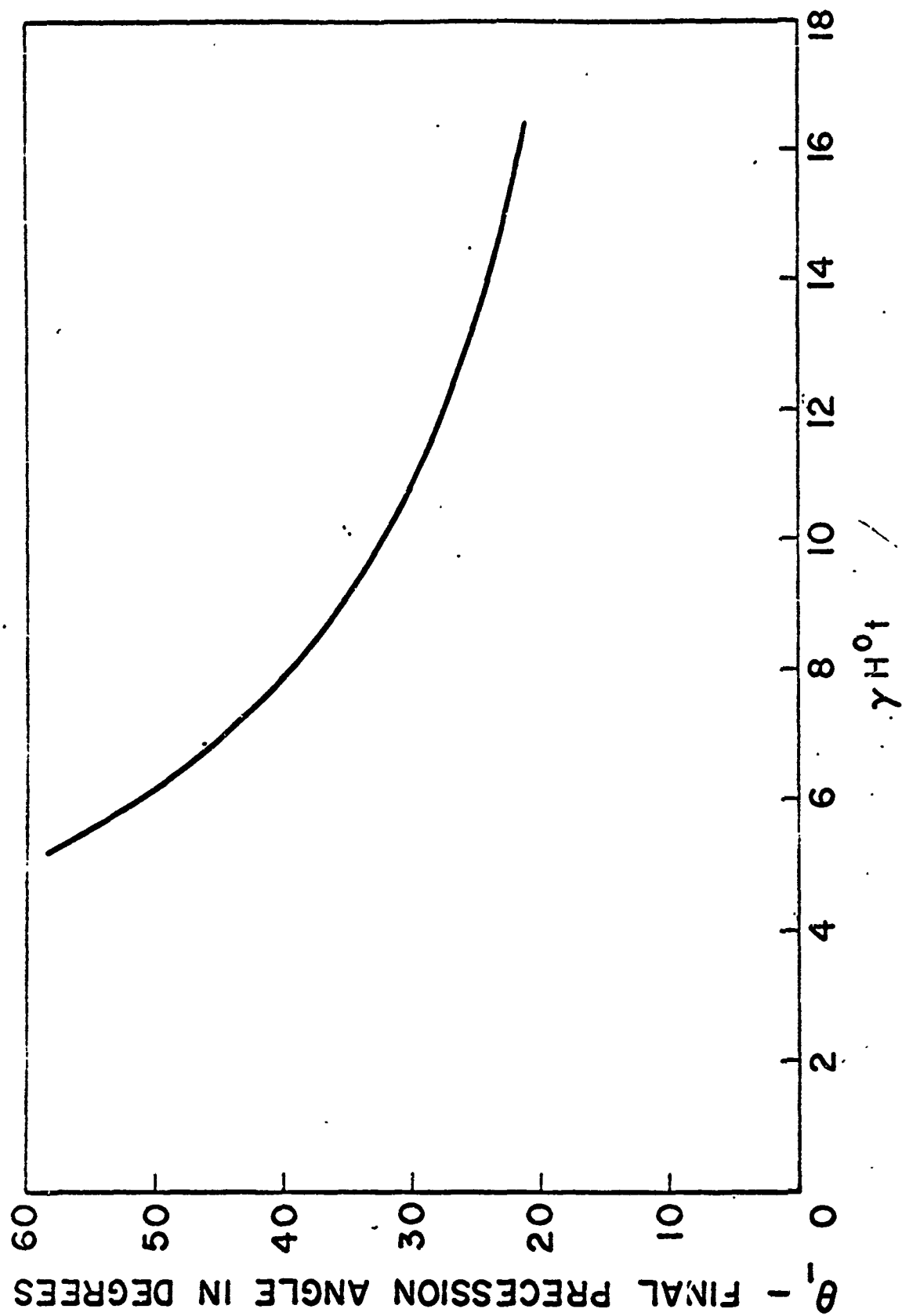
FIGURE 1

- 105 -

FIGURE 2

FIGURE 3

FIGURE 4

FIGURE 5

- 109 -

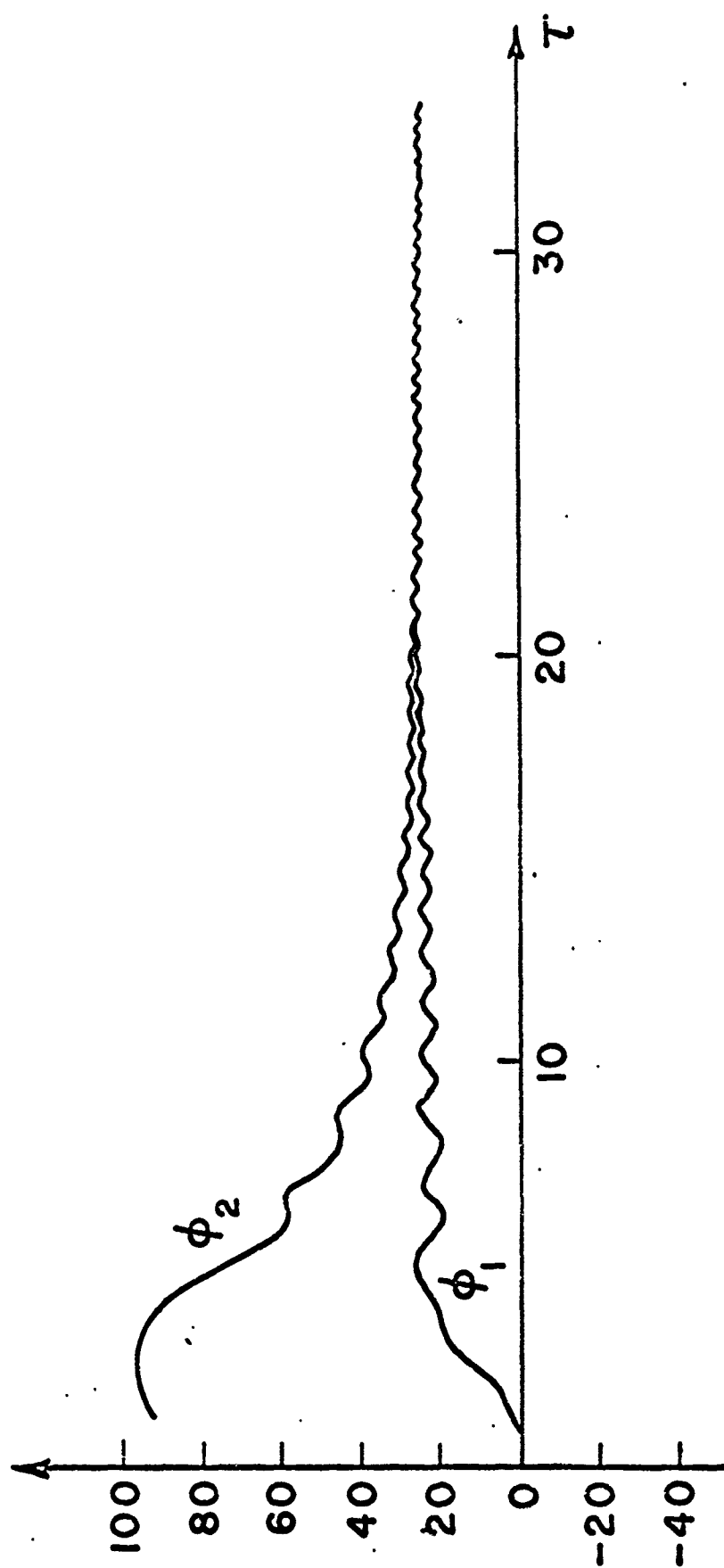FIGURE 6

- 110 -
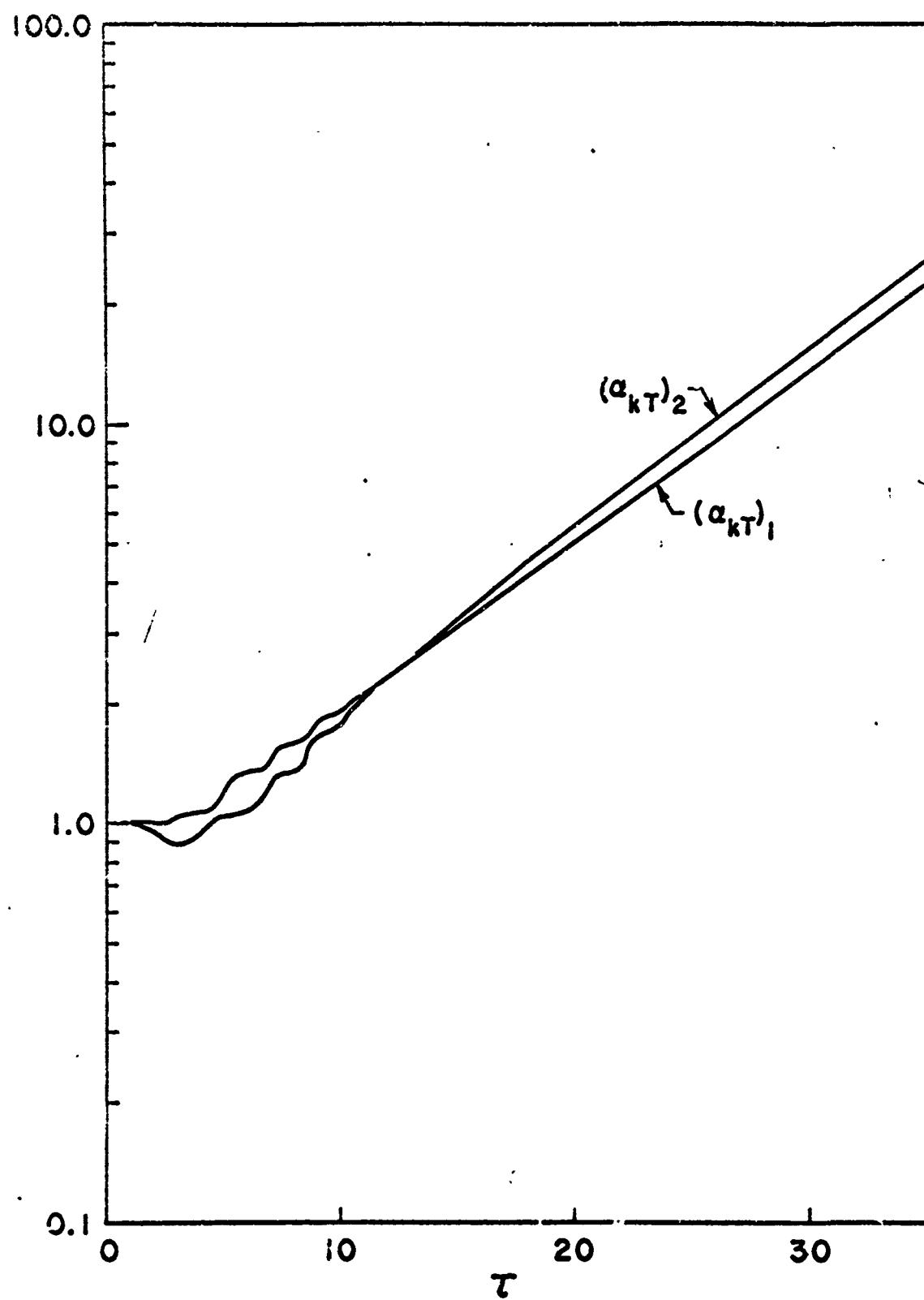
FIGURE 7

- 111 -

FIGURE 8

- 112 -
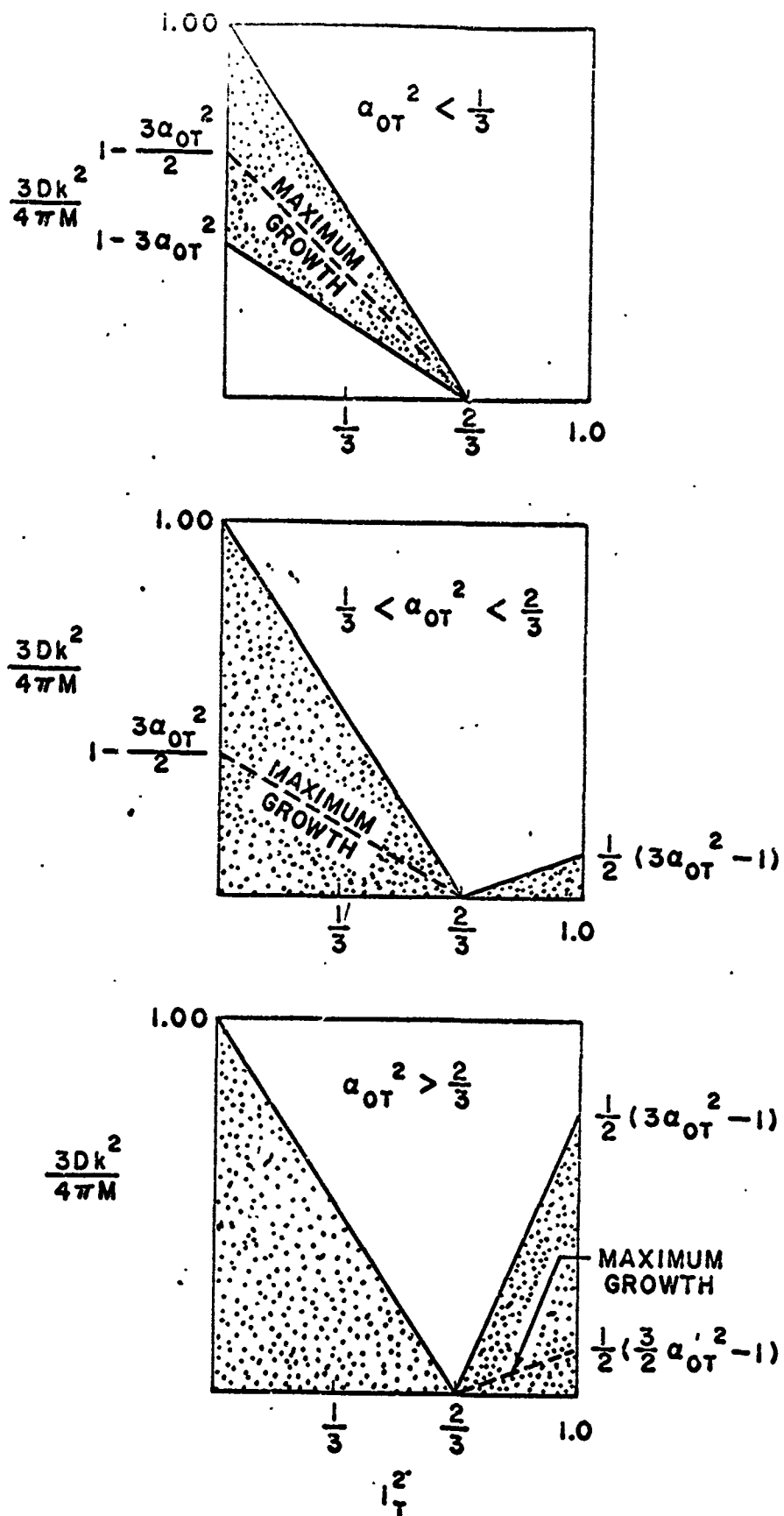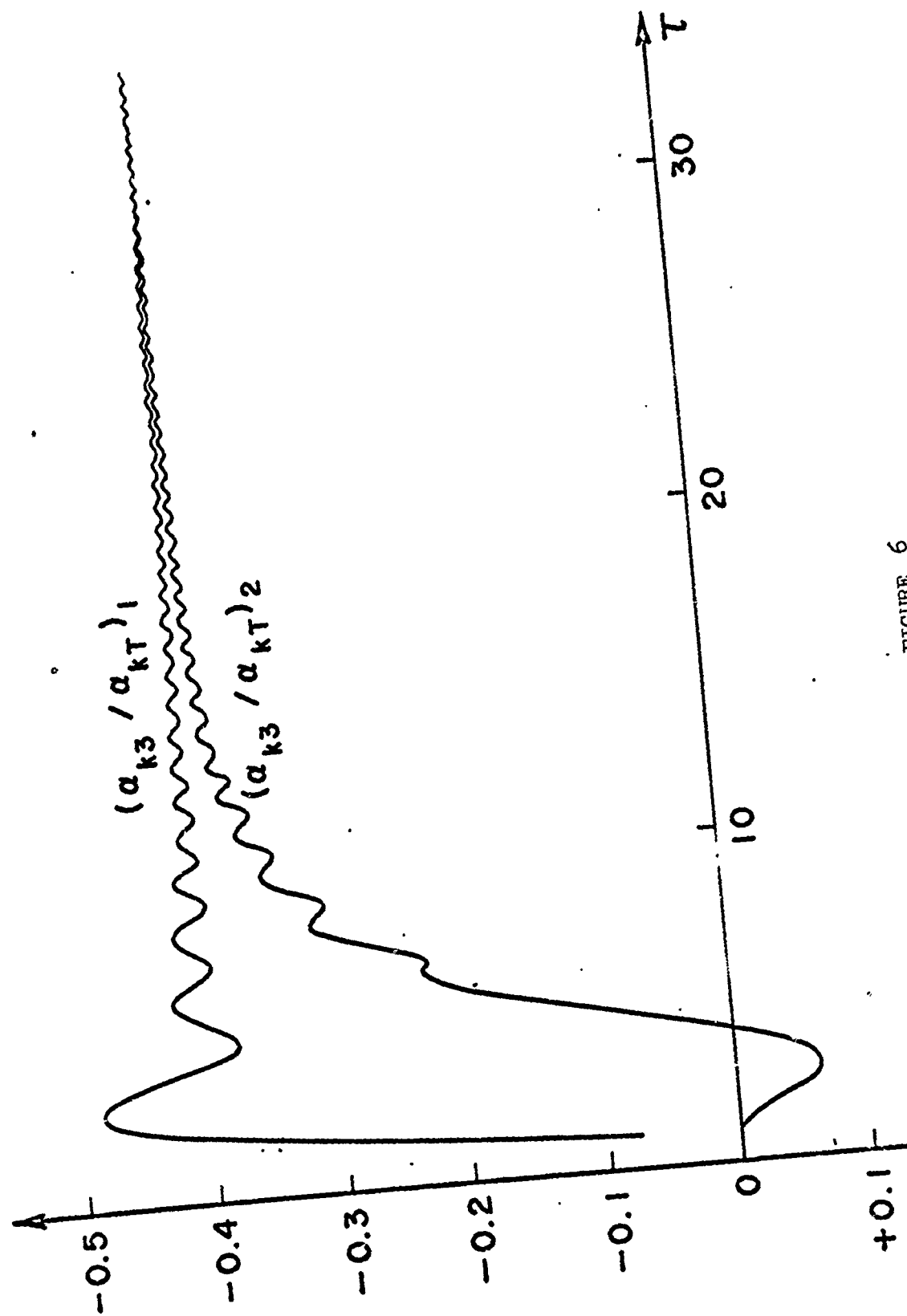
REFERENCES

1. H. Prunet, Compt. Rend. $\underline{252}$, 2860 (1961).

2. H. J. Shaw and B. J. Elliott, "Pulsed Magnetic Field Millimeter
    Wave Generator," Microwave Laboratory Report No. 856, Stanford
    University (September 1961); also, "Generation of Microwave Radi-
    ation with Ferrimagnetic Samples Subjected to Pulsed Magnetic
    Fields," Magnetic and Electric Resonance and Relaxation, Proc.
    of the XIth Colloque Ampère, Eindhoven, 2 - 7 July 1962 (North
    Holland Publishing Co., Amsterdam, Holland, 1963), p. 770.

3. F. R. Morgenthaler, Trans. IRE, PGMTT $\underline{MTT-7}$, 6-11 (January 1959).

4. T. Schaug-Petterson, "Growing Spin Waves in Ferrites in Unstable
    Equilibrium," J. Appl. Phys. Suppl. $\underline{31}$, 382S (May 1960).

5. E. Schlömann, unpublished memorandum, Microwave Laboratory,
    Stanford University, 1962.

6. K. J. Harker, "Final Precession Angles for Pulsed Ferrite Samples,"
    Microwave Laboratory Report No. 1149 (Revised), Stanford University
    (May 1965).

7. B. J. Elliott, T. Schaug-Petterson, and H. J. Shaw, J. Appl. Phys.
    Suppl. $\underline{31}$, 400 (1960).

8. M. R. Stiglitz and F. R. Morganthaler, J. Appl. Phys. $\underline{31}$, 37 (1960).

9. A. P. Aleksandrov, V. I. Kronin, and E. G. Yaschen, JETP $\underline{38}$,
    1334 (1960).

10. H. Suhl, Proc. IRE $\underline{44}$, 1270 (1956).

11. E. Schlömann, "Ferromagnetic Resonance at High Power Levels,"
    Raytheon Report No. R-28 (October 1, 1959), Research Div.,
    Raytheon Company, Waltham 54, Mass.

12. E. Schlömann, J. Appl. Phy:. $\underline{33}$, 2822 (1962).

13. K. J. Harker and H. J. Shaw, J. Appl. Phys. $\underline{35}$, 902 (1964).

14. 1963 Microwave Engineer's Handbook and Buyer's Guide, T. S. Sand,
    Ed. (Horizon House-Microwave Inc., Brookline, Mass.) p. T-169.

15. E. Schlömann, Phys. Rev. $\underline{121}$, 1317 (1961).

COUPLED CIRCUIT ANALYSIS

The purpose of these calculations is to study a pair of coupled resonant circuits where the frequency of one circuit is swept linearly with time through the resonance of the other. The point of interest is the amount of energy transferred from the swept to the unswept circuit.

Figure 1 shows the circuit used. Here, L_1 and C_1 are time-dependent quantities. Thus, care must be taken to calculate the proper time derivatives of terms involving these quantities. When L and C are time dependent, the voltages across the elements are

$$V_L = \frac{d}{dt} \quad Li \tag{1}$$

$$V_C = \frac{1}{C} \int dt \quad . \tag{2}$$

Keeping this in mind, and applying Kirchoff's laws, one can derive the following equations;

$$L_2 \frac{di_2}{dt} + \frac{1}{C_2} \int i_2 dt + i_2 R_2 + \frac{d}{dt} (L_1(t)i_1) = 0 \tag{3}$$

$$\frac{d}{dt} (L_1(t)i_1) = \frac{1}{C_1(t)} \int i_4 dt \tag{4}$$

$$\frac{d}{dt} (L_1(t) i_1) = R_1 i_3 \tag{5}$$

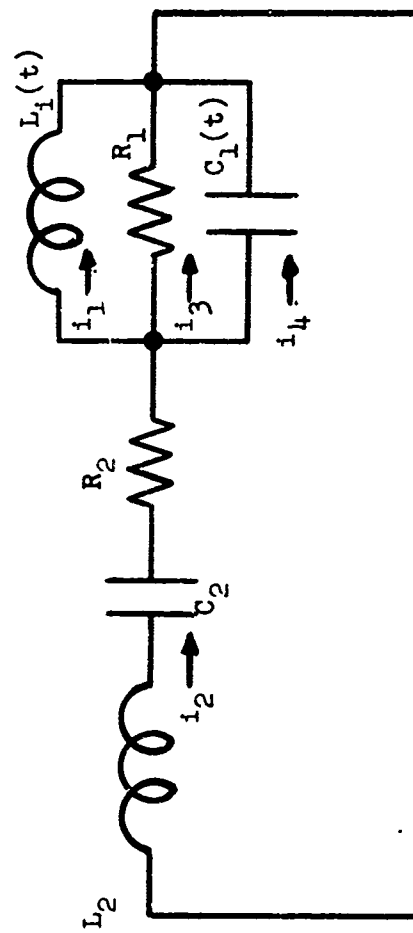$$i_2 = i_1 + i_3 + i_4 \quad . \tag{6}$$

FIG. 2.--Schematic of coupled circuits.

The change of variables

$$Z = \frac{L_1(t)}{L_{10}} i_1 \quad , \quad i_1 = \frac{L_{10}}{L_1(t)} Z \tag{7}$$

simplifies the equations considerably. We have

$$L_2 \frac{di_2}{dt} + \frac{1}{C_2} \int i_2 dt + R_2 i_2 + L_{10} \frac{dZ}{dt} = 0 \tag{8}$$

$$L_{10} \frac{dZ}{dt} = \frac{1}{C_1(t)} \int i_4 dt \tag{9}$$

$$L_{10} \frac{dZ}{dt} = R_1 i_3 \quad . \tag{10}$$

We next define the following normalizing parameters:

$$\frac{1}{\sqrt{L_1 C_1}} = \omega_1 \quad , \quad \frac{1}{\sqrt{L_2 C_2}} = \omega_2 \quad , \quad \omega_2 t = \tau \quad . \tag{11}$$

We then find:

$$\frac{di_2}{d\tau} + \int i_2 d\tau + Q_2^{-1} i_2 + \frac{L_{10}}{L_2} \frac{dZ}{d\tau} = 0 \quad , \quad Q_2^{-1} = \frac{R_2}{\omega_2 L_2} \quad , \tag{12}$$

$$\frac{C_1}{C_{10}} \frac{dZ}{d\tau} = \left(\frac{\omega_{10}}{\omega_2}\right)^2 \int i_4 d\tau \quad , \tag{13}$$

$$\frac{dZ}{d\tau} = \frac{L_1}{L_{10}} \frac{\omega_1}{\omega_2} Q_1 i_3 \quad , \quad Q_1 = \frac{R_1}{L_1 \omega_1} \quad . \tag{14}$$

- 117 -

Changing to the symbolization $\mu' = \dfrac{d\mu}{d\tau}$ and taking derivatives:

$$i_2'' + Q_2^{-1}\, i_2' + i_2 + \frac{L_{10}}{L_2}\, Z'' = 0 \tag{15}$$

$$\frac{C_1}{C_{10}}\, Z'' + \frac{C_1'}{C_{10}}\, Z' = \left(\frac{\omega_{10}}{\omega_2}\right)^2 \cdot i_4 \tag{16}$$

$$Z'' + \frac{C_1'}{C_1}\, Z' - \frac{C_{10}}{C_1} \left(\frac{\omega_{10}}{\omega_2}\right)^2 \cdot i_4 = 0 \quad . \tag{17}$$

Since

$$i_4 = i_2 - i_1 - i_3 \quad , \tag{18}$$

$$Z'' + \frac{C_1'}{C_1}\, Z' - \frac{C_{10}}{C_1} \left(\frac{\omega_{10}}{\omega_2}\right)^2 (i_2 - i_1 - i_3) = 0 \quad . \tag{19}$$

Since

$$i_3 = \frac{L_{10}}{L_1}\frac{\omega_2}{\omega_1}\, Q_2^{-1}\, Z' \quad , \tag{20}$$

we have

$$Z'' + \frac{C_1'}{C_1}\, Z' + \frac{\omega_1}{\omega_2}\, Q_1^{-1}\, Z' + \left(\frac{\omega_1}{\omega_2}\right)^2 Z - \frac{C_{10}}{C_1} \left(\frac{\omega_{10}}{\omega_2}\right)^2 i_2 = 0 \tag{21}$$

$$i_2'' + Q_2^{-1}\, i_2' + i_2 + \frac{L_{10}}{L_2}\, Z'' = 0 \quad . \tag{22}$$

- 118 -

These are the equations describing the system, with arbitrary time-dependent parameters L_1 and C_1.

We now use the following restrictions:

$$\frac{\omega_1}{\omega_2} = \sqrt{\frac{L_2 C_2}{L_1 C_1}} = a + b\tau \tag{23}$$

$$\sqrt{\frac{L_1 C_2}{L_2 C_1}} = K = \text{constant} \ . \tag{24}$$

These lead to:

$$\frac{C_2}{C_1} = K(a + b\tau) \tag{25}$$

$$\frac{C_1}{C_{10}} = \frac{a + b\tau}{a} \tag{26}$$

$$\frac{C_1'}{C_1} = -\frac{b}{a + b\tau} \tag{27}$$

$$\frac{L_1}{L_2} = \frac{K}{a + b\tau} \tag{28}$$

$$\frac{L_{10}}{L_2} = \frac{K}{a} \ . \tag{29}$$

- 119 -

Equations (21) and (22) then become

$$Z'' + \left((a + b\tau)\, Q_1^{-1} - \frac{b}{a + b\tau} \right) Z' + (a + b\tau)^2\, Z - a(a + b\tau)i_2 = 0$$

(30)

$$i_2'' + Q_2^{-1}\, i_2' + i_2 + \frac{K}{z}\, Z'' = 0$$

(31)

where

$$i_1 = \frac{L_{10}}{L_1(t)}\, Z = \left(\frac{a + b\tau}{a} \right) Z \quad .$$

(32)

The energies in the two resonators are found to be

$$\frac{U_1}{U_{10}} = \frac{1}{a} \left(\frac{1}{a + b\tau}^{2} + (a + b\tau)\, Z^2 \right)$$

(33)

$$\frac{U_2}{U_{10}} = \frac{a}{K} \left(i_2^2 + (i_2' + Q_2^{-1}\, i_2 + \frac{K}{a}\, Z')^2 \right) \quad .$$

(34)

The equations were programmed as four first-order equations, where:

$$X_1 = Z \ , \ X_2 = Z' \ , \ X_3 = i_2 \ , \ X_4 = i_2'$$

(35)

$$X_1' = X_2$$

$$X_2' = -[(a + b\tau)\, Q_1^{-1} - \frac{b}{a + b\tau}]\, X_2 - (a + b\tau)^2\, X_1 + a(a + b\tau)\, X_3$$

(36)

$$X_3' = X_4$$

- 120 -

and

$$X_4' \;=\; -\, Q_2^{-1}\, X_4 \,-\, X_3 \,-\, \frac{K}{a}\, X_2' \qquad . \qquad\qquad (37)$$

Computer runs were made of several of the quantities involved in Fig. 1. These quantities were plotted by the computer as a function of the normalized time parameter τ . The quantities i_1 , i_2 , instantaneous power delivered to the resistance R_2 , and cumulative energy delivered to the resistance R_2 , we calculated, in addition to the total energies in the two circuits, as a function of time. Thirty-one cases were run using various combinations of the parameters A , B , τ , Q_1 and Q_2 .

In Section II.A of the main body of this report, the energy distribution in the two circuits is shown for one special case which is of interest. In Figs. 2 through 5 below we show the plots of the remaining quantities for this same special case. Again, the parameter values for this case are $A = 0.1$, $B = 1/20\pi$, $\tau = 0.004$, $Q_1 = 1{,}000$, and $Q_2 = 50$

FIG. 2--Current i_1 as a function of normalized time τ
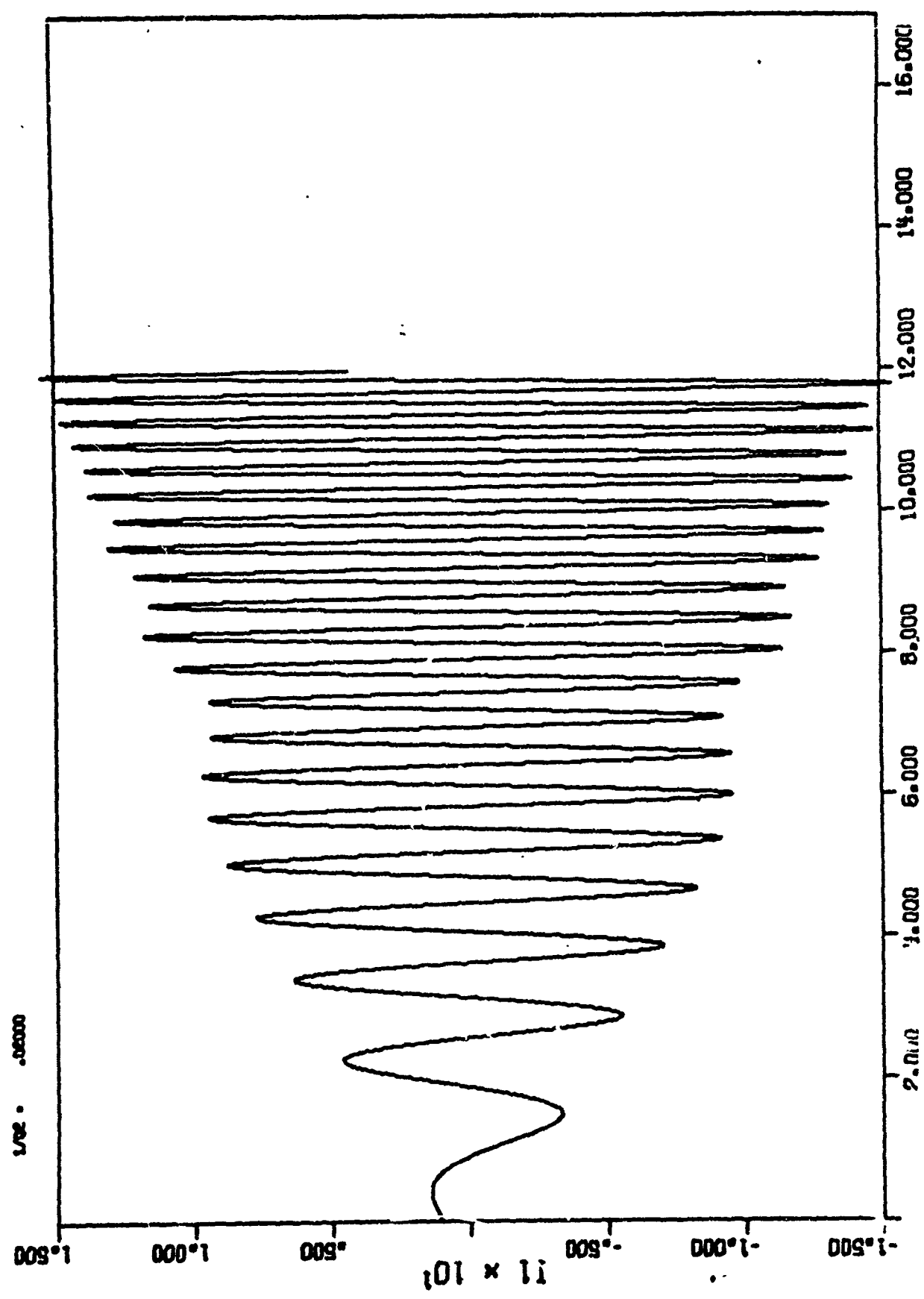
FIG. 3--Current i_2 as a function of normalized time τ.
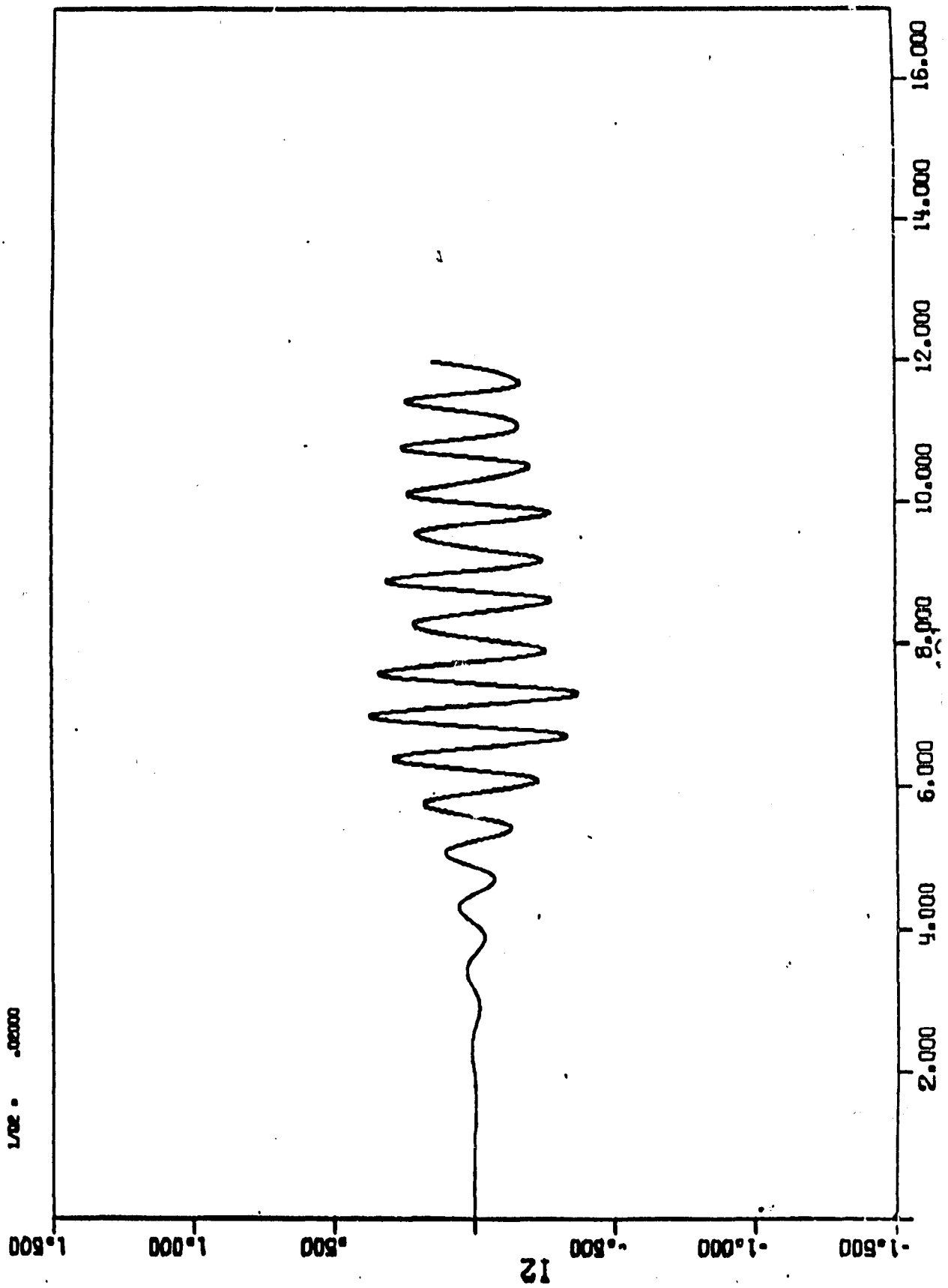
FIG. 4.—Instantaneous power delivered to resistance R_2 as a function of normalized time τ.
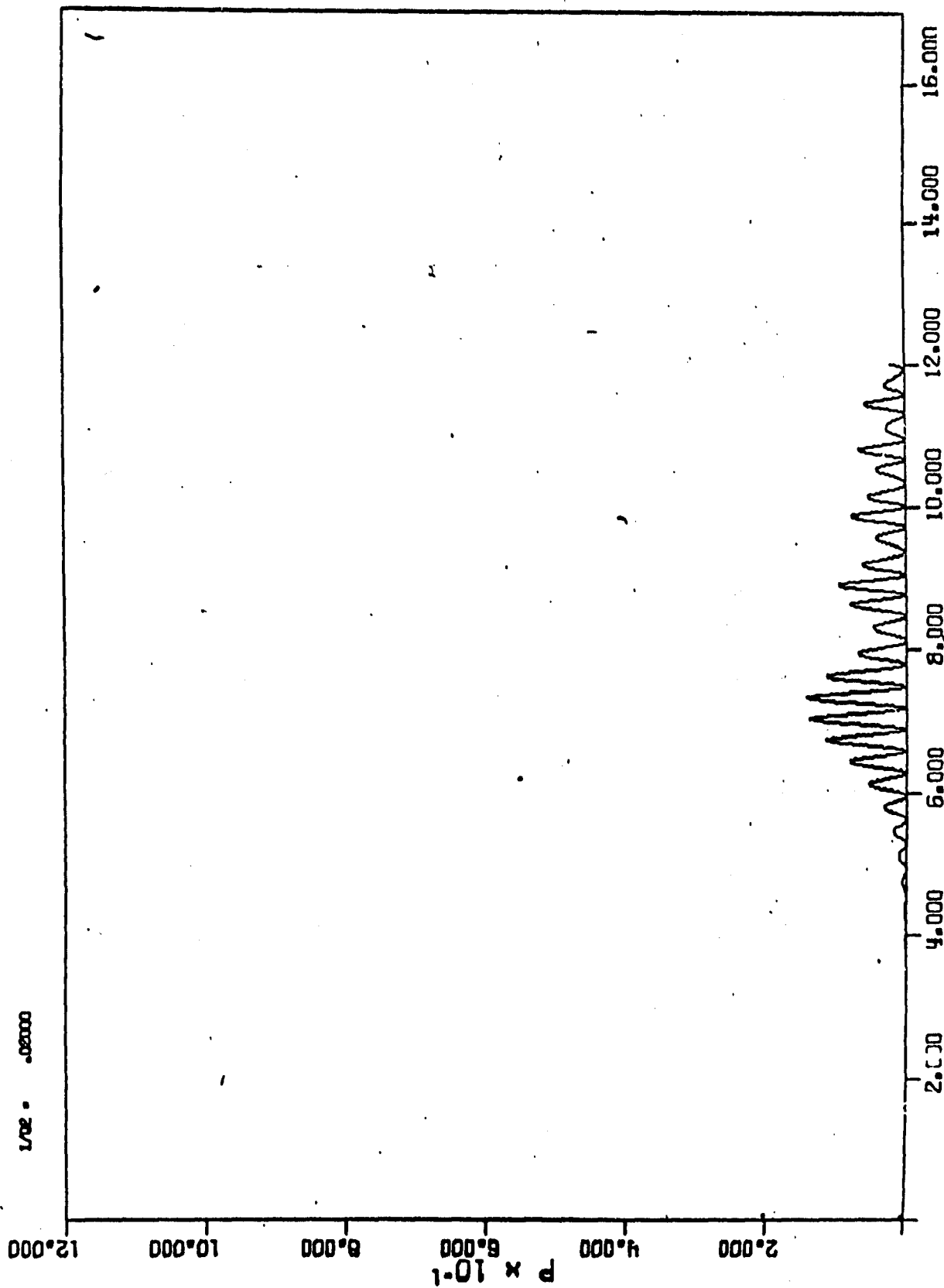
FIG. 5--Energy delivered to resistance R_2 as a function of normalized time τ
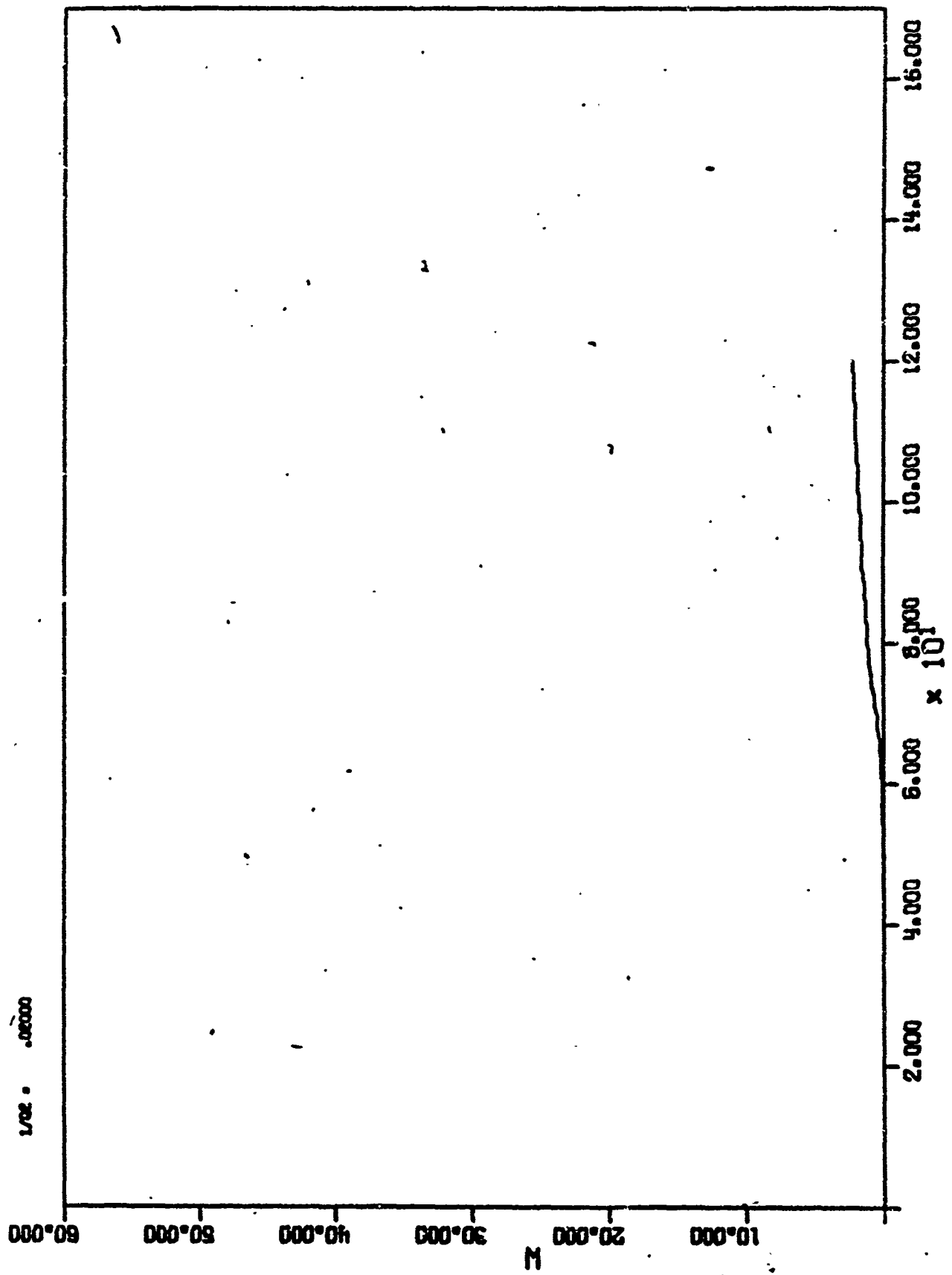
DOCUMENT CONTROL DATA - R&D

(Security classification of title, body of abstract and indexing annotation must be entered when the overall report is classified)

1. ORIGINATING ACTIVITY (Corporate author)	2a. REPORT SECURITY CLASSIFICATION
Stanford University	UNCLASSIFIED
Stanford, California	2b. GROUP N/A

3. REPORT TITLE

PULSED FERRITE X-BAND GENERATOR

4. DESCRIPTIVE NOTES (Type of report and inclusive dates)
Final Report

5. AUTHOR(S) (Last name, first name, initial)

Shaw H. J.

6. REPORT DATE	7a. TOTAL NO. OF PAGES	7b. NO. OF REFS
March 1967	125	

8a. CONTRACT OR GRANT NO.	9a. ORIGINATOR'S REPORT NUMBER(S)
DA 28-043 AMC-00397(E)	
b. PROJECT NO. 1G0-22001-A-055-05	M. L. Report No. 1467
c.	9b. OTHER REPORT NO(S) (Any other numbers that may be assigned this report)
d.	

10. AVAILABILITY/LIMITATION NOTICES

Distribution of this document is unlimited

11. SUPPLEMENTARY NOTES	12. SPONSORING MILITARY ACTIVITY
	U. S. Army Electronics Command
	Fort Monmouth, New Jersey AMSEL-KL-TG

13. ABSTRACT

A magnetically saturated ferrite subjected to a pulsed magnetic field forms a generator of coherent microwave energy. It is shown that relatively high peak rf power in short pulses can be generated in this way. A pulsed magnetic field having amplitude ~ 4 Kg and rise time ~ 1 ns is developed by a strip-line pulser with spark-gap switches. This pulsed field causes nonadiabatic excitation of a coherent oscillation in a YIG sphere. The pulsed field also produces adiabatic pumping of the frequency and energy of this oscillation, so that the output frequency is not related to the pulsed-field rise time. The entire process is completed inside the build-up time of second-order spin waves, allowing precession angles in the YIG to exceed the usual steady-state spin-wave threshold by an order of magnitude. A monolithic circuit element contains a pulsed-field loop and an x-band resonator, which are mutually uncoupled but both tightly coupled to the YIG. The resonator extracts x-band energy from the YIG by radiation damping and transfers it to an output waveguide. The resonator is tunable and determines the output frequency. Coherent, nearly monochromatic rf output pulses having energy of several hundred watt-ns, and pulse widths in the range of 1 - 3 ns, have been observed using YIG diameters in the vicinity of 50 mils. These results are in good agreement with theoretical predictions.

DD FORM 1473 JAN 64

14. KEY WORDS	LINK A		LINK B		LINK C	
	ROLE	WT	ROLE	WT	ROLE	WT
Millimeter Wave Frequency Generation Ferrites Nanosecond Pulses						

INSTRUCTIONS

1. **ORIGINATING ACTIVITY:** Enter the name and address of the contractor, subcontractor, grantee, Department of Defense activity or other organization (*corporate author*) issuing the report.

2a. **REPORT SECURITY CLASSIFICATION:** Enter the overall security classification of the report. Indicate whether "Restricted Data" is included. Marking is to be in accordance with appropriate security regulations.

2b. **GROUP:** Automatic downgrading is specified in DoD Directive 5200.10 and Armed Forces Industrial Manual. Enter the group number. Also, when applicable, show that optional markings have been used for Group 3 and Group 4 as authorized.

3. **REPORT TITLE:** Enter the complete report title in all capital letters. Titles in all cases should be unclassified. If a meaningful title cannot be selected without classification, show title classification in all capitals in parenthesis immediately following the title.

4. **DESCRIPTIVE NOTES:** If appropriate, enter the type of report, e.g., interim, progress, summary, annual, or final. Give the inclusive dates when a specific reporting period is covered.

5. **AUTHOR(S):** Enter the name(s) of author(s) as shown on or in the report. Enter last name, first name, middle initial. If military, show rank and branch of service. The name of the principal author is an absolute minimum requirement.

6. **REPORT DATE:** Enter the date of the report as day, month, year; or month, year. If more than one date appears on the report, use date of publication.

7a. **TOTAL NUMBER OF PAGES:** The total page count should follow normal pagination procedures, i.e., enter the number of pages containing information.

7b. **NUMBER OF REFERENCES:** Enter the total number of references cited in the report.

8a. **CONTRACT OR GRANT NUMBER:** If appropriate, enter the applicable number of the contract or grant under which the report was written.

8b, 8c, & 8d. **PROJECT NUMBER:** Enter the appropriate military department identification, such as project number, subproject number, system numbers, task number, etc.

9a. **ORIGINATOR'S REPORT NUMBER(S):** Enter the official report number by which the document will be identified and controlled by the originating activity. This number must be unique to this report.

9b. **OTHER REPORT NUMBER(S):** If the report has been assigned any other report numbers (*either by the originator or by the sponsor*), also enter this number(s).

10. **AVAILABILITY/LIMITATION NOTICES:** Enter any limitations on further dissemination of the report, other than those

imposed by security classification, using standard statements such as:

(1) "Qualified requesters may obtain copies of this report from DDC."

(2) "Foreign announcement and dissemination of this report by DDC is not authorized."

(3) "U. S. Government agencies may obtain copies of this report directly from DDC. Other qualified DDC users shall request through

_____."

(4) "U. S. military agencies may obtain copies of this report directly from DDC. Other qualified users shall request through

_____."

(5) "All distribution of this report is controlled. Qualified DDC users shall request through

_____."

If the report has been furnished to the Office of Technical Services, Department of Commerce, for sale to the public, indicate this fact and enter the price, if known.

11. **SUPPLEMENTARY NOTES:** Use for additional explanatory notes.

12. **SPONSORING MILITARY ACTIVITY:** Enter the name of the departmental project office or laboratory sponsoring (*paying for*) the research and development. Include address.

13. **ABSTRACT:** Enter an abstract giving a brief and factual summary of the document indicative of the report, even though it may also appear elsewhere in the body of the technical report. If additional space is required, a continuation sheet shall be attached.

It is highly desirable that the abstract of classified reports be unclassified. Each paragraph of the abstract shall end with an indication of the military security classification of the information in the paragraph, represented as (*TS*), (*S*), (*C*), or (*U*).

There is no limitation on the length of the abstract. However, the suggested length is from 150 to 225 words.

14. **KEY WORDS:** Key words are technically meaningful terms or short phrases that characterize a report and may be used as index entries for cataloging the report. Key words must be selected so that no security classification is required. Identifiers, such as equipment model designation, trade name, military project code name, geographic location, may be used as key words but will be followed by an indication of technical context. The assignment of links, rules, and weights is optional.